Hadron Distribution Amplitudes from Lattice QCD Simulations

DISSERTATION
ZUR ERLANGUNG DES DOKTORGRADES
DER NATURWISSENSCHAFTEN (DR. RER. NAT.)
DER FAKULTÄT FÜR PHYSIK

DER UNIVERSITÄT REGENSBURG

vorgelegt von

Fabian Hutzler

aus

Regensburg

im Jahr 2018

Promotionsgesuch eingereicht am: 15.01.2018
Die Arbeit wurde angeleitet von: Prof. Dr. Andreas Schäfer

Prüfungsausschuss:

Vorsitzender:	Prof. Dr. Josef Zweck
1. Gutachter:	Prof. Dr. Andreas Schäfer
2. Gutachter:	Prof. Dr. Vladimir Braun
weiterer Prüfer:	Prof. Dr. Jaroslav Fabian

Abstract

In this thesis we examine hadron distribution amplitudes, which are universal, process-independent functions that govern the physics of hard exclusive processes and contribute to both, measurements of fundamental parameters of the Standard Model and probes of new physics. For this purpose, we perform lattice QCD simulations for mesons and baryons in order to calculate Mellin moments of the distribution amplitudes numerically.

Contents

1 Introduction

In the mind of contemporary physicists, the development of quantum chromodynamics (QCD), the theory of the strong interaction, marked a radical change of perception of our physical world: During the 1950s, it was common belief that all hadrons like the proton or pion are equally elementary particles as reflected by the concept of *nuclear democracy* or *hadronic egalitarianism* [1–4]. However, this view had changed completely by the end of the 70s and it has since been generally accepted that hadrons are composed of fractionally charged fermionic quarks that are bound together by electrically neutral gluons, the gauge bosons of the theory which act as mediators of the strong force between the quarks.

In order to satisfy the spin-statistics theorem [5] for ground state hadron multiplets, refs. [6–8] proposed the existence of an additional quantum number that is nowadays known as color. Consequently, each quark was assigned one of the three color charges *red*, *blue* or *green*. In fact, QCD is a Yang-Mills theory [9] with the underlying non-abelian gauge group $\mathrm{SU}(3)_c$. Therefore, each quark is represented by a triplet of fields, while the gluons form a color octet. Quarks and gluons exhibit color confinement, which means that below the Hagedorn temperature they cannot be observed as free particles and are therefore bound in color-singlet hadronic states. The reason for this is that the QCD one-loop beta function is negative for $N_f \leq 16$, which is a consequence of the non-abelian nature of the theory that allows self-interacting gauge bosons. As a result, the quark interaction becomes weaker for higher momentum transfers Q^2, such that quarks behave asymptotically free at large energies. In contrast, the strong coupling constant grows for smaller Q^2, which leads to the confinement of quarks within hadrons. Hadrons themselves can be further classified into two subgroups, namely baryons and mesons. The former are composite fermions which contain three valence quarks while the latter are bosons with a quark-antiquark pair valence structure. The Standard Model involves quarks of six different flavors: *up*-, *down*-, *charm*-, *strange*-, *top*- and *bottom*-quarks. Their masses range over several orders of magnitude, from the light up-quark with $m_u = 2.2$ MeV to the heavy top quark which has almost the mass of a gold atom with $m_t = 173.1$ GeV [10].

Due to the intrinsically non-perturbative nature of confinement, hadron structure in terms of quarks and gluons is highly non-trivial. It can be described with universal process-independent QCD functions like parton distribution functions (PDFs) and hadron distribution amplitudes (DAs), which are relevant for both, measurements of fundamental parameters of the Standard Model and probes of new physics. PDFs are needed to describe

deep inelastic scattering (DIS) experiments [11–16], where the inner structure of hadrons is resolved by probing them inclusively with leptons. In order to understand the inelastic scattering process, it is helpful to consider the naive parton model [17], where the hadronic structure functions that parametrize the differential cross section become independent of the momentum transfer Q^2 in the asymptotic limit [18]. This so-called Bjorken scaling behavior can be understood in the infinite-momentum frame, where the hadron is considered as a ray of collinear quasi-free partons. Consequently, at a large enough momentum transfer Q^2, the incoming lepton directly scatters with a quasi-free quark that carries the longitudinal momentum fraction x of the hadron, such that the resulting process can be described as lepton-quark scattering instead of lepton-hadron scattering. Early measurements showed that quarks are merely responsible for half of the nucleon's momentum [19], so that the remaining momentum has to be carried by electromagnetically non-interacting partons that were eventually identified as gluons. Strictly speaking, the naive parton model is an approximation of QCD which is only valid for vanishing coupling strength. In reality, Bjorken scaling is somewhat violated. As a consequence, PDFs exhibit a scale dependence which is governed by the famous DGLAP equations [20–22]. Thus, at a certain energy scale Q^2, a PDF specifies the probability density to find a parton of a certain kind that carries the longitudinal momentum fraction x of the hadron.

In this work, however, we will focus on hadron distribution amplitudes, which are fundamental non-perturbative functions that can be interpreted as light-cone wave functions integrated over transverse quark momenta [23, 24]. Because of this, they are sensitive to those Fock states of the hadronic wave function which govern exclusive processes with large momentum transfer Q^2. In the limit $Q^2 \to \infty$, distribution amplitudes are given by their so-called asymptotic expressions [23–25], which, however, deviate significantly from their form at experimentally accessible momentum transfers. Therefore, in view of constantly increasing luminosities of modern research facilities like the 12 GeV upgrade at JLAB [26] or the future EIC [27], a precise determination of hadron distribution amplitudes is essential in order to provide rigorous theoretical descriptions of hard exclusive processes. Compared to PDFs, the connection between DAs and experimentally accessible observables is more challenging. Especially the relations between hadronic form factors and hadron distribution amplitudes are of particular importance. For example, it is known that for very high momentum transfers Q^2, hard exclusive processes like elastic electron-nucleon scattering are dominated by hard gluon exchange contributions [23, 25, 28], such that the baryonic form factor is given by a convolution of two distribution amplitudes with a hard scattering kernel. In this case, the same logic applies as for inclusive DIS processes, i.e., the interaction between the electron and the nucleon can be pictured as electron-quark scattering in the infinite-momentum frame. As the hit quark has obtained a large transverse momentum it must exchange gluons with the remaining quarks in order

to merge into an outgoing baryon again. The fact that all incoming and outgoing quarks within the elastic process are confined in color-singlet states cancels potential soft interactions between the initial and final quarks in the scattering kernel and enables a Fock state expansion of the involved hadronic wave functions [23]. On the light-cone, the leading term of this expansion is given by the valence Fock state, i.e., the Fock state with the minimal number of constituent quarks for the respective hadron. As each gluonic exchange involves an additional factor of α_s/Q^2 in the hard scattering kernel, higher non-valence Fock states can be neglected. In this picture, the probability amplitude to observe a many-parton state confined into a small transverse volume is suppressed [29]. As a result, the information content obtained from distribution amplitudes is complementary to that of parton distribution functions: While a PDF always describes the hadron as a whole and does not discriminate between Fock states, a distribution amplitude corresponds to the probability amplitude to find the partons with a certain momentum distribution within a single Fock state. At experimentally achievable intermediate values of Q^2, the small prefactors of the perturbative calculation cause soft contributions to dominate the behavior of hadronic form factors. In order to account for this, light-cone sum rules (LCSR) have successfully been applied to both meson [30] and baryon [31] form factors at intermediate momentum transfers.

The main goal of this thesis is the determination of hadron distribution amplitudes using lattice QCD simulations. The advent of lattice QCD can be dated to 1974 when Wilson published the first formulation of gauge theories on a discretized space-time lattice [32]. This new approach, however, did not fully establish itself until 1979, when Creutz et al. [33] and Wilson [34] showed how to calculate hadronic observables by purely statistical computer simulations. This was immediately followed by successful attempts to calculate the SU(2) static quark-antiquark potential [35] as well as various hadron masses [36,37] on the lattice. Nowadays, lattice QCD is accepted as *the* tool to investigate non-perturbative phenomena and provides high-precision results due to a combination of sophisticated algorithms [38] and ever growing processing power. The first attempts to calculate distribution amplitudes on a lattice were conducted for the second moment $\langle \xi^2 \rangle$ of the pion DA more than 30 years ago [39,40]. In the meantime, lattice results have been obtained for various hadrons, including the pion, the kaon, the rho and the nucleon [41–44]. In this work, we will present results of multiple recent lattice studies, including the first calculation of the DAs of the baryon octet, a calculation of the second moments of the rho meson as well as a calculation of the pion DA using a new smearing technique. The outline of this work is structured as follows: The 2nd chapter introduces both, QCD in the continuum as well as QCD on the lattice. The 3rd chapter explains the utilised simulation methods with a focus on the lattice ensembles of the CLS effort. Chapter 4 is dedicated to baryon distribution amplitudes and presents a $N_f = 2 + 1$ calculation of the zeroth and first moments

of the DAs of the baryon octet. Chapter 5 is devoted to meson distribution amplitudes and is divided into two parts: Section 5.1 introduces a new smearing technique for the second moments of the distribution amplitude of the pseudoscalar pion. Subsequently, the results of a recent $N_f = 2$ study of the DAs of the ρ-meson are presented in section 5.2. Chapter 6 concludes this thesis by giving a short summary as well as an outlook for future developments.

2 Quantum chromodynamics on the lattice

2.1 Continuum formulation

This section is dedicated to the fundamentals of QCD in the continuum and focuses on the derivation of the classical QCD Lagrangian as a starting point for the lattice discretization in section 2.3. Since we only consider gauge-invariant observables on the lattice, we do not discuss the Faddeev-Popov method [45] and the BRST quantization [46–49] but refer the interested reader to the textbooks [50, 51].

QCD is a non-abelian gauge field theory with the special unitary group $\mathrm{SU}(3)_c$ as its underlying gauge group. Hence the $3^2 - 1$ independent generators give rise to 8 massless spin 1 gauge bosons, the gluon fields A^a_μ ($a = 1, \ldots, 8$). The QCD Lagrangian $\mathcal{L}_{\mathrm{QCD}}$ can be constructed by applying the gauge principle with respect to the color group $\mathrm{SU}(3)_c$ to the Lagrangian $\mathcal{L}_{\mathrm{free}}$ of a free fermionic spin 1/2 quark field ψ of single flavor:

$$\mathcal{L}_{\mathrm{free}} = \sum_{i,i'} \sum_{\alpha\alpha'} \bar{\psi}^i_\alpha \big(i \not{\partial}^{ii'}_{\alpha\alpha'} - m\delta^{ii'}\delta_{\alpha\alpha'} \big) \psi^{i'}_{\alpha'} \,, \tag{2.1}$$

with $\not{\partial} = \partial_\mu \gamma^\mu$, $\bar{\psi} = \psi^\dagger \gamma^0$, the Dirac-spinor index $\alpha = 1, \ldots, 4$ and color $i = 1, 2, 3$. Due to the partial derivatives, eq. (2.1) is not invariant under the local gauge transformation

$$\psi(x) \to \psi'(x) = \Omega(x)\psi(x) \,, \tag{2.2}$$

where $\Omega(x) = e^{i \sum_{a=1}^{8} \theta^a(x) t^a} \in \mathrm{SU}(3)_c$. In the fundamental representation, the generators t^a of $\mathrm{SU}(3)$ can be expressed as $t^a = \frac{\lambda^a}{2}$, where the λ^a are the traceless Hermitian Gell-Mann matrices as introduced in ref. [52]. We replace the partial derivatives in eq. (2.1) by the covariant derivatives

$$D_\mu = \partial_\mu + i A^a_\mu t^a \equiv \partial_\mu + i A_\mu \,, \tag{2.3}$$

where $A_\mu \equiv A^a_\mu t^a$. As a result, the fermionic Lagrangian,

$$\mathcal{L}_F = \sum_{i,i'} \sum_{\alpha\alpha'} \bar{\psi}^i_\alpha \big(i \not{D}^{ii'}_{\alpha\alpha'} - m\delta^{ii'}\delta_{\alpha\alpha'} \big) \psi^{i'}_{\alpha'} \,, \tag{2.4}$$

is now gauge invariant if the gauge potential A_μ transforms as

$$A_\mu \to A'_\mu = \Omega A_\mu \Omega^\dagger + i(\partial_\mu \Omega)\Omega^\dagger \,. \tag{2.5}$$

In order to describe the dynamics of the gluon fields, the final Lagrangian must also contain a kinetic term which is only composed of the gauge fields A_μ. For this purpose, similar to QED, one defines the non-abelian field strength tensor

$$F_{\mu\nu} = \partial_\mu A_\nu - \partial_\nu A_\mu + i[A_\mu, A_\nu] = -i[D_\mu, D_\nu] \,. \tag{2.6}$$

Using that $\mathrm{Tr}\big(\lambda^a \lambda^b\big) = 2\delta^{ab}$, one obtains the gluon Lagrangian as

$$\mathcal{L}_\mathrm{G} = -\frac{1}{4g^2} F^a_{\mu\nu} F^{a\mu\nu} = -\frac{1}{2g^2}\,\mathrm{Tr}\big(F_{\mu\nu}F^{\mu\nu}\big)\,, \tag{2.7}$$

where g is the gauge coupling and again $F_{\mu\nu} = F^a_{\mu\nu} t^a$. As already mentioned in the introduction, the Standard Model involves six quark flavors, ($f = u, d, s, c, b, t$), such that we now can obtain the final QCD Lagrangian, which is by construction invariant under local $\mathrm{SU}(3)_c$ gauge transformations:

$$\begin{aligned}
\mathcal{L}_\mathrm{QCD} &= \mathcal{L}_F + \mathcal{L}_G \\
&= \sum_f \sum_{i,i'} \sum_{\alpha,\alpha'} \bar{\psi}_f{}^i_\alpha \big(i\not{D}^{ii'}_{\alpha\alpha'} - m_f \delta^{ii'}\delta_{\alpha\alpha'}\big)\psi_f{}^{i'}_{\alpha'} - \frac{1}{2g^2}\,\mathrm{Tr}\big(F_{\mu\nu}F^{\mu\nu}\big) \\
&= \sum_f \bar{\psi}_f(x)\big(i\not{D} - m_f\big)\psi_f(x) - \frac{1}{2g^2}\,\mathrm{Tr}\big(F_{\mu\nu}F^{\mu\nu}\big)\,.
\end{aligned} \tag{2.8}$$

The QCD vacuum is highly non-trivial and contains infinitely many vacuum states [53], such that, in general, eq. (2.8) has to be complemented by another gauge-invariant term which governs the vacuum topology. This so-called θ-term is of the form

$$\mathcal{L}_\theta = \frac{\theta}{64\pi^2}\epsilon_{\mu\nu\rho\sigma} F^{a\mu\nu} F^{a\rho\sigma} = \frac{\theta}{32\pi^2} F^{a\mu\nu}\tilde{F}^a_{\mu\nu}\,. \tag{2.9}$$

Here θ is real and $\tilde{F}^a_{\mu\nu} = \frac{1}{2}\epsilon_{\mu\nu\rho\sigma}F^{a\rho\sigma}$ is the dual field strength tensor. As $\epsilon_{\mu\nu\rho\sigma}$ is a pseudotensor, this term acquires a minus sign under parity transformations and thus would violate $\mathcal{P}$ and $\mathcal{CP}$ symmetry. Experimentally, the θ-term can best be probed by measurements of the neutron electric dipole moment (nEDM). To satisfy experimental bounds on the nEDM [54–58], the θ-parameter has to be very small, $\theta \leq 10^{-10}$, and will be neglected in the following. The unexplained smallness of θ poses a fine-tuning problem that leads to the famous strong CP problem. A proposed solution is given by the Peccei-Quinn mechanism [59], which introduces pseudoscalar axions as a consequence of the spontaneously broken $U(1)$ Peccei-Quinn symmetry.

2.2 Euclidean space-time

Since the indefinite metric of QCD in Minkowski space gives rise to n-point correlation functions that oscillate in time, lattice calculations are carried out in Euclidean space-time. This is achieved by a so-called Wick rotation, an analytical continuation of the time component to imaginary values,

$$t \to it\,, \tag{2.10}$$

which was first applied by Dyson to avoid poles in contour integrals in QED [60]. The Minkowski and Euclidean space-time coordinates are then connected in the following way:

$$x_i^E = x^i \;\; = -x_i\,, \tag{2.11a}$$
$$x_4^E = ix^0 = ix_0\,. \tag{2.11b}$$

For example, this means with respect to the gluon Lagrangian that

$$\mathcal{L}_G = -\frac{1}{2g^2}\,\mathrm{Tr}\big(F_{\mu\nu}F^{\mu\nu}\big) = -\frac{1}{2g^2}\,\mathrm{Tr}\big(F^E_{\mu\nu}F^E_{\mu\nu}\big) = -\mathcal{L}_G^E\,, \tag{2.12}$$

such that the action functional gives

$$S_G = \int d^4x\,\mathcal{L}_G = \int dx^0 \int d^3x\,\mathcal{L}_G = i\int dx_4^E \int d^3x^E\,\mathcal{L}_G^E = iS_G^E\,, \tag{2.13}$$

and this "Wick rotation" effectively yields

$$e^{iS_G} \to e^{-S_G^E}\,. \tag{2.14}$$

It is possible to recover the Hilbert space quantum field theory from a Euclidean field theory if certain conditions, such as reflection positivity, are fulfilled [61], guaranteeing the Wick rotation to be a well-defined isomorphism between Minkowski and Euclidean space-time theories. The Wick rotation connects the Euclidean field theory to classical statistical mechanics. The direct equivalence between both theories can be illustrated by considering the similarities between the Boltzmann weight factor and the Feynman weight for amplitudes:

$$e^{-S} \Longleftrightarrow e^{-\beta H}\,. \tag{2.15}$$

Recognizing the impact of eq. (2.15) is crucial for the understanding of lattice QCD, as this equivalence allows us to attack problems of the field theory with already established methods of statistical mechanics. As an illustrative example, the calculation of the vacuum

expectation value $\langle 0|\mathcal{O}|0\rangle$ of an observable $\mathcal{O}$ on the lattice corresponds to the calculation of the canonical ensemble average $\langle O\rangle$ of an observable O in classical statistical mechanics.

2.3 Lattice fermion actions

An introduction to lattice QCD can be found in many textbooks on lattice gauge theories or quantum field theories. In the next sections we follow the introductory presentations of refs. [62–64].

We begin by considering the four-dimensional lattice ℓ of size $N_s^3 N_t$, which contains N_s points in each spatial direction and N_t points in the time direction. The vectors n_μ form the grid points of the lattice, which are separated by the dimensional lattice spacing a from their neighbours and fulfill

$$\ell = \Big\{ n \in \big(n_x, n_y, n_z, n_t\big) \mid n_x, n_y, n_z = 0, \ldots, N_s - 1; n_t = 0, \ldots, N_t - 1 \Big\}, \tag{2.16}$$

such that physical space-time coordinates are recovered by $x_\mu = a n_\mu$. In particular we will often refer to the lattice time $t = a n_t$, the spatial extent $L = a N_s$ and the time extent $T = a N_t$ in the following.

2.3.1 Naive fermion action

Having defined the raw lattice ℓ, our goal is now to construct a discretized lattice version of the Euclidean fermionic action that approaches the Euclidean continuum version

$$S_F = \int d^4x \; \overline{\psi}(x) \Big(\gamma_\mu \big(\partial_\mu + i A_\mu(x) \big) + m \Big) \psi(x) \,, \tag{2.17}$$

in the limit $a \to 0$. In order to achieve this, we proceed in a similar constructive manner as for the derivation of the QCD Lagrangian in section 2.1. On the lattice, the continuous integral over the four-dimensional space-time of eq. (2.17) becomes a sum over all points of ℓ such that

$$\int d^4x \to a^4 \sum_x \,. \tag{2.18}$$

Furthermore, we symmetrically discretize the partial derivative that acts on the fermionic fields to get

$$\partial_\mu \psi(x) = \frac{\psi(x + a\hat{\mu}) - \psi(x - a\hat{\mu})}{2a} \,, \tag{2.19}$$

where $\hat{\mu}$ denotes the unit vector in the μ direction. In this way, we obtain an expression for the free lattice action, similar to the free continuum Lagrangian in eq. (2.1):

$$S_{\text{free}}^{\text{lat.}} = a^4 \sum_x \overline{\psi}(x)\Big(\sum_{\mu=1}^{4} \gamma_\mu \frac{\psi(x+a\hat{\mu}) - \psi(x-a\hat{\mu})}{2a} + m\psi(x)\Big)\,. \tag{2.20}$$

As in the continuum case, due to the partial derivatives, this expression is not invariant under local gauge rotations defined in eq. (2.2), since

$$\overline{\psi}'(x)\psi'(x+a\hat{\mu}) = \overline{\psi}(x)\Omega^\dagger(x)\Omega(x+a\hat{\mu})\psi(x+a\hat{\mu})\,. \tag{2.21}$$

In the continuum, gauge invariance is restored in eq. (2.3) by replacing the partial derivatives with covariant derivatives which contain the gluon fields A_μ^a. On the lattice, the covariant derivatives are achieved by introducing the fields $U_\mu(x)$, which transform as

$$U'_\mu(x) = \Omega(x)U_\mu(x)\Omega^\dagger(x+a\hat{\mu})\,, \tag{2.22}$$

such that

$$\overline{\psi}'(x)U'_\mu(x)\psi'(x+a\hat{\mu}) = \overline{\psi}(x)\Omega^\dagger(x)U'_\mu(x)\Omega(x+a\hat{\mu})\psi(x+a\hat{\mu}) \tag{2.23}$$

becomes gauge invariant. As an element of SU(3), the gauge field $U_\mu(x)$ connects the two neighbouring grid points x and $x+a\hat{\mu}$, which gives rise to its name as *gauge link*. The gauge link $U_{-\mu}(x+a\hat{\mu})$, which connects the point $x+a\hat{\mu}$ with x, and its oppositely orientated counterpart $U_\mu(x)$, which connects the point x with $x+a\hat{\mu}$, are related by

$$U_{-\mu}(x+a\hat{\mu}) = U_\mu^\dagger(x)\,. \tag{2.24}$$

We now introduce the lattice gauge fields $A_\mu(x)$ by defining

$$U_\mu(x) = \exp(iaA_\mu(x))\,. \tag{2.25}$$

Finally, for interacting fermions on the lattice we obtain the so-called *naive fermion action*:

$$S_F^{\text{lat.}} = a^4 \sum_x \overline{\psi}(x)\Big(\sum_{\mu=1}^{4} \gamma_\mu \frac{U_\mu(x)\psi(x+a\hat{\mu}) - U_{-\mu}(x)\psi(x-a\hat{\mu})}{2a} + m\psi(x)\Big)\,. \tag{2.26}$$

By using matrix-vector notation, we can rewrite eq. (2.26) to obtain the familiar expression

$$S_F^{\text{lat.}} = a^4 \sum_{\substack{x,y \\ \alpha,\beta,i,j}} \overline{\psi}_\alpha^i(x) D_{\alpha\beta}^{ij}(x,y)\psi_\beta^j(y)\,, \tag{2.27}$$

with the Dirac operator

$$D^{ij}_{\alpha\beta}(x,y) = \sum_{\mu} \big(\gamma_\mu\big)_{\alpha\beta} \frac{U^{ij}_{\mu}(x)\delta_{x+a\hat{\mu},y} - U^{ij}_{-\mu}(x)\delta_{x-a\hat{\mu},y}}{2a} + m\delta_{\alpha\beta}\delta^{ij}\delta_{x,y}\,. \tag{2.28}$$

In order to check the proper continuum behavior of eq. (2.26), we consider the limit of small lattice spacing a, where

$$U_\mu(x) = \mathbb{1} + iaA_\mu(x) + \mathcal{O}(a^2)\,, \tag{2.29}$$

and neglect the $\mathcal{O}(a^2)$ terms to obtain

$$\begin{aligned} S_F^{\text{lat.}} &= a^4 \sum_x \overline{\psi}(x)\Big(\sum_{\mu=1}^{4} \gamma_\mu \frac{\psi(x+a\hat{\mu}) - \psi(x-a\hat{\mu})}{2a} + m\psi(x)\Big) \\ &\quad + ia^4 \sum_x \sum_{\mu=1}^{4} \overline{\psi}(x)\gamma_\mu \frac{1}{2}\Big(A_\mu(x)\psi(x+a\hat{\mu}) + A_\mu(x-a\hat{\mu})\psi(x-a\hat{\mu})\Big) \\ &= S_{\text{free}}^{\text{lat.}} + ia^4\Big(\sum_x \sum_{\mu=1}^{4} \overline{\psi}(x)\gamma_\mu A_\mu(x)\psi(x) + \mathcal{O}(a)\Big)\,. \end{aligned} \tag{2.30}$$

Hence, we recover the continuum action of eq. (2.17) in the limit $a \to 0$ with discretization errors of $\mathcal{O}(a)$.

2.3.2 Wilson fermions

By further investigating the lattice Dirac operator we find that the naive action in eq. (2.26) actually yields 16 Dirac particles instead of one. We start by comparing the lattice quark propagator with its continuum counterpart

$$S(p) = \frac{m - i\gamma_\mu p_\mu}{m^2 + p^2}\,. \tag{2.31}$$

For this, we calculate the Fourier transformation of the naive Dirac operator in eq. (2.28) for the free case and obtain

$$\tilde{D}(p,q) = \delta(p-q)\tilde{D}(p)\,, \tag{2.32}$$

with

$$\tilde{D}(p) = m\mathbb{1} + \frac{i}{a}\sum_\mu \gamma_\mu \sin(p_\mu a)\,. \tag{2.33}$$

For massless fermions, the momentum-space propagator $\tilde{D}^{-1}(p)$ is then given by

$$\tilde{D}^{-1}(p) = \frac{-\frac{i}{a}\sum_\mu \gamma_\mu \sin(p_\mu a)}{\frac{1}{a^2}\sum_\mu \sin(p_\mu a)^2}. \tag{2.34}$$

At first sight, this result seems reassuring as we recover eq. (2.31) for $m = 0$ in the continuum limit

$$\tilde{D}^{-1}(p) \overset{a\to 0}{\to} \frac{-i\gamma_\mu p_\mu}{p^2} = S(p)\Big|_{m=0}. \tag{2.35}$$

However, due to the periodicity of the sine function, eq. (2.34) exhibits a pole whenever each component of p_μ is either 0 or $\frac{\pi}{a}$, which leaves us with $2^4 = 16$ combinations. Beside the natural pole at $p_\mu = 0$, the 15 additional poles are referred to as *doublers*. In order to get rid of these additional poles, Wilson suggested to modify the fermion action by adding the momentum-dependent term

$$m\overline{\psi}\psi \to m\overline{\psi}\psi + \frac{a}{2}\partial_\mu\overline{\psi}\partial_\mu\psi\,, \tag{2.36}$$

to the mass term [63]. Thus the Dirac operator in momentum space gives

$$\tilde{D}(p) = m\mathbb{1} + \frac{1}{a}\sum_\mu \mathbb{1}\Big(1 - \cos(p_\mu a)\Big) + \frac{i}{a}\sum_\mu \gamma_\mu \sin(p_\mu a)\,. \tag{2.37}$$

The so-called *Wilson term* does not give any contribution for the natural pole at $p_\mu = 0$, while it acts as an additional mass term for poles with momentum components $p_\mu = \frac{\pi}{a}$, such that

$$m_{\text{doubler}} \to m_{\text{doubler}} + N_{\pi/a}\frac{2}{a}\,, \tag{2.38}$$

where $N_{\pi/a}$ is the number of momentum components that are equal to $\frac{\pi}{a}$. In this way the mass of the unintended doublers is increased to the order of the cutoff, which decouples them from physics in the continuum. After incorporating eq. (2.36), the lattice Dirac operator of a fermion f in the interacting case can simply be written as

$$D_f{}^{ij}_{\alpha\beta}(x,y) = -\frac{1}{2a}\sum_{\pm\mu}\Big(\mathbb{1} - \gamma_\mu\Big)_{\alpha\beta} U^{ij}_\mu(x)\delta_{x+a\hat{\mu},y} + \Big(m_f + \frac{4}{a}\Big)\delta_{\alpha\beta}\delta^{ij}\delta_{x,y}\,, \tag{2.39}$$

where for convenience we introduced the compact notation

$$\sum_{\pm\mu} = \sum_{\mu=\pm 1}^{\pm 4}\,, \tag{2.40a}$$

$$\gamma_{-\mu} = -\gamma_\mu\,. \tag{2.40b}$$

An important symmetry of the Wilson Dirac operator is the so-called γ_5-Hermiticity

$$D^\dagger = \gamma_5 D \gamma_5 \,, \tag{2.41}$$

which also holds for its inverse such that

$$D^{-1\,\dagger} = \gamma_5 D^{-1} \gamma_5 \,. \tag{2.42}$$

Eq. (2.41) also means that the eigenvalues of the Wilson Dirac operator are either real or complex conjugate pairs as

$$\det\big(D - \lambda \mathbb{1}\big) = \det\big(D^\dagger - \lambda \mathbb{1}\big) = \det\big(D - \lambda^\star \mathbb{1}\big)^\star \,. \tag{2.43}$$

Finally, the Wilson fermion action for multiple flavors is given by

$$S_F = \sum_f a^4 \sum_{\substack{x,y \\ \alpha,\beta,i,j}} \overline{\psi}_{f\,\alpha}^{\,i}(x) D_{f\,\alpha\beta}^{ij}(x,y) \psi_{f\,\beta}^{\,j}(y) \,. \tag{2.44}$$

2.3.3 Sheikholeslami–Wohlert improvement

The fermion lattice action in eq. (2.44) suffers from discretization errors of $\mathcal{O}(a)$ which distort the lattice results and subsequent continuum extrapolations. In this section we therefore derive the counterterms to the lattice action which are required for an on-shell $\mathcal{O}(a)$ improvement. Following [65,66], we describe the lattice theory for finite a as a local effective theory which recovers the continuum action S_0 in the limit $a \to 0$ such that

$$S_{\text{eff.}} = S_0 + a S_1 + a^2 S_2 + \dots \,, \tag{2.45}$$

where

$$S_k = \int d^4x \, \mathcal{L}_k(x) \,. \tag{2.46}$$

The so-called correction terms $\mathcal{L}_{k>0}(x)$ are of dimension $4+k$ and contain additional powers of the mass or additional derivatives. For an $\mathcal{O}(a)$ improvement we want to identify and cancel the $\mathcal{L}_1$ contribution and thus consider only fields with an energy dimension of 5. In addition, the resulting terms should be gauge invariant and respect the space-time and charge conjugation symmetries of the lattice. It turns out that $\mathcal{L}_1$ must be a linear

combination of the following 5 fields:

$$\mathcal{O}_1 = \overline{\psi}\sigma_{\mu\nu}F_{\mu\nu}\psi\,, \tag{2.47a}$$
$$\mathcal{O}_2 = \overline{\psi}\vec{D}_\mu\vec{D}_\mu\psi + \overline{\psi}\overleftarrow{D}_\mu\overleftarrow{D}_\mu\psi\,, \tag{2.47b}$$
$$\mathcal{O}_3 = m\,\mathrm{Tr}\big(F_{\mu\nu}F_{\mu\nu}\big)\,, \tag{2.47c}$$
$$\mathcal{O}_4 = m\overline{\psi}\gamma_\mu\vec{D}_\mu\psi - m\overline{\psi}\overleftarrow{D}_\mu\gamma_\mu\psi\,, \tag{2.47d}$$
$$\mathcal{O}_5 = m^2\overline{\psi}\psi\,. \tag{2.47e}$$

Using the field equations of the continuum theory allows us to eliminate eq. (2.47b) and eq. (2.47d), which further reduces the number of possible fields. We now want to improve our fermion action by adding a counterterm δS to the Wilson action such that $\mathcal{L}_1$ is eliminated and thus the $\mathcal{O}(a)$ discretization effects are canceled. The counterterm δS can only be composed of the 3 remaining fields:

$$\delta S^{\text{lat.}} = a^5\sum_x\Big(c_1\mathcal{O}_1^{\text{lat.}}(x) + c_3\mathcal{O}_3^{\text{lat.}}(x) + c_5\mathcal{O}_5^{\text{lat.}}(x)\Big)\,, \tag{2.48}$$

where $\mathcal{O}_i^{\text{lat.}}$ is the lattice version of the respective field in eqs. (2.47). The structures $\mathrm{Tr}\big(F_{\mu\nu}F_{\mu\nu}\big)$ and $\overline{\psi}\psi$ already appear in the Wilson gauge and Wilson fermion action and can be accounted for by a renormalization of the bare coupling and mass. Therefore it is only necessary to add one term with the structure of eq. (2.47a) and we obtain the counterterm

$$\delta S^{\text{lat.}}[U,\overline{\psi},\psi] = a^5\sum_x c_{\text{sw}}\overline{\psi}(x)\frac{1}{2}\sigma_{\mu\nu}F_{\mu\nu}^{\text{lat.}}(x)\psi(x)\,, \tag{2.49}$$

where c_{sw} is the so-called *Sheikholeslami–Wohlert coefficient*, which is real and can be calculated numerically, cf. [67]. The lattice version of the Euclidean field strength tensor can be written as

$$F_{\mu\nu}^{\text{lat.}}(x) = -\frac{i}{8a^2}\Big(Q_{\mu\nu}(x) - Q_{\nu\mu}(x)\Big)\,, \tag{2.50}$$

with the sum over all adjacent plaquettes

$$Q_{\mu\nu}(x) = U_{\mu\nu}(x) + U_{\nu-\mu}(x) + U_{-\mu-\nu}(x) + U_{-\nu\mu}(x)\,. \tag{2.51}$$

Due to its four-fold symmetry in a two-dimensional plane, eq. (2.49) is referred to as *clover term*.

2.4 Lattice gauge actions

2.4.1 Wilson gauge action

The construction of the gluon lattice action is governed by three guidelines: The action has to be gauge invariant, it can only consist of gauge fields and it has to yield the continuum gauge action

$$S_G = \frac{1}{2g^2} \int d^4x \, \mathrm{Tr}\Big(F_{\mu\nu}(x) F_{\mu\nu}(x) \Big), \tag{2.52}$$

in the limit $a \to 0$. Equivalent definitions in terms of the inverse squared coupling $\beta = \frac{6}{g^2}$ are also found in the literature. We first consider the smallest closed loop $U_{\mu\nu}(x)$ on the lattice:

$$U_{\mu\nu}(x) = U_\mu(x) U_\nu(x + a\hat{\mu}) U_\mu^\dagger(x + a\hat{\nu}) U_\nu^\dagger(x) \,. \tag{2.53}$$

$U_{\mu\nu}(x)$ can be illustrated as a square along the four gauge links and thus is referred to as *plaquette* in the literature. The trace of every closed loop of gauge links is gauge invariant due to the cyclic properties of the trace. Therefore we define the so-called *Wilson gauge action* [32] as a sum over all possible plaquettes:

$$S_G^{\text{lat.}}[U] = \frac{2}{g^2} \sum_x \sum_{\mu<\nu} \mathrm{Re}\,\mathrm{Tr}\Big(\mathbb{1} - U_{\mu\nu}(x) \Big). \tag{2.54}$$

The behavior in the continuum limit can be checked by applying the Baker-Campbell-Hausdorff formula

$$\exp(A)\exp(B) = \exp\Big(A + B + \frac{1}{2}\big[A, B\big] + \dots \Big), \tag{2.55}$$

together with the Taylor expansion

$$A_\nu(x + a\hat{\mu}) = A_\nu(x) + a\partial_\mu A_\nu(x) + \mathcal{O}(a^2) \,. \tag{2.56}$$

As a result, we get:

$$\begin{aligned} U_{\mu\nu}(x) &= \exp\Big(ia^2 \big(\partial_\mu A_\nu(x) - \partial_\nu A_\mu(x) + i\big[A_\mu(x), A_\nu(x)\big] \big) + \mathcal{O}(a^3) \Big) \\ &= \exp\Big(ia^2 F_{\mu\nu}(x) + \mathcal{O}(a^3) \Big). \end{aligned} \tag{2.57}$$

We insert this expression for $U_{\mu\nu}$ into eq. (2.54) and obtain

$$S_G^{\text{lat.}}[U] = \frac{a^4}{2g^2} \sum_{x\in\ell} \sum_{\mu,\nu} \mathrm{Tr}\Big(F_{\mu\nu} F_{\mu\nu} \Big) + \mathcal{O}(a^2), \tag{2.58}$$

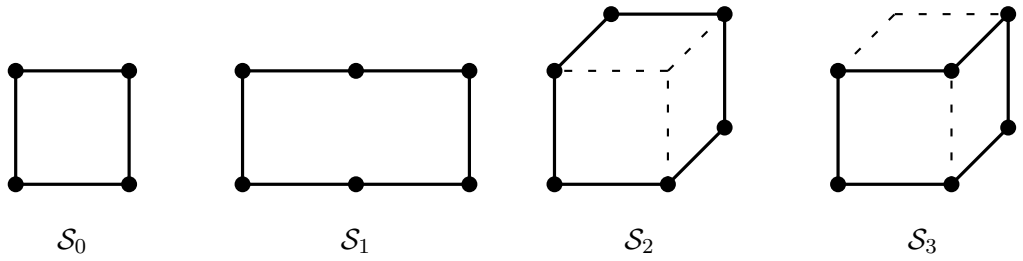

Figure 2.1: Elementary loops contained in each set $\mathcal{S}_i$.

which yields eq. (2.52) for $a \to 0$.

2.4.2 Lüscher–Weisz gauge action

Similar to the Sheikholeslami–Wohlert improvement for the fermion action, the Wilson gauge action can be improved by adding a linear combination of 3 operators of dimension 6 to the standard plaquette. We follow [68] and make the ansatz

$$S_G^{\text{lat.}}[U] = \frac{2}{g^2} \sum_{i=0}^{3} c_i(g^2) \sum_{\mathcal{C} \in \mathcal{S}_i} \operatorname{Re} \operatorname{Tr}\big[\mathbb{1} - U(\mathcal{C})\big] , \tag{2.59}$$

where the $\mathcal{S}_i$ denote the sets of elementary loops $\mathcal{C}$ of a certain kind, while $U(\mathcal{C})$ is the oriented product of link variables $U_\mu(x)$ along $\mathcal{C}$. Figure 2.1 shows a sketch of the possible elementary loops $\mathcal{C}$ that appear in eq. (2.59). In compliance with eq. (2.54), $\mathcal{S}_0$ is the set of oriented 1×1 plaquettes, while $\mathcal{S}_1$ contains all 1×2 rectangular loops. $\mathcal{S}_2$ and $\mathcal{S}_3$ are more complicated and extend in 3 dimensions, cf. figure 2.1. In order to achieve a tree-level improved action, Lüscher and Weisz showed that one coefficient can be chosen freely [69], such that to lowest order in g^2, the most general on-shell improved action is given by

$$c_0(0) = \frac{5}{3} - 24x , \tag{2.60a}$$

$$c_1(0) = -\frac{1}{12} + x , \tag{2.60b}$$

$$c_2(0) = 0 , \tag{2.60c}$$

$$c_3(0) = x . \tag{2.60d}$$

For the reader's convenience we will suppress the superscript *lat.* in the following and always use the lattice action unless stated explicitly otherwise.

2.5 Correlation functions and path integrals

2.5.1 Correlators

Having constructed the appropriate QCD action on the lattice, we will now establish a connection between the observables of interest and the numerically evaluable path integral on the lattice. To this end we define the Euclidean correlator of two operators $\hat{\mathcal{O}}_1$ and $\hat{\mathcal{O}}_2$ as

$$\langle O_2(t)O_1(0)\rangle = \frac{1}{Z}\,\mathrm{Tr}\big[e^{-(T-t)\hat{H}}\hat{O}_2 e^{-t\hat{H}}\hat{O}_1\big]\,, \tag{2.61}$$

with the Hamiltonian of the system $\hat{H}$ and the partition function $Z = \mathrm{Tr}\big[e^{-T\hat{H}}\big]$. The field operators appearing in eq. (2.61) can measure observables or create and annihilate particles with certain quantum numbers. We will denote $\hat{O}_H^\dagger$ as the operator that creates a state with the quantum numbers of the hadron H, while its adjoint partner $\hat{O}_H$ annihilates this state or creates a state with the quantum numbers of its antiparticle $\overline{H}$. Using the eigenvalue equation

$$\hat{H}|n\rangle = E_n|n\rangle\,, \tag{2.62}$$

we expand eq. (2.61) by inserting a complete set of states. After normalizing the vacuum energy E_0 to zero we obtain the limit

$$\lim_{T\to\infty}\langle O_2(t)O_2(0)\rangle = \sum_n \langle 0|\hat{O}_2|n\rangle\langle n|\hat{O}_1|0\rangle e^{-tE_n}\,. \tag{2.63}$$

Let H be a hadron with the corresponding annihilation and creation operators O_H and $O_H^\dagger$, respectively. For this case eq. (2.63) yields

$$\lim_{T\to\infty}\langle O_H(t)O_H^\dagger(0)\rangle = |\langle H|\hat{O}_H^\dagger|0\rangle|^2 e^{-tE_H} + |\langle H'|\hat{O}_H^\dagger|0\rangle|^2 e^{-tE_{H'}} + \dots\,, \tag{2.64}$$

where $|H\rangle$ denotes the ground state of the hadron H, while $|H'\rangle, |H''\rangle, \dots$ denote excited states with the quantum numbers of H. All states which possess these quantum numbers contribute to the correlator with a coefficient that falls off exponentially with the respective energy of the state. All other contributions from states that do not possess the quantum numbers of the hadron H vanish. For high lattice times t, the excited states have sufficiently decayed and only the ground state contributes, which allows us to analyse its energy and matrix element.

In order to calculate the Euclidean correlator on the lattice, we employ the Feynman

path integral formalism such that

$$\langle O_2(t)O_1(0)\rangle = \frac{1}{Z}\int \mathcal{D}[\psi,\overline{\psi}]\mathcal{D}[U]e^{-S_F[\psi,\overline{\psi},U]-S_G[U]}O_2[\psi,\overline{\psi},U]O_1[\psi,\overline{\psi},U]\,, \tag{2.65}$$

with the partition function

$$Z = \int \mathcal{D}[\psi,\overline{\psi}]\mathcal{D}[U]e^{-S_F[\psi,\overline{\psi},U]-S_G[U]}\,. \tag{2.66}$$

The integral in eq. (2.65) runs over all values of the quark fields ψ and $\bar{\psi}$, as well as over the gluon fields U at every space-time point. The corresponding integral measures are products of measures of all quark fields and all gauge links

$$\mathcal{D}[\psi,\overline{\psi}] = \prod_x \prod_{f,\alpha,i} d\psi_{f}{}^{i}_{\alpha}(x) d\bar{\psi}_{f}{}^{i}_{\alpha}(x)\,, \tag{2.67a}$$

$$\mathcal{D}[U] = \prod_x \prod_{\mu=1}^{4} dU_\mu(x)\,, \tag{2.67b}$$

where dU denotes the normalized Haar measure on SU(3) [63, 70].

2.5.2 Grassmann integrals

Due to Pauli's exclusion principle, the integration of the fermionic fields ψ and $\overline{\psi}$ is inherently different from the integration of the gauge links U. Let O be a generic product of operators

$$O = \prod_{n=1}^{N} \psi^{i_n}_{\alpha_n}(x_n)\overline{\psi}^{j_n}_{\beta_n}(y_n)\,, \tag{2.68}$$

we then rewrite eq. (2.65) such that

$$\langle O\rangle = \frac{1}{Z}\int \mathcal{D}[U]e^{-S_G[U]}Z_F[U]\langle O\rangle_F[U]\,, \tag{2.69}$$

with the fermionic part of the correlator

$$\langle O\rangle_F[U] = \frac{1}{Z_F[U]}\int \mathcal{D}[\psi,\overline{\psi}]e^{-S_F[\psi,\overline{\psi},U]}O[\psi,\overline{\psi},U]\,, \tag{2.70}$$

and the fermionic partition function

$$Z_F[U] = \int \mathcal{D}[\psi,\overline{\psi}]e^{-S_F[\psi,\overline{\psi},U]}\,. \tag{2.71}$$

In this way we separate the fermionic and bosonic integrals in order to account for their different nature. The fermionic fields $\overline{\psi}$ and ψ have to obey Fermi statistics, which means that $\langle O \rangle$ has to acquire a minus sign if the quantum numbers of two fermions are interchanged. We implement this correct anti-commutation behavior by introducing $\overline{\psi}$ and ψ as Grassmann numbers with the properties

$$\left\{\psi^i_\alpha(x), \psi^j_\beta(y)\right\} = 0\,, \tag{2.72a}$$

$$\frac{\partial}{\partial \psi^j_\beta(y)} \psi^i_\alpha(x) = \int d\psi^j_\beta(y)\, \psi^i_\alpha(x) = \delta_{\alpha\beta}\delta^{ij}\delta_{x,y}\,. \tag{2.72b}$$

Realizing these Grassmann numbers in a computer simulation would be tedious but in practice this is not required anyway as the fermionic fields can be integrated out before the simulation. Using the properties (2.72), the fermionic partition function can be expressed as the determinant of the Dirac operator:

$$\begin{aligned} Z_F[U] &= \int \mathcal{D}[\psi, \overline{\psi}] \exp\Big(-a^4 \sum_{\substack{x,y \\ \alpha,\beta,i,j}} \overline{\psi}^i_\alpha(x) D^{ij}_{\alpha\beta}(x,y) \psi^j_\beta(y)\Big) \\ &= \det(-a^4 D)\,. \end{aligned} \tag{2.73}$$

We use the translational invariance of Grassmannian integration and generalize eq. (2.73) by making the translations $\overline{\psi} \to \overline{\psi} - a^{-4}\overline{\theta}D^{-1}$ and $\psi \to \psi - a^{-4}D^{-1}\theta$ to obtain

$$\begin{aligned} &\int \mathcal{D}[\psi, \overline{\psi}] \exp\Big(-a^4 \sum_{\substack{x,y \\ \alpha,\beta,i,j}} \overline{\psi}^i_\alpha(x) D^{ij}_{\alpha\beta}(x,y) \psi^j_\beta(y) + \sum_{\substack{x \\ \alpha,i}} \overline{\theta}^i_\alpha(x) \psi^i_\alpha(x) + \sum_{\substack{x \\ \alpha,i}} \overline{\psi}^i_\alpha(x) \theta^i_\alpha(x)\Big) \\ &\quad = \det(-a^4 D) \exp\Big(a^{-4} \sum_{\substack{x,y \\ \alpha,\beta,i,j}} \overline{\theta}^i_\alpha(x) (D^{-1})^{ij}_{\alpha\beta}(x,y) \theta^j_\beta(y)\Big)\,, \end{aligned} \tag{2.74}$$

which we will use as a generating functional for fermions. The inverse of the lattice Dirac operator D^{-1} is referred to as *quark propagator*. By applying derivatives with respect to θ and $\overline{\theta}$ in eq. (2.74) we obtain the so-called Wick theorem:

$$\begin{aligned} &\Big\langle \prod_{n=1}^N \psi^{i_n}_{\alpha_n}(x_n) \overline{\psi}^{j_n}_{\beta_n}(y_n) \Big\rangle_F \\ &\quad = \frac{1}{Z_F} \int \mathcal{D}[\psi, \overline{\psi}] \Big(\prod_{n=1}^N \psi^{i_n}_{\alpha_n}(x_n) \overline{\psi}^{j_n}_{\beta_n}(y_n) \Big) \exp\Big(-a^4 \sum_{\substack{x,y \\ \alpha,\beta,i,j}} \overline{\psi}^i_\alpha(x) D^{ij}_{\alpha\beta}(x,y) \psi^j_\beta(y)\Big) \\ &\quad = \sum_{\pi \in \mathcal{S}_N} \operatorname{sgn}(\pi) \prod_{n=1}^N (a^{-4} D^{-1})^{i_n j_{\pi_n}}_{\alpha_n \beta_{\pi_n}}(x_n, y_{\pi_n})\,. \end{aligned} \tag{2.75}$$

The Wick theorem allows us to reduce products of quark field operators to sums of products of quark propagators, which can be calculated on the lattice, cf. eq. (2.69).

3 Simulation methods

3.1 General idea

In the following we will describe the simulation details and techniques which were used for the lattices analysed in this work. In particular, we will focus on the $N_f = 2+1$ ensembles generated by the Coordinated Lattice Simulations (CLS) community effort.

Having integrated out the fermionic degrees of freedom in section 2.5.2, we are merely left with an integration over the gauge links U. Employing $N_f = 2+1$ dynamical fermions, the corresponding path integral has the form

$$\langle O \rangle = \frac{1}{Z} \int \mathcal{D}[U] e^{-S_G} \det\big(D_u\big) \det\big(D_d\big) \det\big(D_s\big) \langle O \rangle_F. \tag{3.1}$$

Eq. (3.1) is a high-dimensional group integral for each link of the whole lattice and already extremely expensive to calculate for very small lattice sizes. As an illustrative example, we consider a four-dimensional lattice of the size $10 \times 10 \times 10 \times 10$ which contains $4 \cdot 10^4$ gauge links. Each of the SU(3) gauge links contains 8 real parameters, which results in 320000 integrations. Approximating the integral by a mesh of 10 points per integration already yields a sum of 10^{320000} terms [64], which obviously cannot be computed in practice. Therefore, sophisticated numerical methods are needed for the evaluation. Fortunately, due to the direct equivalence between Euclidean field theories and classical statistical mechanics as shown in eq. (2.15), we can use well-established techniques that were initially developed for statistical mechanics systems. In particular we will employ the Metropolis Monte Carlo algorithm, which was introduced in 1953 [71] to numerically handle multi-dimensional integrals for interacting individual molecules and spin systems. Following [72] we introduce the Monte Carlo method for a generic statistical mechanics system. Let $\mathcal{H}$ be the Hamiltonian of the system which is characterized by the set of variables $\mathbf{x}$, while f is the observable of interest. The expectation value of f is given by

$$\langle f \rangle = \frac{\sum_{\mathbf{x}} f(\mathbf{x}) e^{-\beta \mathcal{H}(\mathbf{x})}}{\sum_{\mathbf{x}} e^{-\beta \mathcal{H}(\mathbf{x})}}. \tag{3.2}$$

Using the Monte Carlo method, we approximate $\langle f \rangle$ by the evaluation of the sequence

$$f_n = \frac{\sum_{i=1}^{n} f(\mathbf{x}_i) e^{-\beta \mathcal{H}(\mathbf{x}_i)} P^{-1}(\mathbf{x}_i)}{\sum_{i=1}^{n} e^{-\beta \mathcal{H}(\mathbf{x}_i)} P^{-1}(\mathbf{x}_i)}, \tag{3.3}$$

where the independent configurations $\mathbf{x}_i$ are randomly generated according to the probability distribution $P(\mathbf{x}_i)$. In the limit of infinitely many configurations one recovers the average observable

$$\lim_{n \to \infty} f_n = \langle f \rangle, \tag{3.4}$$

where the errors are of order $\frac{1}{\sqrt{n}}$ for a finite n. The weight $P(\mathbf{x}_i)$ is used to reduce the computing time by choosing configurations close to the mean action with higher probability. This so-called *importance sampling* approach avoids configurations that hardly contribute to the mean values and thus allows one to estimate large sums by a relative small amount of configurations.

In our case, we want to approximate the path integral in eq. (3.1) by evaluating the observable O on N_c gauge field configurations U_i,

$$\langle O \rangle \approx \frac{1}{N_c} \sum_i O[U_i], \tag{3.5}$$

where the U_i are distributed according to the weight

$$P(U) = \frac{1}{Z} e^{-S_G} \det\big(D_u\big) \det\big(D_d\big) \det\big(D_s\big). \tag{3.6}$$

The fermion determinants incorporate the effects of virtual quark loops in the fermionic vacuum. According to Dirac's picture of a fermion sea, these quarks are referred to as *sea quarks*. The lattice Dirac operator $D^{ij}_{\alpha\beta}(x, y)$ is a matrix with $\big(4 \cdot 3 \cdot N_s^3 \cdot N_t\big)^2$ complex entries and thus its determinant is extremely expensive to calculate. Furthermore, the fermion determinant is highly non-local as it depends on the whole gauge field, which further complicates the generation of configurations distributed according to eq. (3.6), especially with one-link update algorithms [62,64]. In the past, fermion determinants were often simply set to unity, which effectively neglects any effects of virtual quark loops except those treated explicitly as "disconnected diagrams", see for example [73,74]. Although this so-called *quenched approximation* is comfortable to simulate, we are in the end interested in the physics that includes dynamical quarks.

3.2 Hybrid Monte Carlo

The Hybrid Monte Carlo (HMC) algorithm [75] allows to generate configurations with dynamical sea quarks by updating all link variables in one step while keeping the acceptance probability high. The computational effort of conventional one-link algorithms scales with the square of the lattice volume V^2, whereas the cost of the HMC is merely proportional to $V^{5/4}$ (see refs. [76, 77]), which enabled dynamical simulations in the first place. Following [78], we will briefly summarize the essential steps of the HMC algorithm. First we consider the auxiliary $\mathfrak{su}(3)$ field

$$\pi_\mu(x) = \pi_\mu^a(x) t^a, \tag{3.7}$$

where $\pi_\mu^a(x)$ are real functions. We interpret π as the canonical momentum of a classical statistical system with the Hamiltonian

$$H(\pi, U) = \frac{1}{2}\pi^\dagger\pi + S(U)\,, \tag{3.8}$$

where $S(U)$ is a not yet specified non-local action and $\pi^\dagger\pi = \sum_{x,\mu} \pi^{\dagger a}_\mu(x)\pi^a_\mu(x)$. Vacuum expectation values with respect to the gauge fields U remain uninfluenced by the field π as

$$\int \mathcal{D}[U]\mathcal{O}(U)e^{-S(U)} \propto \int D[\pi]D[U]\mathcal{O}(U)e^{-H(\pi,U)}\,. \tag{3.9}$$

The time evolution of this classical system is determined by the so-called *molecular-dynamics equations*, which are given by Hamilton's equations

$$\dot{\pi}_\mu(x) = -\frac{\partial S(U)}{\partial U_\mu(x)}\,, \tag{3.10a}$$

$$\dot{U}_\mu(x) = \pi_\mu(x)U_\mu(x)\,. \tag{3.10b}$$

The dot on top of the fields denotes the differentiation with respect to the computer time τ, not to be confused with the time coordinate t of the space-time. The gauge configurations are generated by evolving this classical system via the integration of eqs. (3.10). Starting from configuration $U_\mu(x)$ which is to be updated, the new configuration $U'_\mu(x)$ is generated according to the following algorithm [78]:

(a) Momentum heatbath: Generate the momentum field π randomly from the Gaussian distribution $\exp\left(-\frac{1}{2}\pi^\dagger\pi\right)$.

(b) Molecular-dynamics evolution: Integrate the molecular-dynamics equations from $\tau = 0$ to $\tau = \tau'$ where π and $U = U_0$ are the initial values of the fields.

(c) Metropolis acceptance step: The new field field U' is set to the resulting field $U_{\tau'}$ with the acceptance probability $P = \min\{1, e^{-\delta H(U_0, U_{\tau'})}\}$, otherwise $U' = U$.

3.2.1 Inclusion of the light sea quarks

We still need to specify the action used in eq. (3.8) of the Hybrid Monte Carlo algorithm. Therefore, we first consider the $N_f = 2$ case of two degenerate light sea quarks, where we want to obtain configurations distributed according to

$$P(U) = \frac{1}{Z} \det(D_l) \det(D_l) e^{-S_G(U)}, \tag{3.11}$$

with the light Dirac operator $D_l = D_u = D_u$. We introduce the pseudo-fermionic auxiliary fields $\phi(x)$ to express the determinant as an integral:

$$\det(D_l)^2 \propto \int D[\phi_l, \phi_l^\dagger]\, e^{-S_l(U,\phi)}, \tag{3.12}$$

$$S_l(U, \phi_l) = \phi_l^\dagger (D^\dagger D)^{-1} \phi_l . \tag{3.13}$$

For the HMC algorithm this means that the Hamiltonian is given by

$$H(\pi, U) = \frac{1}{2}\pi^\dagger \pi + S_G(U) + S_l(U, \phi_l), \tag{3.14}$$

and that the first step of the algorithm,

(a) Momentum heatbath: Generate the momentum field π randomly from the Gaussian distribution $\exp(-\frac{1}{2}\pi^\dagger \pi)$.

has to be replaced by

(a′) Momentum heatbath: Generate the momentum field π and the pseudo-fermion field ϕ randomly from the Gaussian distribution $\exp(-\frac{1}{2}\pi^\dagger \pi - S_l(U, \phi_l))$.

3.2.2 Inclusion of the strange sea quarks

Due to the even number of light sea quarks, the contributions from the light determinants are guaranteed to be positive since

$$\det(D_u) \det(D_d) = \det(D_l^2) = \det(D_l^\dagger D_l) \geq 0, \tag{3.15}$$

where γ_5-Hermiticity was employed in the first step. This is not the case for the strange sea quarks and the determinant can become negative for some configurations such that both cases

$$\det(D_s) = \pm |\det(D_s)|, \tag{3.16}$$

can appear. The Rational Hybrid Monte Carlo (RHMC) algorithm [79, 80] circumvents this problem by using an approximation for the positive square root $\sqrt{D_s^\dagger D_s}$ in the HMC algorithm. The strange determinant is factorized such that

$$\det\big(D_s\big) = W_s \det\big(R^{-1}\big)\,, \tag{3.17}$$

where R denotes the Zolotarev optimal rational approximation of the operator $\big(D_s^\dagger D_s\big)^{-1/2}$. The reweighting factor,

$$W_s = \det\big(D_s R\big)\,, \tag{3.18}$$

is used to correct for the numerical error of the approximation. Similar as for the light case, the determinant $\det\big(R^{-1}\big)$ is then represented as a pseudo-fermionic Gaussian integral

$$\det\big(D_s\big) \propto \int D[\phi_s] D[\phi_s^\dagger]\, e^{-S_s(U,\phi)}\,, \tag{3.19}$$

$$S_s(U,\phi_s) = \phi_s^\dagger R \phi_s\,. \tag{3.20}$$

For further details on the method, the reader is referred to refs. [78, 81, 82].

3.3 Ensembles

As most of the results in this work were obtained by analyzing ensembles generated within the CLS effort, we will describe the details of these ensembles in this section, see also [83]. The CLS lattices contain $N_f = 2 + 1$ flavors of sea quarks. The fermions employ the Wilson Dirac operator and the Sheikholeslami–Wohlert term for the $\mathcal{O}(a)$ improvement, introduced in section 2.3.2 and section 2.3.3, respectively. The improvement coefficients c_{sw} have been calculated non-perturbatively in [84]. The gauge action is Lüscher-Weisz improved and corresponds to setting $x = 0$ in eqs. (2.60), such that only the plaquettes contained in $\mathcal{S}_0$ and the rectangles contained in $\mathcal{S}_1$ have to be included with the respective coefficients $c_0 = \frac{5}{3}$ and $c_1 = -\frac{1}{12}$, see section 2.4.2.

3.3.1 Open boundary conditions

One of the goals of the CLS effort is to perform reliable continuum extrapolations, which requires the generation of lattice ensembles with small lattice spacings a. In most lattice simulations, periodic boundary conditions are imposed on the gauge fields in all space-time directions in order to sustain the translational symmetry of the lattice. However, for lattice spacings smaller than 0.05 fm, HMC algorithms can get trapped in sectors of gauge fields with fixed topological charge and lose ergodicity [81]. As a consequence, large undesired autocorrelation times arise for quantities that are related to the topological charge of the

gauge field such as the hadronic matrix elements of pseudoscalar densities [85, 86]. The CLS ensembles avoid this problem by imposing open boundary conditions on the gauge fields in time direction. In this way, the topological charge flows through the boundaries, which makes all the relevant parts of the field space accessible while the physical states and the Hamiltonian remain unchanged [86]. Open boundary conditions are imposed by setting the gauge field tensor $F_{\mu\nu}(x)$ to zero at the boundaries in time direction

$$F_{4k}\big(\mathbf{x}, t = 0\big) = F_{4k}\big(\mathbf{x}, t = T\big) = 0\,. \tag{3.21}$$

Meanwhile, periodic boundary conditions are still imposed on all boundaries in the spatial directions. The price to pay is that open boundary conditions introduce lattice artifacts at sites close to the boundaries which, have to be discarded in the lattice analysis.

3.3.2 Twisted mass reweighting and preconditioning

In section 2.3.2 we showed that the doublers of the naive fermion action decouple from the theory if the Wilson term is added to the action. As a side effect, the Wilson term violates chiral symmetry with effects of $\mathcal{O}(a)$, or $\mathcal{O}(a^2)$ if the action is Sheikholeslami–Wohlert improved. Unlike for the Ginsparg–Wilson Dirac operator, where chiral symmetry is preserved, the spectrum of the Wilson Dirac operator is not protected against gauge fluctuations allowing for arbitrarily small eigenvalues [87]. Employing twisted mass determinant reweighting avoids this problem by introducing a twisted mass term into the action in order to shift the eigenvalues away from zero [88]. The modification of the action is compensated by correcting the gauge configuration with a suitable reweighting factor. In practice, this is implemented by introducing the twisted mass parameter $\mu > 0$ which serves as an infrared regularization such that

$$\det\Big(D_l^\dagger D_l\Big) \to \det\Big(\big(D_l^\dagger D_l + \mu^2\big)^2\big(D_l^\dagger D_l + 2\mu^2\big)^{-1}\Big)\,. \tag{3.22}$$

The reweighting factor W for this choice of regularization is given by

$$W = \det\Big(D_l^\dagger D_l\big(D_l^\dagger D_l + 2\mu^2\big)\big(D_l^\dagger D_l + \mu^2\big)^{-2}\Big)\,. \tag{3.23}$$

The twisted mass determinant reweighting is conveniently combined with an even-odd preconditioning of the Dirac operator [89] in order to accelerate the runs. A lattice point x is considered even or odd if the sum of its coordinates is even or odd. The even-odd preconditioned Dirac operator is assembled such that

$$D = \begin{pmatrix} D_{\mathrm{ee}} & D_{\mathrm{eo}} \\ D_{\mathrm{oe}} & D_{\mathrm{oo}} \end{pmatrix}, \tag{3.24}$$

id	N_s	N_t	m_π [MeV]	m_K [MeV]	$m_\pi L$	$N_c(\times N_{\text{src}})$
H101	32	96	420	420	5.8	2000(×3)
H102	32	96	355	440	4.9	1997(×3)
H105	32	96	280	465	3.9	2833(×3)
C101	48	96	222	474	4.6	1552(×3)

Table 3.1: List of the CLS ensembles used in this work. All lattices feature the inverse squared gauge coupling $\beta = 3.4$, which corresponds to a lattice spacing of $a \approx 0.0857\,\text{fm}$. The number of sources, N_{src}, is the same for all lattices, while the number of available configurations, N_c, varies between $1500 - 2800$. For further details on the generation of the CLS ensembles, the reader may consult refs. [83, 90].

where, for example, D_{eo} contains the hopping terms that connect even and odd sites. Instead of directly solving the Dirac equation

$$D\psi = \eta, \tag{3.25}$$

we follow [78] and consider the preconditioned equation

$$LDR\varphi = L\eta\,, \tag{3.26}$$

with the preconditioners

$$L = \begin{pmatrix} 1 & -D_{\text{eo}}D_{\text{oo}}^{-1} \\ 0 & 1 \end{pmatrix} \qquad \text{and} \qquad R = \begin{pmatrix} 1 & 0 \\ -D_{\text{oo}}^{-1}D_{\text{oe}} & 1 \end{pmatrix}. \tag{3.27}$$

In this way, the Dirac operator can be block-diagonalized such that

$$LDR = \begin{pmatrix} \hat{D} & 0 \\ 0 & D_{\text{oo}} \end{pmatrix}, \tag{3.28}$$

where $\hat{D}$ is the Schur complement of the preconditioned Dirac operator,

$$\hat{D} = D_{\text{ee}} - D_{\text{eo}}D_{\text{oo}}^{-1}D_{\text{oe}}\,. \tag{3.29}$$

Using $\hat{D}$ instead of D is beneficial for the inversion as the condition number of $\hat{D}$ is in most cases less than half the one of D.

3.3.3 CLS ensembles

Following our publication [24], we introduce the specific CLS ensembles used in this work. The lattices will be referred to using their CLS identifier, which is given with the attached properties in table 3.1. As introduced in section 3.3.1, the ensembles employ open

m_π[MeV]	m_π^∞[MeV]	N_s	N_t	$m_\pi L$	$N_c(\times N_{src})$
$\beta = 5.20$, $a = 0.081$ fm, $a^{-1} = 2400$ MeV					
280	278	32	64	3.7	$1999(\times 4)^\dagger$
$\beta = 5.29$, $a = 0.071$ fm, $a^{-1} = 2800$ MeV					
422	422	32	64	4.8	$1998(\times 2)^\dagger$
295	290	32	64	3.4	$1999(\times 1)$
289	290	40	64	4.2	$2028(\times 2)$
290	290	64	64	6.7	$1237(\times 2)^\dagger$
150	150	64	64	3.5	$1599(\times 3)^\dagger$
$\beta = 5.40$, $a = 0.060$ fm, $a^{-1} = 3300$ MeV					
490	488	32	64	4.8	$982(\times 2)$
426	424	32	64	4.2	$1999(\times 2)^\dagger$
260	259	48	64	3.8	$2178(\times 2)$

Table 3.2: Other ensembles analysed in this work. For each ensemble we give the inverse squared coupling β, the pion mass m_π, the finite volume corrected pion mass m_π^∞ determined in [91], the lattice size, the value of $m_\pi L$, the number of configurations N_c and the number of sources N_{src} used on each configuration. The ensembles marked with † were generated on the QPACE systems of the SFB/TRR 55, while the others were generated earlier within the QCDSF collaboration.

boundary conditions for the gauge fields in the temporal direction. They comprise between $N_c \approx 1500$ to $N_c \approx 2800$ configurations that are separated by four Hybrid Monte Carlo molecular dynamics units. For each configuration we carried out measurements with 3 different source positions, $t_{src} = 30a$, $47a$ and $65a$. To enhance the ground state overlap the interpolators are, if required, Wuppertal-smeared [92], employing spatially APE-smeared [93] transporters. In addition, we carried out an additional analysis run for the meson DAs at $t_{src} = 47a$, where we employed a new momentum smearing technique. In order to reduce possible finite volume effects, the spatial extent of all ensembles fulfills $L > 2.7$ fm, such that $m_\pi L \gtrsim 4$. As illustrated in figure 3.1, the quark masses of these lattice ensembles are chosen such that they lie on the $\mathrm{Tr}\, M = 2m_l + m_s = \text{const.}$ trajectory, which implies that they fulfill

$$\frac{2m_K^2 + m_\pi^2}{X_b} = \text{phys.}\,, \tag{3.30}$$

where $X_b = (2m_N + 3m_\Sigma + 2m_\Xi + m_\Lambda)/8$ refers to the average octet baryon mass. Eq. (3.30) means that the normalized average quadratic meson mass is set to its physical value. This

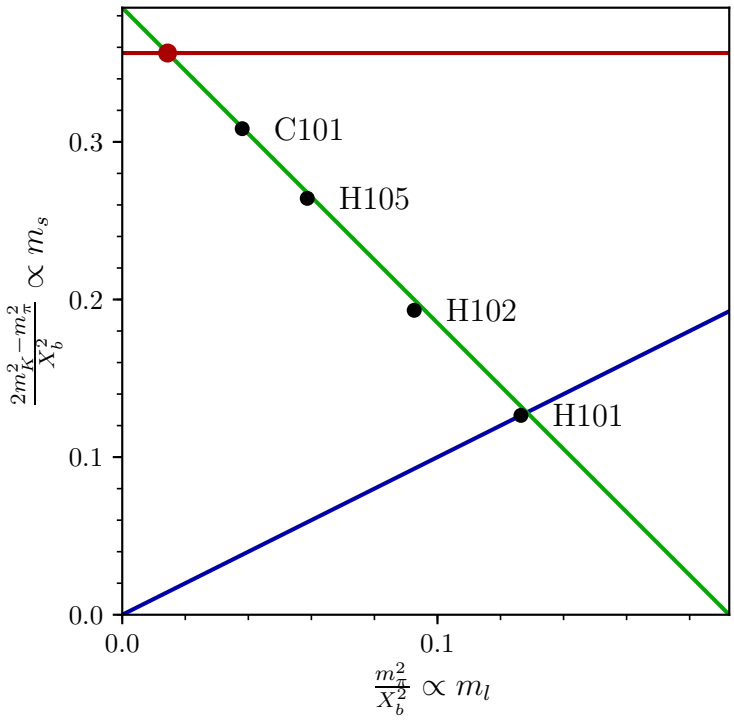

Figure 3.1: Plot showing the position of the used lattice ensembles in the meson mass landscape. The lattices lie on the green $\mathrm{Tr}\, M$ = const. line. The flavor symmetric line (blue) and the line of physical strange quark mass (red) are also shown.

corresponds to an approximately average quadratic mean quark mass

$$2m_l + m_s \approx \text{phys.}. \tag{3.31}$$

Starting at the flavor symmetric point with the lattice H101 (see fig. 3.1), the physical point is approached by decreasing the light quark mass while simultaneously increasing the strange quark mass such that their average is kept constant. Similar approaches of the physical point have already been carried out in the past for hadron masses and form factors [94–96]. An advantage of such strategies is that the QCD interaction is flavor blind and best understood at the flavor symmetric point [94], where the properties of different hadrons can be related by symmetry. For example, in the case of the baryon octet all baryons have the same mass at the symmetric point, which provides an excellent starting point for chiral extrapolations as well as the opportunity to backtest the simulation and analysis code.

3.3.4 Other ensembles

In addition to the CLS ensembles, the analysis runs for the calculation of the distribution amplitudes of the ρ-meson in section 5.2 were performed on ensembles generated on the

QPACE systems as well as within the QCDSF collaboration [97]. A list of the lattices is shown in table 3.2. The gauge configurations employ the Wilson gauge action with $N_f = 2$ flavors of non-perturbatively order a improved Wilson (clover) fermions. The lattices exhibit three different inverse couplings, $\beta = 5.20, 5.29, 5.40$, which correspond to lattice spacings between 0.06 fm and 0.081 fm. Since these ensembles employ periodic boundary conditions, smaller lattice spacings could not be realized and continuum extrapolations for observables sensitive to cutoff effects are difficult to perform. The pion masses vary between 150 MeV and 500 MeV, with spatial volumes between $(1.9\,\mathrm{fm})^3$ and $(4.5\,\mathrm{fm})^3$.

4 Baryon distribution amplitudes

4.1 Overview

Distribution amplitudes are essential for the understanding of hard exclusive processes, i.e., processes that exhibit a momentum-transfer Q^2 which is large with respect to the QCD scale such that

$$Q^2 \gg \Lambda^2_{\mathrm{QCD}}\,. \tag{4.1}$$

They represent reactions in which the concept of the parton picture becomes a valid guiding principle and where perturbative QCD (pQCD) becomes applicable due to the small associated coupling constant $\alpha_s(Q^2)$ [98]. In particular, modern experimental projects like the JLAB@12 GeV upgrade [26, 99] or the future EIC [27] press more and more towards previously unachieved high luminosities. This raises the need for accurate theoretical descriptions of hard exclusive processes in order to deepen our understanding of the structure of hadrons in terms of quark and gluon degrees of freedom. Early research suggested that hard exclusive reactions are dominated by hard gluon exchange contributions [23, 25, 28]. As an example, we consider the scattering process of a nucleon and a highly virtual photon as depicted in figure 4.1. In this case, the Dirac form factor of the nucleon is given by the convolution

$$F_1(Q^2) = \int [dx][dy]\,\Phi^\star(y_i, Q^2) T_H(x_i, y_i, Q^2)\Phi(x_i, Q^2)\,, \tag{4.2}$$

where the integration measure

$$\int [dx] = \int_0^1\!\!\int_0^1\!\!\int_0^1 dx_1 dx_2 dx_3\;\delta(1 - x_1 - x_2 - x_3)\,, \tag{4.3}$$

ensures momentum conservation. Here, $\Phi(x_i)$ denotes the nucleon distribution amplitude, which is the amplitude to find the incoming nucleon in a valence state with each quark carrying the fraction x_i of the nucleon momentum. The hard scattering kernel T_H contains all diagrams for $\gamma^* + 3q \to 3q$, while the DA $\Phi^\star(y_i)$ is the amplitude for the final quark state to form a nucleon again [23]. As already mentioned in the introduction, higher non-valence Fock states of the nucleon are suppressed as the gluonic momentum transfer between the

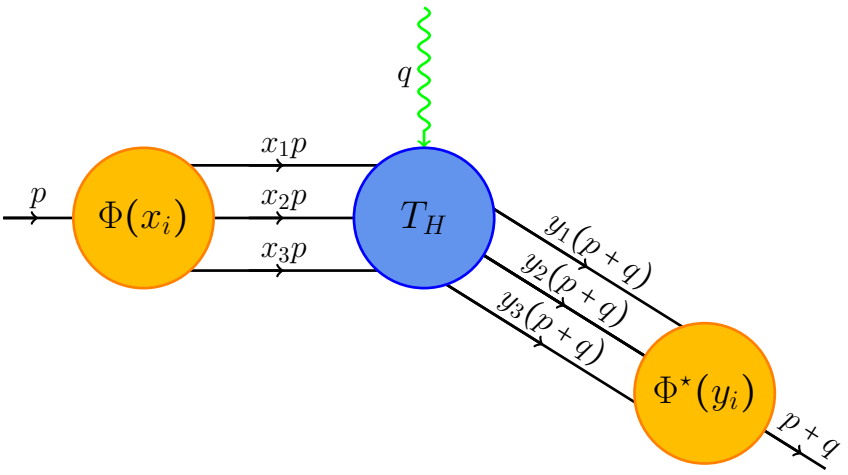

Figure 4.1: The process of absorbing a large transverse momentum while remaining an intact nucleon is described by the form factor $F_1(Q^2)$, which is factorized in terms of the distribution amplitude Φ and the hard scattering kernel T_H, see, e.g., ref [23].

quark lines falls off with a factor of $1/Q^2$ in T_H for each additional constituent.

However, this approach is only valid for very large values of Q^2 as the leading contribution to the baryon form factors contains two hard gluon exchanges, both of which enter the perturbative calculation with a coefficient of α_s/π. The resulting small prefactor $(\alpha_s/\pi)^2 \sim 0.01$ suppresses the pQCD contribution compared to purely soft terms and delays the onset of the perturbative regime. Therefore, although being suppressed by extra powers of $1/Q^2$, soft contributions play a dominant role at moderately large energies [100]. A possible solution of this problem was given in ref. [31], which suggests to calculate the baryon form factors for intermediate values of Q^2 using light-cone sum rules [101, 102]. This approach connects the standard QCD sum rules [103] with the light-cone kinematics of hard exclusive processes [31]. The LCSR method involves the same DAs for the soft contributions as the pQCD calculations and hence provides a direct relation between hadron form factors and distribution amplitudes [100]. For this purpose, one relates the

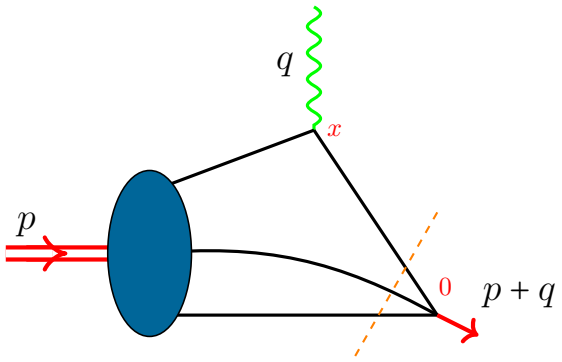

Figure 4.2: Simplified sketch of the LCSR for baryon form factors, cf. ref. [31].

correlation function

$$T_\nu = \int dx^4\, e^{-iqx} \langle 0|T\{\eta(0) j_\nu(x)|N(P)\rangle\,, \tag{4.4}$$

to both, the nucleon form factors and the leading twist nucleon distribution amplitude, which enables a comparison to experimental data [31,100]. In our case, $|N(P)\rangle$ is the state of the nucleon with momentum P, j_ν is an electromagnetic current and η is an operator with the quantum numbers of the nucleon, see figure 4.2 for a simplified representation. LCSR for baryons have also been worked out for the exclusive semileptonic heavy baryon decay $\Lambda_b \to p l \bar{\nu}$ [104] and the $\gamma^* N \to \Delta$ transition form factors [105].

Having successfully established a theoretical connection between nucleon form factors and the nucleon distribution amplitude, the natural next step is a generalization to the whole $J^P = \frac{1}{2}^+$ baryon octet. However, in contrast to the situation for the nucleon [106–110], the available experimental data on hyperon form factors is limited due to their unstable nature. In 1990, the DM2 detector at the Orsay Storage Ring DCI enabled for the first time measurements of the upper limits for the hyperon pair production cross sections $e^+e^- \to \bar{\Lambda}^0\Lambda^0$, $\bar{\Sigma}^0\Sigma^0$, $\bar{\Sigma}^0\Lambda^0$ at $|Q^2| = 5.8\,\text{GeV}^2$ [111]. This was complemented by results of the BaBar detector in 2007 [112], which furthermore produced an estimate for the ratio of the electric and magnetic form factors for $e^+e^- \to \bar{\Lambda}^0\Lambda^0$ as well as measurements of the branching fractions of $J/\psi \to \bar{\Lambda}^0\Lambda^0$, $\bar{\Sigma}^0\Sigma^0$ and $\psi(2S) \to \Lambda^0\bar{\Lambda}^0$. The first direct measurement of the electromagnetic form factors of the $\Lambda^0, \Sigma^0, \Sigma^+, \Xi^0$ and Ξ^- hyperons was conducted by the CLEO-c detector [113] with a time-like momentum transfer of $|Q^2| = 14.2\,\text{GeV}^2$. It was found that the form factors of the different hyperons vary by almost a factor of two. In particular, the form factors of the Λ^0 and Σ^0 hyperons, that share the same valence quark content, fulfill $|G_M(\Lambda^0)| = 1.66\,|G_M(\Sigma^0)|$[1]. In addition to electron-positron annihilations, the exclusive production of hyperons via antiproton-proton collisions, such as $\bar{p}p \to \bar{\Lambda}^0\Lambda^0$ and $\bar{p}p \to \bar{\Xi}^+\Xi^-$ within the $\bar{\text{P}}$anda detector, will also yield further experimental results in the future [114]. A third class of reactions that can be described with hyperon distribution amplitudes is given by rare decays of b-baryons like the $\Lambda_b \to \Lambda^0\mu^+\mu^-$ process, which was measured by both, the CDF [115] and LHCb [116].

The determination of the octet baryon distribution amplitudes provides the foundation for the theoretical description of these processes. In this context, lattice QCD offers the possibility to calculate baryon distribution amplitudes from first principles without additional model input. Previous lattice studies have already investigated the distribution amplitudes of the nucleon by calculating its Mellin moments [44,117,118]. This approach is based on the systematic study of higher twist distribution amplitudes in ref. [119], which contains the first full decomposition of the relevant hadron-to-vacuum matrix element.

[1] The electric and magnetic Sachs form factors G_E and G_M are defined as linear combinations of the Dirac and Pauli form factors, cf. [31].

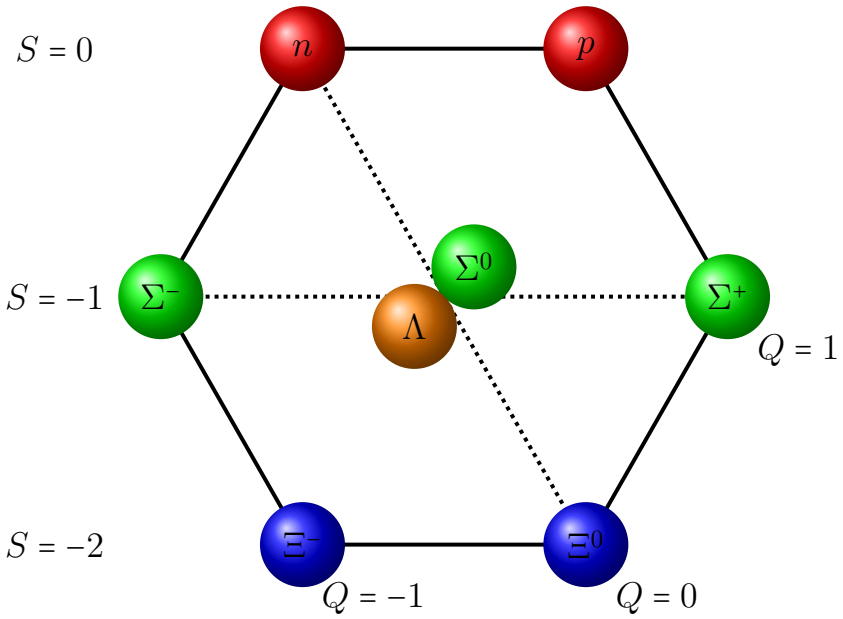

Figure 4.3: Visualization of the $J^P = \frac{1}{2}^+$ baryon octet.

In this chapter we will present results of the first lattice study on distribution amplitudes of the $J^P = \frac{1}{2}^+$ baryon octet, which has been published in ref. [24]. The determination of the octet DAs requires multidisciplinary expertise from various subfields of QCD. Beyond lattice QCD itself, the list includes the renormalization of composite operators and chiral perturbation theory. This project was carried out as a joint effort, where the renormalization was treated by M. Gruber [120], while the chiral extrapolation was provided by P. Wein [121]. The present work is mainly concerned with the lattice aspects of the calculation.

4.2 Continuum formulation

The $J^P = \frac{1}{2}^+$ baryon octet is shown in figure 4.3 and contains eight particles organized into two isodoublets, (p, n) and (Ξ^0, Ξ^-), one isotriplet $(\Sigma^+, \Sigma^0, \Sigma^-)$ and one isosinglet (Λ). By assuming exact isospin symmetry ($m_l \equiv m_u = m_d$) and neglecting electromagnetic effects, one only has to consider one member of each isospin multiplet. Hence, we choose our baryons B such that

$$B \in \{N \equiv p, \Sigma \equiv \Sigma^-, \Xi \equiv \Xi^0, \Lambda\}\,. \tag{4.5}$$

Baryon distribution amplitudes are defined in terms of baryon-to-vacuum matrix elements

of renormalized three-quark operators at light-like separations [119]:

$$B^{fgh}_{\alpha\beta\gamma}(a_1, a_2, a_3; \mu) = \langle 0 | f_\alpha(a_1 n) g_\beta(a_2 n) h_\gamma(a_3 n) | B(p, \lambda) \rangle \,, \tag{4.6}$$

where $|B(p,\lambda)\rangle$ is the baryon state with momentum p and helicity λ, while α, β, γ are Dirac indices, n is a light-cone vector ($n^2 = 0$), the a_i are real numbers and f, g, h are quark fields of the given flavor, chosen to match the valence quark content of the baryon B. In order to sustain gauge invariance, the quark fields in eq. (4.6) are connected by Wilson lines which we omit to write out explicitly.

We choose the following flavor ordering:

$$p: \quad (f,g,h) = (u,u,d)\,, \tag{4.7a}$$
$$\Sigma^-: \quad (f,g,h) = (d,d,s)\,, \tag{4.7b}$$
$$\Xi^0: \quad (f,g,h) = (s,s,u)\,, \tag{4.7c}$$
$$\Lambda: \quad (f,g,h) = (u,d,s)\,. \tag{4.7d}$$

The general Lorentz decomposition of the matrix element (4.6) consists of 24 terms [119] such that

$$B_{\alpha\beta\gamma}(a_1, a_2, a_3; \mu) = \sum_{\mathrm{DA}} \left(\Gamma^{\mathrm{DA}}\right)_{\alpha\beta} \left(\tilde{\Gamma}^{\mathrm{DA}} u^B(p,\lambda)\right)_\gamma \int [dx]\, e^{-ip\cdot n \sum_i a_i x_i}\, \mathrm{DA}^B(x_1, x_2, x_3; \mu)\,. \tag{4.8}$$

The Dirac structures Γ^{DA} and $\tilde{\Gamma}^{\mathrm{DA}}$ correspond to the distribution amplitude $\mathrm{DA}^B(x_i)$, see eq. (2.9) of ref. [119], and $u^B(p,\lambda)$ is the Dirac spinor with on-shell momentum p ($p^2 = m_B^2$) and helicity λ. This decomposition can be organized in such a way that all DAs have definite collinear twist. The variables x_1, x_2, x_3 correspond to the momentum fractions carried by the quarks f, g, h, respectively.

4.2.1 Leading twist distribution amplitudes

With respect to the leading twist contributions, the general decomposition in eq. (4.8) yields [25]:

$$\begin{aligned} 4B_{\alpha\beta\gamma}(a_1, a_2, a_3) = &\int [dx]\, e^{-ip\cdot n \sum_i a_i x_i} \\ &\times \left(v^B_{\alpha\beta;\gamma} V^B(x_1,x_2,x_3) + a^B_{\alpha\beta;\gamma} A^B(x_1,x_2,x_3) + t^B_{\alpha\beta;\gamma} T^B(x_1,x_2,x_3) + \ldots \right), \end{aligned} \tag{4.9}$$

with the leading twist Dirac structures

$$v^B_{\alpha\beta;\gamma} = (\tilde{\not{n}}C)_{\alpha\beta}(\gamma_5 u^B_+(p,\lambda))_\gamma\,, \tag{4.10a}$$
$$a^B_{\alpha\beta;\gamma} = (\tilde{\not{n}}\gamma_5 C)_{\alpha\beta}(u^B_+(p,\lambda))_\gamma\,, \tag{4.10b}$$
$$t^B_{\alpha\beta;\gamma} = (i\sigma_{\perp\tilde{n}}C)_{\alpha\beta}(\gamma^\perp\gamma_5 u^B_+(p,\lambda))_\gamma\,, \tag{4.10c}$$

where C denotes the charge conjugation matrix and

$$\tilde{n}_\mu = p_\mu - \frac{1}{2}\frac{p^2}{p\cdot n}n_\mu\,, \qquad u^B_+(p,\lambda) = \frac{1}{2}\frac{\tilde{\not{n}}\not{n}}{\tilde{n}\,\cdot\, n}u^B(p,\lambda)\,, \tag{4.11a}$$
$$\sigma_{\perp\tilde{n}}\otimes\gamma^\perp = \sigma^{\mu\rho}\tilde{n}_\rho g^\perp_{\mu\nu}\otimes\gamma^\nu\,, \qquad g^\perp_{\mu\nu} = g_{\mu\nu} - \frac{\tilde{n}_\mu n_\nu + \tilde{n}_\nu n_\mu}{\tilde{n}\cdot n}\,. \tag{4.11b}$$

By inserting suitable Dirac structures into the baryon-to-vacuum matrix element, the individual DAs appearing in eq. (4.8) can be isolated. For the leading twist contributions one obtains:

$$\begin{aligned}&\langle 0|\big(f^{\uparrow T}(a_1 n)C\not{n}g^\downarrow(a_2 n)\big)\not{n}h^\uparrow(a_3 n)|B(p,\lambda)\rangle\\ &\qquad = -\tfrac{1}{2}(p\cdot n)\not{n}u^{B\uparrow}(p,\lambda)\int[dx]\,e^{-ipn\sum_i a_i x_i}\,[V-A]^B(x_1,x_2,x_3)\,,\end{aligned} \tag{4.12a}$$
$$\begin{aligned}&\langle 0|\big(f^{\uparrow T}(a_1 n)C\gamma^\mu\not{n}g^\uparrow(a_2 n)\big)\gamma_\mu\not{n}h^\downarrow(a_3 n)|B(p,\lambda)\rangle\\ &\qquad = 2(p\cdot n)\not{n}u^{B\uparrow}(p,\lambda)\int[dx]\,e^{-ipn\sum_i a_i x_i}\,T^B(x_1,x_2,x_3)\,.\end{aligned} \tag{4.12b}$$

Here we use the definition in terms of the right- and left-handed components of the quark fields where $q^{\uparrow(\downarrow)} = \frac{1}{2}(\mathbb{1}\pm\gamma_5)q$ and $u^{B\uparrow}(p,\lambda) = \frac{1}{2}(\mathbb{1}+\gamma_5)u^B(p,\lambda)$. Eqs. (4.12) also yield that $[V-A]^B$ corresponds to the helicity order $|\uparrow\downarrow\uparrow\rangle$, while T^B corresponds to $|\uparrow\uparrow\downarrow\rangle$. The three leading twist DAs have the following symmetry properties under the exchange of the first and second quark:

$$V^{B\neq\Lambda}(x_2,x_1,x_3) = +V^B(x_1,x_2,x_3)\,, \qquad V^\Lambda(x_2,x_1,x_3) = -V^\Lambda(x_1,x_2,x_3)\,, \tag{4.13a}$$
$$A^{B\neq\Lambda}(x_2,x_1,x_3) = -A^B(x_1,x_2,x_3)\,, \qquad A^\Lambda(x_2,x_1,x_3) = +A^\Lambda(x_1,x_2,x_3)\,, \tag{4.13b}$$
$$T^{B\neq\Lambda}(x_2,x_1,x_3) = +T^B(x_1,x_2,x_3)\,, \qquad T^\Lambda(x_2,x_1,x_3) = -T^\Lambda(x_1,x_2,x_3)\,. \tag{4.13c}$$

Furthermore, due to isospin symmetry it yields that

$$2T^N(x_1,x_3,x_2) = [V-A]^N(x_1,x_2,x_3) + [V-A]^N(x_3,x_2,x_1)\,, \tag{4.14}$$

which means that the nucleon has only one independent leading twist DA defined as

$$\Phi^N(x_1,x_2,x_3) = [V-A]^N(x_1,x_2,x_3)\,. \tag{4.15}$$

The standard DAs V^N and A^N can be recovered from Φ^N by using eqs. (4.13). We generalize eq. (4.15) for the full octet and define

$$\Phi^{B\neq\Lambda}(x_1,x_2,x_3) = [V-A]^B(x_1,x_2,x_3)\,, \tag{4.16a}$$

$$\Phi^{\Lambda}(x_1,x_2,x_3) = -\sqrt{\tfrac{2}{3}}\big\{[V-A]^{\Lambda}(x_1,x_2,x_3) - 2[V-A]^{\Lambda}(x_3,x_2,x_1)\big\}\,. \tag{4.16b}$$

Eq. (4.14) does not hold for the remaining baryons $B \neq N$ and the functions $T^{B\neq N}$ are independent of $[V-A]^{B\neq N}$. Hence, in order to examine the SU(3) symmetry breaking behavior it is advantageous to define the following set of DAs [121]:

$$\Phi_{\pm}^{B\neq\Lambda}(x_1,x_2,x_3) = \tfrac{1}{2}\big\{[V-A]^B(x_1,x_2,x_3) \pm [V-A]^B(x_3,x_2,x_1)\big\}\,, \tag{4.17a}$$

$$\Pi^{B\neq\Lambda}(x_1,x_2,x_3) = T^B(x_1,x_3,x_2)\,, \tag{4.17b}$$

$$\Phi_{+}^{\Lambda}(x_1,x_2,x_3) = \sqrt{\tfrac{1}{6}}\big\{[V-A]^{\Lambda}(x_1,x_2,x_3) + [V-A]^{\Lambda}(x_3,x_2,x_1)\big\}\,, \tag{4.17c}$$

$$\Phi_{-}^{\Lambda}(x_1,x_2,x_3) = -\sqrt{\tfrac{3}{2}}\big\{[V-A]^{\Lambda}(x_1,x_2,x_3) - [V-A]^{\Lambda}(x_3,x_2,x_1)\big\}\,, \tag{4.17d}$$

$$\Pi^{\Lambda}(x_1,x_2,x_3) = \sqrt{6}\,T^{\Lambda}(x_1,x_3,x_2)\,, \tag{4.17e}$$

where for the nucleon $\Pi^N = \Phi_+^N$ up to isospin breaking effects. In the limit of SU(3) flavor symmetry, where $m_u = m_d = m_s$ (and in particular at the flavor symmetric point with physical average quark mass indicated by $\star$), the following relations hold:

$$\Phi_{+}^{\star} \equiv \Phi_{+}^{N\star} = \Phi_{+}^{\Sigma\star} = \Phi_{+}^{\Xi\star} = \Phi_{+}^{\Lambda\star} = \Pi^{N\star} = \Pi^{\Sigma\star} = \Pi^{\Xi\star}\,, \tag{4.18a}$$

$$\Phi_{-}^{\star} \equiv \Phi_{-}^{N\star} = \Phi_{-}^{\Sigma\star} = \Phi_{-}^{\Xi\star} = \Phi_{-}^{\Lambda\star} = \Pi^{\Lambda\star}\,. \tag{4.18b}$$

Therefore, the amplitudes Π^B (or T^B) are only independent DAs when flavor symmetry is broken. We expand the DAs in a set of orthogonal polynomials, $\mathcal{P}_{nk}(x_1,x_2,x_3)$, which correspond to irreducible representations of the collinear conformal group $\mathrm{SL}(2,\mathbb{R})$. The first few polynomials are [122]:

$$\mathcal{P}_{00} = 1\,, \qquad \mathcal{P}_{20} = \tfrac{63}{10}[3(x_1-x_3)^2 - 3x_2(x_1+x_3) + 2x_2^2]\,, \tag{4.19a}$$

$$\mathcal{P}_{10} = 21(x_1-x_3)\,, \qquad \mathcal{P}_{21} = \tfrac{63}{2}(x_1-3x_2+x_3)(x_1-x_3)\,, \tag{4.19b}$$

$$\mathcal{P}_{11} = 7(x_1-2x_2+x_3)\,, \qquad \mathcal{P}_{22} = \tfrac{9}{5}[x_1^2 + 9x_2(x_1+x_3) - 12x_1x_3 - 6x_2^2 + x_3^2]\,. \tag{4.19c}$$

The DAs Φ_+^B and $\Pi^{B\neq\Lambda}$ (Φ_-^B and Π^Λ) are constructed such that they contain only polynomials that are symmetric (antisymmetric) under the exchange of x_1 and x_3:

$$\Phi_+^B = 120x_1x_2x_3\big(\varphi_{00}^B\mathcal{P}_{00} + \varphi_{11}^B\mathcal{P}_{11} + \varphi_{20}^B\mathcal{P}_{20} + \varphi_{22}^B\mathcal{P}_{22} + \dots\big)\,, \tag{4.20a}$$

$$\Phi_-^B = 120x_1x_2x_3\big(\varphi_{10}^B\mathcal{P}_{10} + \varphi_{21}^B\mathcal{P}_{21} + \dots\big)\,, \tag{4.20b}$$

$$\Pi^{B\neq\Lambda} = 120x_1x_2x_3\big(\pi_{00}^B\mathcal{P}_{00} + \pi_{11}^B\mathcal{P}_{11} + \pi_{20}^B\mathcal{P}_{20} + \pi_{22}^B\mathcal{P}_{22} + \dots\big)\,, \tag{4.20c}$$

$$\Pi^\Lambda = 120x_1x_2x_3\big(\pi_{10}^\Lambda\mathcal{P}_{10} + \pi_{21}^\Lambda\mathcal{P}_{21} + \dots\big)\,. \tag{4.20d}$$

The whole non-perturbative information is in this way encoded in the set of the coefficients φ_{nk}^B, π_{nk}^B, which can be related to matrix elements of local operators. The leading contributions $120x_1x_2x_3\varphi_{00}^B$ and $120x_1x_2x_3\pi_{00}^{B\neq\Lambda}$ are usually referred to as the asymptotic DAs. The corresponding normalization coefficients φ_{00}^B and $\pi_{00}^{B\neq\Lambda}$ can be thought of as the wave functions at the origin. In the following we will use the notation

$$f^B = \varphi_{00}^B\,, \qquad\qquad f_T^{B\neq\Lambda} = \pi_{00}^B\,. \tag{4.21}$$

Note that for the nucleon the two coupling constants coincide, $f_T^N = f^N$. For the Λ baryon the zeroth moment of T^Λ vanishes. The higher-order coefficients are usually referred to as shape parameters.

The interpretation of the DAs V^B, A^B and T^B as well as Φ_+^B, Φ_-^B and Π^B can be mapped out by considering their relation to light-front wave functions. The leading twist approximation contains all S-wave contributions in which the helicities of the quarks sum up to the helicity of the baryon [123, 124]. The standard DAs V^B, A^B and T^B appear naturally when one describes a flavor-ordered wave function:

$$\begin{aligned}|(B\neq\Lambda)^\uparrow\rangle = \int\frac{[dx]}{8\sqrt{6x_1x_2x_3}}|fgh\rangle\otimes\big\{&[V+A]^B(x_1,x_2,x_3)|{\downarrow}{\uparrow}{\uparrow}\rangle\\ &+[V-A]^B(x_1,x_2,x_3)|{\uparrow}{\downarrow}{\uparrow}\rangle\\ &-2T^B(x_1,x_2,x_3)|{\uparrow}{\uparrow}{\downarrow}\rangle\big\}\,,\end{aligned} \tag{4.22a}$$

$$\begin{aligned}|\Lambda^\uparrow\rangle = \int\frac{[dx]}{4\sqrt{6x_1x_2x_3}}|uds\rangle\otimes\big\{&[V+A]^\Lambda(x_1,x_2,x_3)|{\downarrow}{\uparrow}{\uparrow}\rangle\\ &+[V-A]^\Lambda(x_1,x_2,x_3)|{\uparrow}{\downarrow}{\uparrow}\rangle\\ &-2T^\Lambda(x_1,x_2,x_3)|{\uparrow}{\uparrow}{\downarrow}\rangle\big\}\,,\end{aligned} \tag{4.22b}$$

where $|{\uparrow}{\downarrow}{\uparrow}\rangle$ etc. show quark helicities and $|fgh\rangle$ stands for the flavor ordering as specified in eqs. (4.7). In contrast, the DAs Φ_+^B, Φ_-^B and Π^B appear together with their corresponding

flavor structure in a helicity-ordered wave function:

$$|(B{\neq}\Lambda)^{\uparrow}\rangle = \int \frac{[dx]}{8\sqrt{3x_1x_2x_3}} |\uparrow\uparrow\downarrow\rangle \otimes \big\{-\sqrt{3}\Phi_+^B(x_1,x_3,x_2)\big(|\mathrm{MS},B\rangle - \sqrt{2}|\mathrm{S},B\rangle\big)/3 \\ -\sqrt{3}\Pi^B(x_1,x_3,x_2)\big(2|\mathrm{MS},B\rangle + \sqrt{2}|\mathrm{S},B\rangle\big)/3 \\ +\Phi_-^B(x_1,x_3,x_2)|\mathrm{MA},B\rangle\big\}\,, \tag{4.23a}$$

$$|\Lambda^{\uparrow}\rangle = \int \frac{[dx]}{8\sqrt{3x_1x_2x_3}} |\uparrow\uparrow\downarrow\rangle \otimes \big\{-\sqrt{3}\Phi_+^\Lambda(x_1,x_3,x_2)|\mathrm{MS},\Lambda\rangle \\ +\Pi^\Lambda(x_1,x_3,x_2)\big(2|\mathrm{MA},\Lambda\rangle + \sqrt{2}|\mathrm{A},\Lambda\rangle\big)/3 \\ +\Phi_-^\Lambda(x_1,x_3,x_2)\big(|\mathrm{MA},\Lambda\rangle - \sqrt{2}|\mathrm{A},\Lambda\rangle\big)/3\big\}\,, \tag{4.23b}$$

where $|\mathrm{MS},B\rangle$ and $|\mathrm{MA},B\rangle$ are the mixed-symmetric and mixed-antisymmetric octet flavor wave functions, while $|\mathrm{A},\Lambda\rangle$ and $|\mathrm{S},B\neq\Lambda\rangle$ are the totally antisymmetric and symmetric flavor wave functions as defined in appendix A of [24].

4.2.2 Higher twist contributions

In general, higher twist contributions stem from three different sources: Contributions of higher Fock states with additional gluons and/or quark-antiquark pairs, contributions of transverse motion of quarks in the leading twist components and contributions from so-called bad[2] components in the wave function, cf. [119, 127].

In our case, the general decomposition in eq. (4.8) contains 21 DAs of higher twist. They include only up to three new normalization constants (just two for N, Σ and Ξ) [119, 121], which can be defined as matrix elements of local three-quark twist four operators without derivatives. These twist four couplings are also interesting in a broader context, e.g., in studies of baryon decays in generic GUT models [128], and as input parameters for QCD sum rule calculations, see, e.g., refs. [129–131].

We use the following definitions:

$$\langle 0|\big(f^{\uparrow T}(0)C\gamma^\mu g^{\downarrow}(0)\big)\gamma_\mu h^{\uparrow}(0)|(B\neq\Lambda)(p,\lambda)\rangle = -\tfrac{1}{2}\lambda_1^B m_B u^{B\downarrow}(p,\lambda)\,, \tag{4.24a}$$

$$\langle 0|\big(f^{\uparrow T}(0)C\sigma^{\mu\nu} g^{\uparrow}(0)\big)\sigma_{\mu\nu} h^{\uparrow}(0)|(B\neq\Lambda)(p,\lambda)\rangle = \lambda_2^B m_B u^{B\uparrow}(p,\lambda)\,, \tag{4.24b}$$

for the isospin-nonsinglet baryons (N, Σ, Ξ) and

$$\langle 0|\big(u^{\uparrow T}(0)C\gamma^\mu d^{\downarrow}(0)\big)\gamma_\mu s^{\uparrow}(0)|\Lambda(p,\lambda)\rangle = \tfrac{1}{2\sqrt{6}}\lambda_1^\Lambda m_\Lambda u^{\Lambda\downarrow}(p,\lambda)\,, \tag{4.25a}$$

$$\langle 0|\big(u^{\uparrow T}(0)Cd^{\uparrow}(0)\big)s^{\downarrow}(0)|\Lambda(p,\lambda)\rangle = \tfrac{1}{2\sqrt{6}}\lambda_T^\Lambda m_\Lambda u^{\Lambda\downarrow}(p,\lambda)\,, \tag{4.25b}$$

$$\langle 0|\big(u^{\uparrow T}(0)Cd^{\uparrow}(0)\big)s^{\uparrow}(0)|\Lambda(p,\lambda)\rangle = \tfrac{-1}{4\sqrt{6}}\lambda_2^\Lambda m_\Lambda u^{\Lambda\uparrow}(p,\lambda)\,, \tag{4.25c}$$

[2] This terminology is to be understood in terms of the light-cone formalism of Kogut and Soper, which separates the quark field into "good" and "bad" components, cf. [125, 126]

for the Λ baryon. As defined in [121], all twist four couplings coincide at the flavor symmetric point such that

$$\lambda_1^\star \equiv \lambda_1^{N\star} = \lambda_1^{\Sigma\star} = \lambda_1^{\Xi\star} = \lambda_1^{\Lambda\star} = \lambda_T^{\Lambda\star}\,, \tag{4.26a}$$

$$\lambda_2^\star \equiv \lambda_2^{N\star} = \lambda_2^{\Sigma\star} = \lambda_2^{\Xi\star} = \lambda_2^{\Lambda\star}\,. \tag{4.26b}$$

4.3 Lattice formulation

In the following we will show how baryon DAs can be accessed on a lattice. For this purpose, we follow the Euclidean gamma matrix convention of [117]. Distribution amplitudes cannot be calculated directly on the lattice, as this would require quark fields at light-like separations. Instead one calculates moments of the DAs like

$$V^B_{lmn} = \int [dx]\; x_1^l x_2^m x_3^n V^B(x_1,x_2,x_3)\,, \tag{4.27}$$

and similarly for the other functions. In order to extract the desired moments of the DAs on the lattice one calculates two-point correlation functions of the general form

$$\langle 0|\mathcal{X}(t,\mathbf{p})\bar{\mathcal{N}}^B(0,\mathbf{p})|0\rangle\,. \tag{4.28}$$

The smeared source operator $\mathcal{N}^B$ is an interpolating creation operator which is chosen such that it has a good overlap with the baryon of interest, see, e.g., [132] for spin-1/2 baryons. Our choice of interpolating currents is as follows:

$$\mathcal{N}^N = \big(u^T C\gamma_5 d\big)u\,, \tag{4.29a}$$

$$\mathcal{N}^\Sigma = \big(d^T C\gamma_5 s\big)d\,, \tag{4.29b}$$

$$\mathcal{N}^\Xi = \big(s^T C\gamma_5 u\big)s\,, \tag{4.29c}$$

$$\mathcal{N}^\Lambda = \tfrac{1}{\sqrt{6}}\big(2\big(u^T C\gamma_5 d\big)s + \big(u^T C\gamma_5 s\big)d + \big(s^T C\gamma_5 d\big)u\big)\,, \tag{4.29d}$$

where each operator is smeared to suppress excited state contributions. The optimal number of smearing steps was determined before the actual analysis runs by gradually applying more and more smearing steps to the light and strange quark propagators while simultaneously tracking the ground state behavior and noise of the standard pion and kaon correlation functions.

The sink operator $\mathcal{X}$ is a local (unsmeared) three-quark operator of the form

$$\mathcal{X}^{B,lmn}_{\bar{r}\bar{l}\bar{m}\bar{n}} = \epsilon^{ijk}\Big(\big[i^l D_{\bar{l}} f^T(0)\big]^i C\Gamma^{\mathcal{X}_{\bar{r}}}_{\bar{r}}\big[i^m D_{\bar{m}} g(0)\big]^j\Big)\tilde{\Gamma}^{\mathcal{X}_{\bar{r}}}\big[i^n D_{\bar{n}} h(0)\big]^k\,. \tag{4.30}$$

Here we use a multi-index notation for the covariant derivatives, $D_{\bar{l}} \equiv D_{\lambda_1}\cdots D_{\lambda_l}$. The Dirac

$\mathcal{X}_{\bar{r}}$	$\mathcal{S}$	$\mathcal{P}$	$\mathcal{V}$	$\mathcal{A}$	$\mathcal{T}$	$\mathcal{V}_\rho$	$\mathcal{A}_\rho$	$\mathcal{T}_\rho$
$\Gamma_{\bar{r}}^{\mathcal{X}_{\bar{r}}}$	$\mathbb{1}$	γ_5	γ_η	$\gamma_\eta\gamma_5$	$\sigma_{\eta_1\eta_2}$	γ_ρ	$\gamma_\rho\gamma_5$	$i\sigma_{\rho\eta}$
$\tilde{\Gamma}^{\mathcal{X}_{\bar{r}}}$	γ_5	$\mathbb{1}$	$\gamma_\eta\gamma_5$	γ_η	$\sigma_{\eta_1\eta_2}\gamma_5$	γ_5	$\mathbb{1}$	$\gamma_\eta\gamma_5$

Table 4.1: Definition of the Dirac matrix structures that appear in the local operators which are used in the lattice calculation, see eq. (4.30). Lorentz indices appearing in both $\Gamma_{\bar{r}}^{\mathcal{X}_{\bar{r}}}$ and $\tilde{\Gamma}^{\mathcal{X}_{\bar{r}}}$ are summed over implicitly.

structures, $\Gamma_{\bar{r}}^{\mathcal{X}_{\bar{r}}}$ and $\tilde{\Gamma}^{\mathcal{X}_{\bar{r}}}$, which isolate the respective moments, are listed in table 4.1. Neglecting the exponentially suppressed excited states, the correlation functions can be written as

$$\langle \mathcal{O}_\tau(t,\mathbf{p})\bar{\mathcal{N}}^B_{\tau'}(0,\mathbf{p})\rangle = \frac{\sqrt{Z_B}}{2E_B}\sum_\lambda \langle 0|\mathcal{O}_\tau(0)|B(\mathbf{p},\lambda)\rangle\ \bar{u}^B_{\tau'}(\mathbf{p},\lambda)e^{-E_B t}\,, \tag{4.31}$$

with the energy $E_B = E_B(\mathbf{p}) = \sqrt{m_B^2+\mathbf{p}^2}$. The coupling $Z_B = Z_B(\mathbf{p})$ is momentum-dependent and describes the overlap between the smeared source operator and the physical baryon ground state. It can be obtained from the correlator

$$\langle \mathcal{N}^B_\tau(t,\mathbf{p})\bar{\mathcal{N}}^B_{\tau'}(0,\mathbf{p})(\gamma_+)_{\tau'\tau}\rangle = Z_B\frac{m_B+kE_B}{E_B}e^{-E_B t}\,, \tag{4.32}$$

where $\gamma_+ = (\mathbb{1}+k\gamma_4)/2$ with $k = m_{B^*}/E_{B^*}$ acts effectively as a parity "projector"[3] to suppress contributions from the negative parity partner B^* of the baryon B [44, 132].

4.3.1 Correlation functions

The simplest application of eq. (4.31) is the calculation of the leading twist normalization constants f^B and f_T^B, as in these cases no derivatives are needed within $\mathcal{X}$. In order to avoid higher twist contributions we construct the following linear combinations of operators:

$$\mathcal{O}^{B,000}_{\mathcal{X},\mathfrak{A}} = -\gamma_1\mathcal{X}_1^{B,000} + \gamma_2\mathcal{X}_2^{B,000}\,, \tag{4.33a}$$

$$\mathcal{O}^{B,000}_{\mathcal{X},\mathfrak{B}} = -\gamma_3\mathcal{X}_3^{B,000} + \gamma_4\mathcal{X}_4^{B,000}\,, \tag{4.33b}$$

$$\mathcal{O}^{B,000}_{\mathcal{X},\mathfrak{C}} = -\gamma_1\mathcal{X}_1^{B,000} - \gamma_2\mathcal{X}_2^{B,000} + \gamma_3\mathcal{X}_3^{B,000} + \gamma_4\mathcal{X}_4^{B,000}\,, \tag{4.33c}$$

[3] Strictly speaking, γ_+ is not a real projector for $k \neq 1$ as $\gamma_+^2 \neq \gamma_+$.

where $\mathcal{X}$ can be $\mathcal{V}$, $\mathcal{A}$ or $\mathcal{T}$. From these one obtains the following correlation functions:

$$\begin{aligned} C^{B,000}_{\mathcal{X},\mathfrak{A}} &= \langle \big(\gamma_4 \mathcal{O}^{B,000}_{\mathcal{X},\mathfrak{A}}(t,\mathbf{p})\big)_\tau \bar{\mathcal{N}}^B_{\tau'}(0,\mathbf{p})(\gamma_+)_{\tau'\tau}\rangle \\ &= c_X X^B_{000}\sqrt{Z_B}\frac{k(p_1^2-p_2^2)}{E_B}e^{-E_B t}\,, \end{aligned} \tag{4.34a}$$

$$\begin{aligned} C^{B,000}_{\mathcal{X},\mathfrak{B}} &= \langle \big(\gamma_4 \mathcal{O}^{B,000}_{\mathcal{X},\mathfrak{B}}(t,\mathbf{p})\big)_\tau \bar{\mathcal{N}}^B_{\tau'}(0,\mathbf{p})(\gamma_+)_{\tau'\tau}\rangle \\ &= c_X X^B_{000}\sqrt{Z_B}\frac{E_B(m_B+kE_B)+kp_3^2}{E_B}e^{-E_B t}\,, \end{aligned} \tag{4.34b}$$

$$\begin{aligned} C^{B,000}_{\mathcal{X},\mathfrak{C}} &= \langle \big(\gamma_4 \mathcal{O}^{B,000}_{\mathcal{X},\mathfrak{C}}(t,\mathbf{p})\big)_\tau \bar{\mathcal{N}}^B_{\tau'}(0,\mathbf{p})(\gamma_+)_{\tau'\tau}\rangle \\ &= c_X X^B_{000}\sqrt{Z_B}\frac{E_B(m_B+kE_B)+k(p_1^2+p_2^2-p_3^2)}{E_B}e^{-E_B t}\,, \end{aligned} \tag{4.34c}$$

where $c_V = c_A = 1$ and $c_T = -2$. Again, $\mathcal{X}$ can be $\mathcal{V}$, $\mathcal{A}$ or $\mathcal{T}$. A close look at the right-hand side of eqs. (4.34) shows that it is possible to extract the zeroth moment X^B_{000} from the correlators $C^{B,000}_{\mathcal{X},\mathfrak{B}}$ and $C^{B,000}_{\mathcal{X},\mathfrak{C}}$ using $\mathbf{p} = \mathbf{0}$, as in this case terms proportional to $m_B = E_B(\mathbf{p} = \mathbf{0})$ do not vanish. In contrast, the correlator $C^{B,000}_{\mathcal{X},\mathfrak{A}}$ only contains terms proportional to either p_1^2 or p_2^2 and hence vanishes for zero momentum. It is therefore preferable to use $C^{B,000}_{\mathcal{X},\mathfrak{B}}$ and $C^{B,000}_{\mathcal{X},\mathfrak{C}}$ as they are less noisy and, therefore, can be measured with higher accuracy. From the zeroth moments X^B_{000}, one obtains the desired coupling in the following way:

$$f^{B\neq\Lambda} \equiv \varphi^B_{00} = V^B_{000}\,, \qquad f^\Lambda \equiv \varphi^\Lambda_{00} = -\sqrt{\tfrac{2}{3}}A^\Lambda_{000}\,, \qquad f_T^{B\neq\Lambda} \equiv \pi^B_{00} = T^B_{000}\,, \tag{4.35}$$

where $f_T^N = f^N$ due to isospin symmetry. The remaining zeroth moments of the leading twist DAs V^B, A^B and T^B vanish:

$$V^\Lambda_{000} = A^{B\neq\Lambda}_{000} = T^\Lambda_{000} = 0\,. \tag{4.36}$$

The situation for the first moments of the DAs is more involved as the sink operators now contain covariant derivatives. For $l+m+n=1$ we define the leading twist combinations

$$\mathcal{O}^{B,lmn}_{\mathcal{X},\mathfrak{A}} = +\gamma_1\gamma_3\mathcal{X}^{B,lmn}_{\{13\}} + \gamma_1\gamma_4\mathcal{X}^{B,lmn}_{\{14\}} - \gamma_2\gamma_3\mathcal{X}^{B,lmn}_{\{23\}} - \gamma_2\gamma_4\mathcal{X}^{B,lmn}_{\{24\}} - 2\gamma_1\gamma_2\mathcal{X}^{B,lmn}_{\{12\}}\,, \tag{4.37a}$$

$$\mathcal{O}^{B,lmn}_{\mathcal{X},\mathfrak{B}} = +\gamma_1\gamma_3\mathcal{X}^{B,lmn}_{\{13\}} - \gamma_1\gamma_4\mathcal{X}^{B,lmn}_{\{14\}} + \gamma_2\gamma_3\mathcal{X}^{B,lmn}_{\{23\}} - \gamma_2\gamma_4\mathcal{X}^{B,lmn}_{\{24\}} + 2\gamma_3\gamma_4\mathcal{X}^{B,lmn}_{\{34\}}\,, \tag{4.37b}$$

$$\mathcal{O}^{B,lmn}_{\mathcal{X},\mathfrak{C}} = -\gamma_1\gamma_3\mathcal{X}^{B,lmn}_{\{13\}} + \gamma_1\gamma_4\mathcal{X}^{B,lmn}_{\{14\}} + \gamma_2\gamma_3\mathcal{X}^{B,lmn}_{\{23\}} - \gamma_2\gamma_4\mathcal{X}^{B,lmn}_{\{24\}}\,, \tag{4.37c}$$

where the braces indicate symmetrization. For the calculation of the first moments of the leading twist DAs one can use the correlation functions ($l+m+n=1$)

$$
\begin{aligned}
C^{B,lmn}_{\mathcal{X},\mathfrak{A},1} &= \langle \big(\gamma_4\gamma_1 \mathcal{O}^{B,lmn}_{\mathcal{X},\mathfrak{A}}(t,\mathbf{p})\big)_\tau \bar{\mathcal{N}}^B_{\tau'}(0,\mathbf{p})(\gamma_+)_{\tau'\tau}\rangle \\
&= -c_X X^B_{lmn}\sqrt{Z_B}p_1 \frac{E_B(m_B+kE_B)+k(2p_2^2-p_3^2)}{E_B} e^{-E_B t}\,, \qquad (4.38a)\\
C^{B,lmn}_{\mathcal{X},\mathfrak{A},2} &= \langle \big(\gamma_4\gamma_2 \mathcal{O}^{B,lmn}_{\mathcal{X},\mathfrak{A}}(t,\mathbf{p})\big)_\tau \bar{\mathcal{N}}^B_{\tau'}(0,\mathbf{p})(\gamma_+)_{\tau'\tau}\rangle \\
&= +c_X X^B_{lmn}\sqrt{Z_B}p_2 \frac{E_B(m_B+kE_B)+k(2p_1^2-p_3^2)}{E_B} e^{-E_B t}\,, \qquad (4.38b)\\
C^{B,lmn}_{\mathcal{X},\mathfrak{A},3} &= \langle \big(\gamma_4\gamma_3 \mathcal{O}^{B,lmn}_{\mathcal{X},\mathfrak{A}}(t,\mathbf{p})\big)_\tau \bar{\mathcal{N}}^B_{\tau'}(0,\mathbf{p})(\gamma_+)_{\tau'\tau}\rangle \\
&= -c_X X^B_{lmn}\sqrt{Z_B}p_3 \frac{k(p_1^2-p_2^2)}{E_B} e^{-E_B t}\,, \qquad (4.38c)
\end{aligned}
$$

$$
\begin{aligned}
C^{B,lmn}_{\mathcal{X},\mathfrak{B},1} &= \langle \big(\gamma_4\gamma_1 \mathcal{O}^{B,lmn}_{\mathcal{X},\mathfrak{B}}(t,\mathbf{p})\big)_\tau \bar{\mathcal{N}}^B_{\tau'}(0,\mathbf{p})(\gamma_+)_{\tau'\tau}\rangle \\
&= +c_X X^B_{lmn}\sqrt{Z_B}p_1 \frac{E_B(m_B+kE_B)+kp_3^2}{E_B} e^{-E_B t}\,, \qquad (4.38d)\\
C^{B,lmn}_{\mathcal{X},\mathfrak{B},2} &= \langle \big(\gamma_4\gamma_2 \mathcal{O}^{B,lmn}_{\mathcal{X},\mathfrak{B}}(t,\mathbf{p})\big)_\tau \bar{\mathcal{N}}^B_{\tau'}(0,\mathbf{p})(\gamma_+)_{\tau'\tau}\rangle \\
&= +c_X X^B_{lmn}\sqrt{Z_B}p_2 \frac{E_B(m_B+kE_B)+kp_3^2}{E_B} e^{-E_B t}\,, \qquad (4.38e)\\
C^{B,lmn}_{\mathcal{X},\mathfrak{B},3} &= \langle \big(\gamma_4\gamma_3 \mathcal{O}^{B,lmn}_{\mathcal{X},\mathfrak{B}}(t,\mathbf{p})\big)_\tau \bar{\mathcal{N}}^B_{\tau'}(0,\mathbf{p})(\gamma_+)_{\tau'\tau}\rangle \\
&= -c_X X^B_{lmn}\sqrt{Z_B}p_3 \frac{2E_B(m_B+kE_B)+k(p_1^2+p_2^2)}{E_B} e^{-E_B t}\,, \qquad (4.38f)
\end{aligned}
$$

$$
\begin{aligned}
C^{B,lmn}_{\mathcal{X},\mathfrak{C},1} &= \langle \big(\gamma_4\gamma_1 \mathcal{O}^{B,lmn}_{\mathcal{X},\mathfrak{C}}(t,\mathbf{p})\big)_\tau \bar{\mathcal{N}}^B_{\tau'}(0,\mathbf{p})(\gamma_+)_{\tau'\tau}\rangle \\
&= -c_X X^B_{lmn}\sqrt{Z_B}p_1 \frac{E_B(m_B+kE_B)+kp_3^2}{E_B} e^{-E_B t}\,, \qquad (4.38g)\\
C^{B,lmn}_{\mathcal{X},\mathfrak{C},2} &= \langle \big(\gamma_4\gamma_2 \mathcal{O}^{B,lmn}_{\mathcal{X},\mathfrak{C}}(t,\mathbf{p})\big)_\tau \bar{\mathcal{N}}^B_{\tau'}(0,\mathbf{p})(\gamma_+)_{\tau'\tau}\rangle \\
&= +c_X X^B_{lmn}\sqrt{Z_B}p_2 \frac{E_B(m_B+kE_B)+kp_3^2}{E_B} e^{-E_B t}\,, \qquad (4.38h)\\
C^{B,lmn}_{\mathcal{X},\mathfrak{C},3} &= \langle \big(\gamma_4\gamma_3 \mathcal{O}^{B,lmn}_{\mathcal{X},\mathfrak{C}}(t,\mathbf{p})\big)_\tau \bar{\mathcal{N}}^B_{\tau'}(0,\mathbf{p})(\gamma_+)_{\tau'\tau}\rangle \\
&= +c_X X^B_{lmn}\sqrt{Z_B}p_3 \frac{k(p_1^2-p_2^2)}{E_B} e^{-E_B t}\,. \qquad (4.38i)
\end{aligned}
$$

It becomes obvious from eq. (4.38) that at least one non-zero component of spatial momentum is required to extract the first moments as each correlator is proportional to p_i. We evaluate $C^{B,lmn}_{\mathcal{X},\mathfrak{A},1}$, $C^{B,lmn}_{\mathcal{X},\mathfrak{B},1}$ and $C^{B,lmn}_{\mathcal{X},\mathfrak{C},1}$ with momentum in x direction ($\mathbf{n_p}=(\pm1,0,0)$), and $C^{B,lmn}_{\mathcal{X},\mathfrak{A},2}$, $C^{B,lmn}_{\mathcal{X},\mathfrak{B},2}$ and $C^{B,lmn}_{\mathcal{X},\mathfrak{C},2}$ with momentum in y direction ($\mathbf{n_p}=(0,\pm1,0)$). For momentum in z direction ($\mathbf{n_p}=(0,0,\pm1)$) only the correlator $C^{B,lmn}_{\mathcal{X},\mathfrak{B},3}$ can be used. We do not

consider the remaining two correlators as they require a higher number of non-vanishing momentum components, which would lead to larger statistical uncertainties.

The shape parameters defined in eqs. (4.20) can be expressed as linear combinations of V^B_{lmn}, A^B_{lmn} and T^B_{lmn} via eqs. (4.17). For the N, Σ and Ξ baryons the shape parameters are given by

$$\varphi_{11}^{B\neq\Lambda} = \tfrac{1}{2}\big([V-A]^B_{100} - 2[V-A]^B_{010} + [V-A]^B_{001}\big)\,, \tag{4.39a}$$
$$\varphi_{10}^{B\neq\Lambda} = \tfrac{1}{2}\big([V-A]^B_{100} - [V-A]^B_{001}\big)\,, \tag{4.39b}$$
$$\pi_{11}^{B\neq\Lambda} = \tfrac{1}{2}\big(T^B_{100} + T^B_{010} - 2T^B_{001}\big)\,, \tag{4.39c}$$

where $\pi^N_{11} = \varphi^N_{11}$ due to isospin symmetry. For the Λ baryon one obtains

$$\varphi_{11}^{\Lambda} = \tfrac{1}{\sqrt{6}}\big([V-A]^\Lambda_{100} - 2[V-A]^\Lambda_{010} + [V-A]^\Lambda_{001}\big)\,, \tag{4.40a}$$
$$\varphi_{10}^{\Lambda} = -\sqrt{\tfrac{3}{2}}\big([V-A]^\Lambda_{100} - [V-A]^\Lambda_{001}\big)\,, \tag{4.40b}$$
$$\pi_{10}^{\Lambda} = \sqrt{\tfrac{3}{2}}\big(T^\Lambda_{100} - T^\Lambda_{010}\big)\,. \tag{4.40c}$$

Due to the momentum conservation enforced in eq. (4.3), we can express the couplings $f^B_{(T)}$ in terms of a sum of first moments. For this purpose we define:

$$\varphi_{00,(1)}^{B\neq\Lambda} = [V-A]^B_{100} + [V-A]^B_{010} + [V-A]^B_{001}\,, \tag{4.41a}$$
$$\pi_{00,(1)}^{B\neq\Lambda} = T^B_{100} + T^B_{010} + T^B_{001}\,, \tag{4.41b}$$
$$\varphi_{00,(1)}^{\Lambda} = \sqrt{\tfrac{2}{3}}\big([V-A]^\Lambda_{100} + [V-A]^\Lambda_{010} + [V-A]^\Lambda_{001}\big)\,, \tag{4.41c}$$

where the subscript (1) indicates that these shape parameters have been obtained using the first moments instead of the zeroth moments. In the continuum, due to the Leibniz product rule for derivatives, it holds that

$$\varphi^B_{00,(1)} = \varphi^B_{00}\,, \qquad\qquad \pi^{B\neq\Lambda}_{00,(1)} = \pi^B_{00}\,. \tag{4.42}$$

The Leibniz rule is violated on the lattice due to finite lattice spacing effects. However, the relations in eqs. (4.42) have to be true again in the limit $a \to 0$, which provides a good check for the reliability of a continuum extrapolation.

It is possible to obtain the higher twist normalization constants introduced in section 4.2.2 by using correlation functions without derivatives:

$$\langle \mathcal{X}^{B,000}_\tau(t,\mathbf{p})\bar{\mathcal{N}}^B_{\tau'}(0,\mathbf{p})(\gamma_+)_{\tau'\tau}\rangle = \kappa^B_{\mathcal{X}} m_B \sqrt{Z_B}\frac{m_B + kE_B}{E_B} e^{-E_B t}\,, \tag{4.43}$$

where now $\mathcal{X}$ can be $\mathcal{S}$, $\mathcal{P}$, $\mathcal{V}$, $\mathcal{A}$ or $\mathcal{T}$ as shown in table 4.1. The couplings defined in

eqs. (4.24) and (4.25) are then given by

$$\lambda_1^{B\neq\Lambda} = -\kappa_{\mathcal{V}}^{B}\,, \qquad \lambda_2^{B\neq\Lambda} = \kappa_{\mathcal{T}}^{B}\,, \tag{4.44a}$$

$$\lambda_1^{\Lambda} = -\sqrt{6}\kappa_{\mathcal{A}}^{\Lambda}\,, \qquad \lambda_2^{\Lambda} = -2\sqrt{6}\big(\kappa_{\mathcal{S}}^{\Lambda} + \kappa_{\mathcal{P}}^{\Lambda}\big)\,, \qquad \lambda_T^{\Lambda} = -\sqrt{6}\big(\kappa_{\mathcal{S}}^{\Lambda} - \kappa_{\mathcal{P}}^{\Lambda}\big)\,. \tag{4.44b}$$

Due to symmetry properties of the associated operators it follows that

$$\kappa_{\mathcal{S}}^{B\neq\Lambda} = \kappa_{\mathcal{P}}^{B\neq\Lambda} = \kappa_{\mathcal{V}}^{\Lambda} = \kappa_{\mathcal{A}}^{B\neq\Lambda} = \kappa_{\mathcal{T}}^{\Lambda} = 0\,, \tag{4.45}$$

and the corresponding correlators vanish.

4.3.2 Details and strategy of the lattice simulation

The CLS ensembles used for the calculation of the baryon distribution amplitudes have already been introduced in section 3.3.3 and are listed in table 3.1. For each lattice, we have carried out measurements for the source positions $t_{\mathrm{src}} = 30a$, $47a$ and $65a$. Taking the average of correlators from all these different sources is not advisable as the open boundary conditions break translational invariance in time. Instead, we average suitable forward and backward propagating states, i.e., the forward direction from $t_{\mathrm{src}} = 30a$ and the backward direction from $t_{\mathrm{src}} = 65a$ as well as the forward and the backward running state from $t_{\mathrm{src}} = 47a$. The two remaining ones (backward from $t_{\mathrm{src}} = 30a$ and forward from $t_{\mathrm{src}} = 65a$) are not considered in this analysis, as sink positions closer than ~ 20 time slices to the boundary can show significant artifacts due to the open boundary conditions.

As a second step, the statistical analysis is conducted by averaging over appropriate two-point functions and momenta as outlined in section 4.3.1. For the statistical analysis we then generate 1000 bootstrap samples per ensemble using a binsize of 8 to eliminate autocorrelations. For each sample we use a χ^2-measure to simultaneously fit the two correlation functions resulting from the forward-backward averaging procedure described above.

In order to exclude contributions from excited states the choice for the lower bound of the fit range is crucial. Figure 4.4 demonstrates that, with increasing source-sink distance, the excited states decay and clear plateaus in the effective masses emerge. To determine the optimum minimal source-sink distance t_{start} we perform multiple fits with varying fit ranges for all observables. t_{start} is chosen in such a way that fits with even larger starting times no longer show any systematic trend in the fit results. As an example, figure 4.5 shows the fitted leading twist coupling constants as a function of t_{start}.

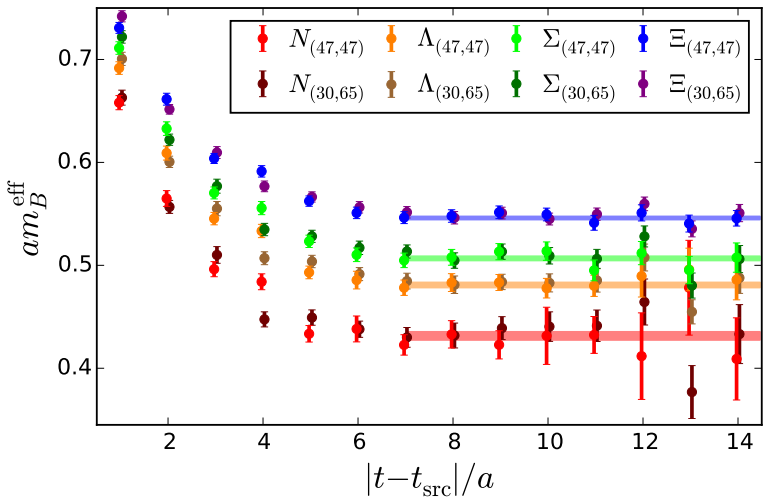

Figure 4.4: Plot showing the effective baryon masses obtained from the two forward-backward averaged smeared-smeared correlation functions in eq. (4.32) on the C101 ensemble using $\mathbf{p} = \mathbf{0}$. The plateaus start at $|t-t_{\text{src}}| = 7a$, where excited states are sufficiently suppressed. The horizontal lines represent the result of a combined fit to both correlators in the range $7a \leq |t - t_{\text{src}}| \leq 20a$.

4.4 Data analysis

In order to make physically relevant statements, the bare lattice results have to be renormalized. For this purpose we employ a non-perturbative method in a RI′/SMOM scheme and convert the results to the $\overline{\text{MS}}$ scheme using continuum perturbation theory at one-loop accuracy. In order to control operator mixing, one organizes the three-quark operators into multiplets that transform according to the five irreducible spinorial representations of the spinorial hypercubic group $\overline{\text{H}(4)}$, which are summarized in table 4.2. On the lattice, however, operators of lower dimension within the same irreducible representation can still mix with operators of higher dimension due to the dimensionful lattice spacing a [133], e.g.:

$$\mathcal{O}_i^{\overline{\text{MS}}} = Z_{ij}\mathcal{O}_j^{\text{lat}} + Z'_{ik}\frac{1}{a}\mathcal{O}_k^{\text{lat, lower dim}}. \tag{4.46}$$

As our final goal is to take the continuum limit $a \to 0$, it is obvious that this admixture should be avoided. Following table 4.2, this behavior poses no problem for the renormalization of the leading twist coupling constants f^B and the higher twist normalization constants λ^B using the operators $\mathcal{O}_{7-9}$ and $\mathcal{O}_{1-5}$, respectively, since in these cases no multiplets of lower dimension can exist. However, for the calculation of the first moments it is essential that we choose the operators $\mathcal{O}_{D5-D7}$ instead of $\mathcal{O}_{D2-D4}$, as the latter would mix under renormalization with the operators $\mathcal{O}_{7-8}$, whereas no such lower dimensional coun-

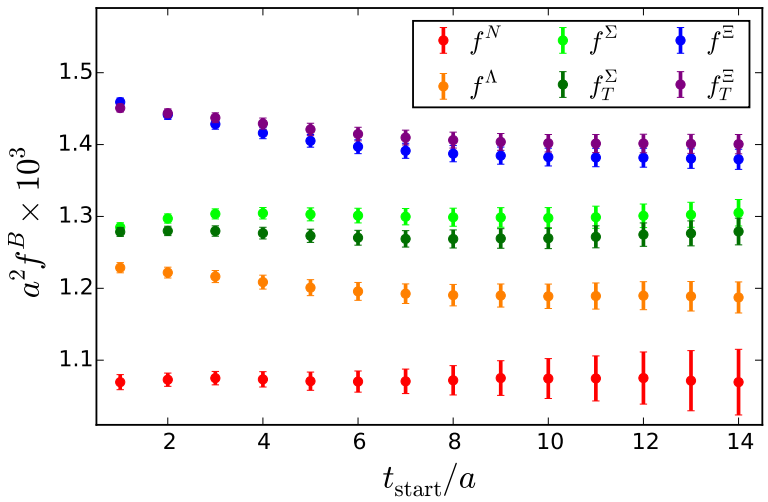

Figure 4.5: Typical plot (from the C101 ensemble) used for the determination of the fit ranges by varying the value of the minimal source-sink distance t_{start}. It shows the leading twist normalization constants obtained from the correlators given in eqs. (4.34). A conservative choice is $t_{\mathrm{start}} = 9a$, where the results have fully saturated for all leading twist couplings. A variation of the maximal source-sink separation within reasonable bounds did not have any significant impact on the result. Here it is always set to $t_{\mathrm{end}} = 20a$.

terpart exists in the representation τ_2^{12}. For a detailed treatment of the renormalization procedure we refer to [120].

Having renormalized the bare lattice results, we conduct an extrapolation to the physical point along the $\mathrm{Tr}\, M$ = const. line using the quark mass dependence derived from three-flavor baryon chiral perturbation theory (ChPT) [121, 134]. We parametrize the extrapolation using the dimensionless variable

$$\delta m = \frac{4(m_K^2 - m_\pi^2)}{3X_b^2} \propto (m_s - m_l) + \mathcal{O}((m_s - m_l)^2)\,, \tag{4.47}$$

where we start at the symmetric point $\delta m_\star = 0$ and extrapolate to the physical point

	no derivatives dimension 9/2	1 derivative dimension 11/2	2 derivatives dimension 13/2
$\tau_1^{\bar{4}}$	$\mathcal{O}_1, \mathcal{O}_2, \mathcal{O}_3, \mathcal{O}_4, \mathcal{O}_5$	...	$\mathcal{O}_{DD1}, \mathcal{O}_{DD2}, \mathcal{O}_{DD3}, ...$
$\tau_2^{\bar{4}}$			$\mathcal{O}_{DD4}, \mathcal{O}_{DD5}, \mathcal{O}_{DD6}, ...$
$\tau^{\bar{8}}$	$\mathcal{O}_6$	$\mathcal{O}_{D1}, ...$	$\mathcal{O}_{DD7}, \mathcal{O}_{DD8}, \mathcal{O}_{DD9}, ...$
$\tau_1^{\overline{12}}$	$\mathcal{O}_7, \mathcal{O}_8, \mathcal{O}_9$	$\mathcal{O}_{D2}, \mathcal{O}_{D3}, \mathcal{O}_{D4}, ...$	$\mathcal{O}_{DD10}, \mathcal{O}_{DD11}, \mathcal{O}_{DD12}, \mathcal{O}_{DD13}, ...$
$\tau_2^{\overline{12}}$		$\mathcal{O}_{D5}, \mathcal{O}_{D6}, \mathcal{O}_{D7}, \mathcal{O}_{D8}$	$\mathcal{O}_{DD14}, \mathcal{O}_{DD15}, \mathcal{O}_{DD16}, \mathcal{O}_{DD17}, \mathcal{O}_{DD18}, ...$

Table 4.2: List of three-quark operator multiplets transforming irreducibly under $\overline{\mathrm{H}(4)}$. The dimensions of the five irreducible spinorial representations $\tau_1^{\bar{4}}$, $\tau_2^{\bar{4}}$, $\tau^{\bar{8}}$, $\tau_1^{\overline{12}}$ and $\tau_2^{\overline{12}}$ are indicated by the superscripts. The nomenclature follows ref. [133].

$\delta m_{\mathrm{phys}} \approx 0.228$. We make the following ansatz for the extrapolation formulas:

$$\Phi_+^B = g_{\Phi+}^B(\delta m)\big(\Phi_+^\star + \delta m \Delta\Phi_+^B\big), \tag{4.48a}$$

$$\Phi_-^B = g_{\Phi-}^B(\delta m)\big(\Phi_-^\star + \delta m \Delta\Phi_-^B\big), \tag{4.48b}$$

$$\Pi^{B\neq\Lambda} = g_{\Pi}^B(\delta m)\big(\Phi_+^\star + \delta m \Delta\Pi^B\big), \tag{4.48c}$$

$$\Pi^{\Lambda} = g_{\Pi}^{\Lambda}(\delta m)\big(\Phi_-^\star + \delta m \Delta\Pi^{\Lambda}\big), \tag{4.48d}$$

$$\lambda_1^B = g_{\Phi-}^B(\delta m)\big(\lambda_1^\star + \delta m \Delta\lambda_1^B\big), \tag{4.48e}$$

$$\lambda_T^{\Lambda} = g_{\Pi}^{\Lambda}(\delta m)\big(\lambda_1^\star + \delta m \Delta\lambda_T^{\Lambda}\big), \tag{4.48f}$$

$$\lambda_2^B = g_{\Xi}^B(\delta m)\big(\lambda_2^\star + \delta m \Delta\lambda_2^B\big). \tag{4.48g}$$

The functions $g_{\mathrm{DA}}^B(\delta m)$ appearing in eqs. (4.48) fulfill $g_{\mathrm{DA}}^B(0) = 1$, such that eqs. (4.18) are recovered at the flavor symmetric point. They are worked out explicitly in [121] using three-flavor baryon ChPT and contain the usual chiral logs stemming from virtual pion loops. The functions $\Phi_\pm^\star$, $\Delta\Phi_\pm^B$, $\Delta\Pi^B$, $\lambda_{1,2}^\star$, $\Delta\lambda_{1,2}^B$ and $\Delta\lambda_T^{\Lambda}$ are independent of δm and act as low-energy constants (LECs) of the theory. The DAs $\Delta\Phi_\pm^B$ and $\Delta\Pi^B$ are not independent of one another as three-flavor ChPT imposes certain constraints on the SU(3) symmetry breaking. Following [121] one obtains the following relations between the leading twist DAs:

$$\Delta\Phi_\pm^N = -\Delta\Phi_\pm^\Sigma - \Delta\Phi_\pm^\Xi, \tag{4.49a}$$

$$\Delta\Pi^N = \Delta\Phi_+^N, \tag{4.49b}$$

$$\Delta\Pi^\Sigma = -\frac{1}{2}\Delta\Phi_+^\Sigma - \frac{3}{2}\Delta\Phi_+^\Lambda, \tag{4.49c}$$

$$\Delta\Pi^\Xi = \frac{1}{2}\Delta\Phi_+^\Sigma + \frac{3}{2}\Delta\Phi_+^\Lambda - \Delta\Phi_+^N, \tag{4.49d}$$

$$\Delta\Pi^\Lambda = -\frac{1}{2}\Delta\Phi_-^\Lambda - \frac{3}{2}\Delta\Phi_-^\Sigma. \tag{4.49e}$$

Analogously, the SU(3) symmetry breaking of the higher twist DAs should satisfy

$$\Delta\lambda_{1,2}^{N} = -\Delta\lambda_{1,2}^{\Sigma} - \Delta\lambda_{1,2}^{\Xi}\,, \tag{4.49f}$$

$$\Delta\lambda_{2}^{\Sigma} = -\Delta\lambda_{2}^{\Lambda}\,, \tag{4.49g}$$

$$\Delta\lambda_{T}^{\Lambda} = -\frac{1}{2}\Delta\lambda_{1}^{\Lambda} - \frac{3}{2}\Delta\lambda_{1}^{\Sigma}\,. \tag{4.49h}$$

In practice, we can enforce these constraints by replacing the respective DAs with the linear combinations of eq. (4.49) in our χ^2 fit function, which effectively reduces the number of free parameters in the fit. We have performed both constrained and unconstrained fits to the renormalized lattice data as shown in figures 4.6–4.11. It turns out that the lattice data is not always adequately described by a constrained fit. This is reflected in a poor χ^2 value for the fits of the leading twist normalization constants f^B and $f_T^{B\neq\Lambda}$, as well as for $\varphi_{00,(1)}^B$ and $\pi_{00,(1)}^{B\neq\Lambda}$. Alongside the high χ^2 value, the discrepancies also become obvious to the naked eye when considering the left plots in figures 4.6 and 4.9, where, for example, the orange extrapolation lines for the Λ do not agree with the orange points within the errors. We stress that this is not a specific problem for the Λ baryon but rather a consequence of the constraints in eqs. (4.49). We could in principle force the χ^2 minimizer to align the orange lines and points perfectly at the cost of a slightly higher minimum. However, this would only shift the problem to other particles due to the constraints. The situation is similar for the higher twist normalization constants λ_2^B in figure 4.8, where, for example, the red points for the nucleon do not follow the shape of the extrapolation line in an acceptable manner. On the contrary, we obtain comparable good values of χ^2 for both fits, constrained and unconstrained, for quantities like λ_1^B and λ_T^Λ, and for the first moments of Φ_-^B and Π^Λ (φ_{10}^B and π_{10}^Λ), which have the same chiral behavior as λ_1^B and λ_T^Λ, see figures 4.7 and 4.11. The constraints are also reasonably well fulfilled for the first moments φ_{11}^B and $\pi_{11}^{B\neq\Lambda}$, which appear in Φ_+^B and $\Pi^{B\neq\Lambda}$, and are predicted to have the same chiral logarithms as the couplings f^B and $f_T^{B\neq\Lambda}$, see figure 4.10.

The problems one encounters for certain observables with a constrained approach may stem from various reasons. As the ChPT calculation was carried out in leading one-loop order, higher order effects could be particularly large for these observables. Finite volume effects could also be responsible for these discrepancies, however, considering that the spatial extents of our lattices in table 3.1 fulfill $m_\pi L \gtrsim 4$ with $L > 2.7$ fm, this seems rather unlikely, cf. [44, 135, 136]. Certainly, the claimed constraints in eqs. (4.49) were derived in a continuum theory and are therefore only true in the limit $a \to 0$. This makes cut-off effects a probable reason for the observed behavior. In particular lattice spacing effects have already been identified as a major source of systematic uncertainty in the two-flavor calculation of ref. [44], where it was also argued that for the leading twist normalization constants discretization effects are expected to be larger than for the higher twist couplings.

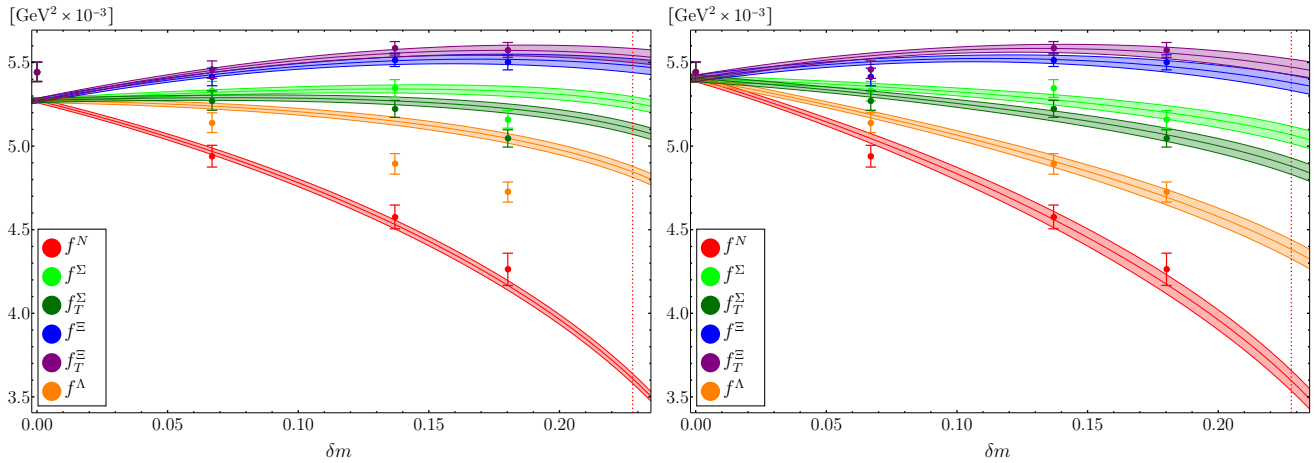

Figure 4.6: Constrained fit (left, 4 parameters) and unconstrained fit (right, 7 parameters) for the leading twist normalization constants f^N, f^Σ, f_T^Σ, f^Ξ, f_T^Ξ and f^Λ.

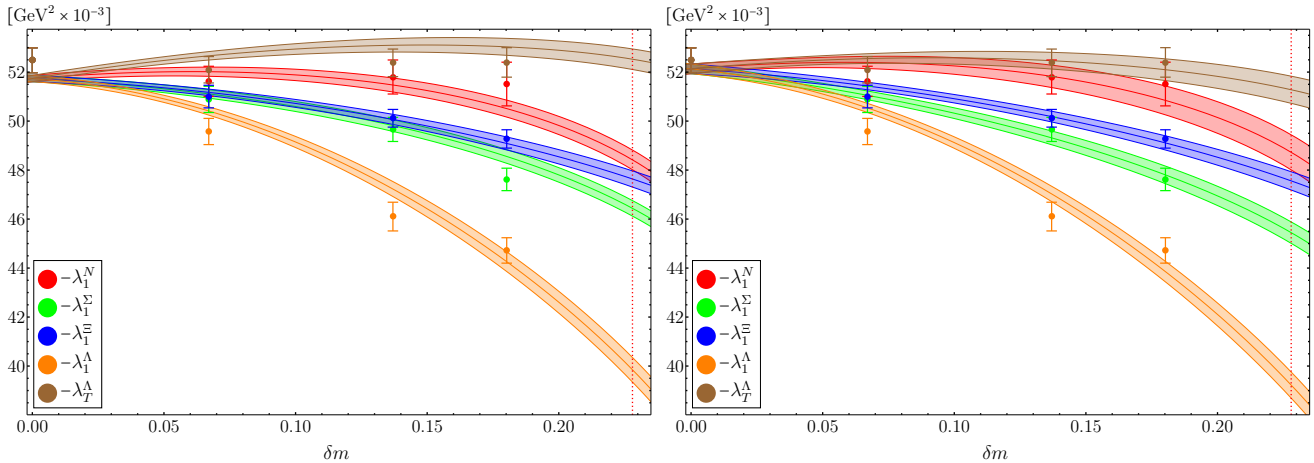

Figure 4.7: Constrained fit (left, 4 parameters) and unconstrained fit (right, 6 parameters) for the chiral odd higher twist normalization constants λ_1^N, λ_1^Σ, λ_1^Ξ, λ_1^Λ and λ_T^Λ.

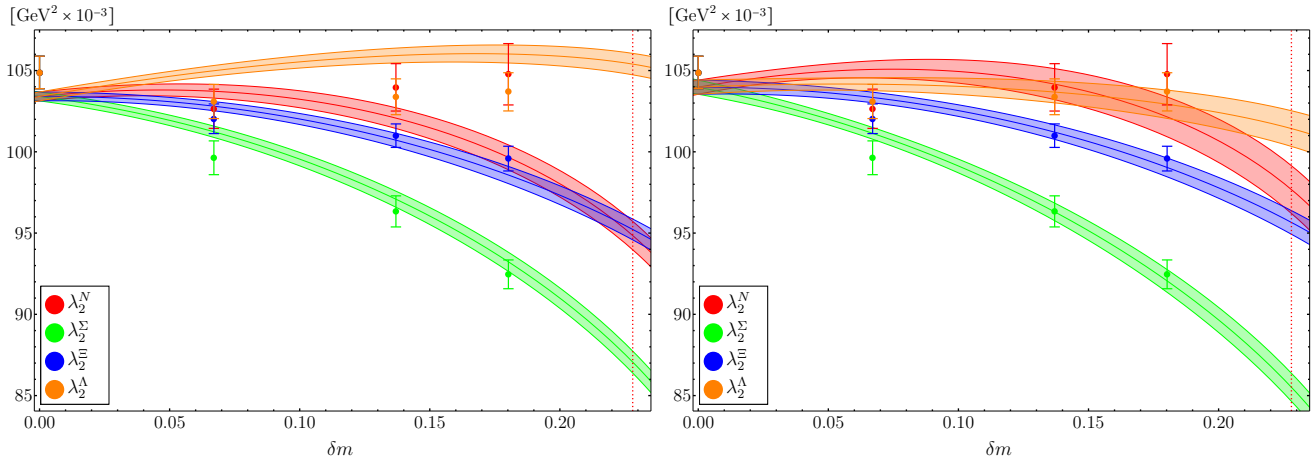

Figure 4.8: Constrained fit (left, 3 parameters) and unconstrained fit (right, 5 parameters) for the chiral even higher twist normalization constants λ_2^N, λ_2^Σ, λ_2^Ξ and λ_2^Λ.

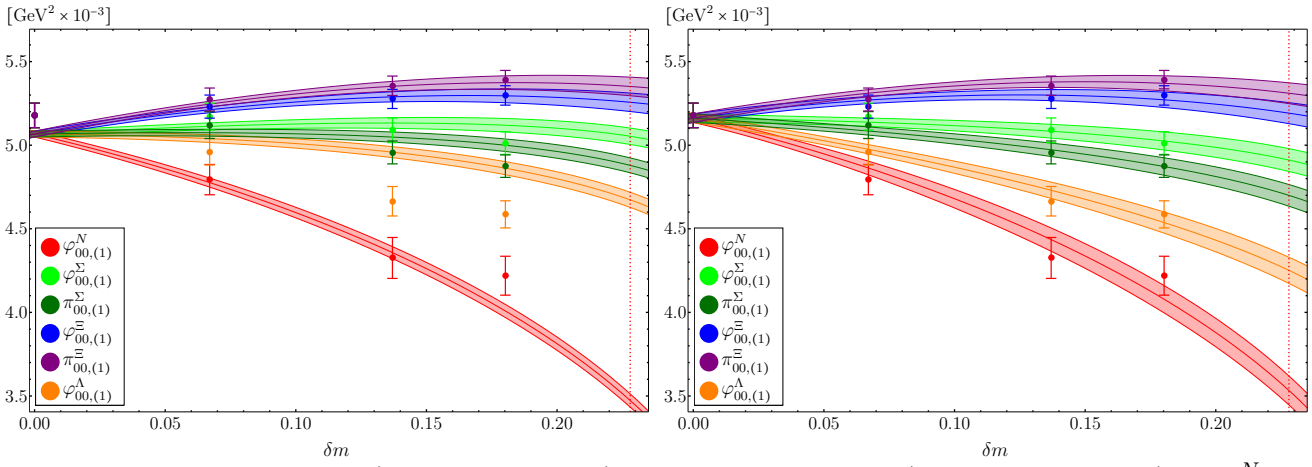

Figure 4.9: Constrained fit (left, 4 parameters) and unconstrained fit (right, 7 parameters) for $\varphi^N_{00,(1)}$, $\varphi^\Sigma_{00,(1)}$, $\pi^\Sigma_{00,(1)}$, $\varphi^\Xi_{00,(1)}$, $\pi^\Xi_{00,(1)}$ and $\varphi^\Lambda_{00,(1)}$ of the leading twist DAs Φ^B_+ and $\Pi^{B\neq\Lambda}$. These moments should be equivalent to the leading twist normalization constants in the continuum (cf. figure 4.6).

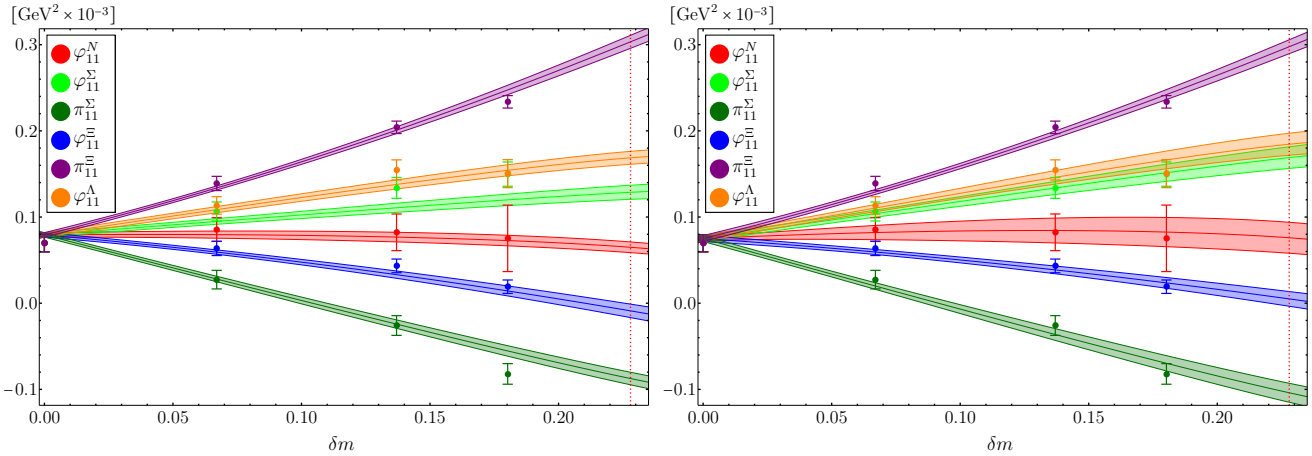

Figure 4.10: Constrained fit (left, 4 parameters) and unconstrained fit (right, 7 parameters) for the first moments φ^N_{11}, φ^Σ_{11}, π^Σ_{11}, φ^Ξ_{11}, π^Ξ_{11} and φ^Λ_{11} of the leading twist DAs Φ^B_+ and $\Pi^{B\neq\Lambda}$.

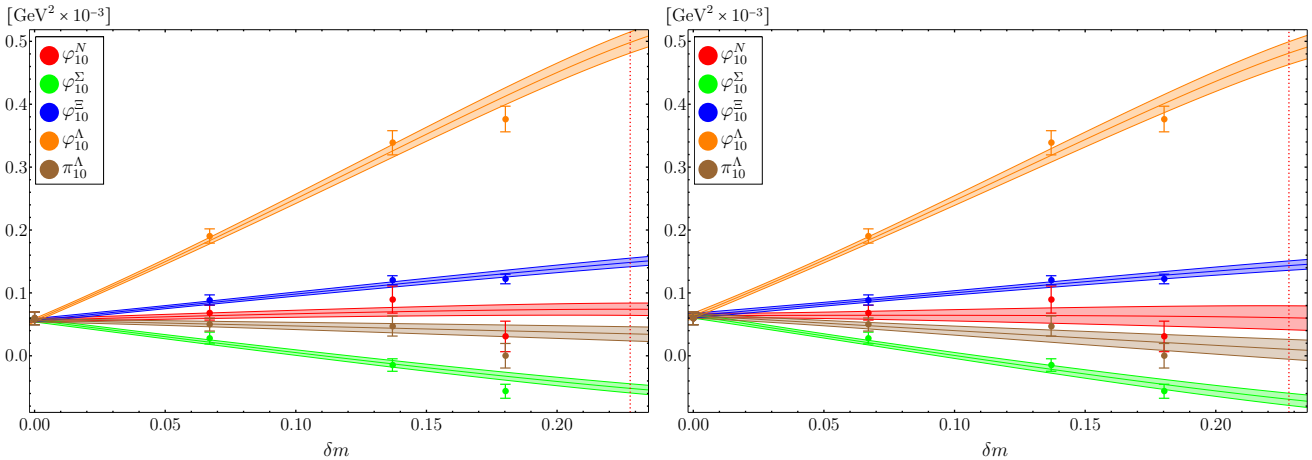

Figure 4.11: Constrained fit (left, 4 parameters) and unconstrained fit (right, 6 parameters) for the first moments φ^N_{10}, φ^Σ_{10}, φ^Ξ_{10}, φ^Λ_{10} and π^Λ_{10} of the leading twist DAs Φ^B_- and Π^Λ.

We can try to account for the leading discretization effects by constructing an ansatz that recovers the continuum formulas in eqs. (4.48) in the limit $a \to 0$. Since the operators we use are not $\mathcal{O}(a)$ improved we assume the leading corrections to be linear in a. At fixed mean quark mass this would yield, for instance, for the leading twist couplings:

$$f^B = g^B_{\Phi_+}(\delta m)\big(1 + aC + a\delta m D^B\big)\big(f^\star + \delta m \Delta f^B\big)\,, \tag{4.50a}$$

$$f_T^{B\neq\Lambda} = g^B_{\Pi}(\delta m)\big(1 + aC + a\delta m D^B_T\big)\big(f^\star + \delta m \Delta f^B_T\big)\,. \tag{4.50b}$$

The constant C has to be equal for all baryons in the octet, while the $D^B_{(T)}$ can be different and are not necessarily subject to the same constraints as $\Delta f^B_{(T)}$. One can easily convince oneself that, at non-zero lattice spacing, terms $\mathcal{O}(a\delta m)$ can override the effect of the constraints given in eqs. (4.49). Note that it is actually rather natural to assume that discretization effects break the continuum constraints obtained from ChPT, since Wilson fermions break chiral symmetry by construction. However, the symmetry is recovered when taking the continuum limit, which is also reflected correctly in eqs. (4.50).

As we only use data at a single lattice spacing in this work, we cannot study discretization effects here and take the difference between constrained and unconstrained fits as evidence for systematic uncertainties.

4.5 Results

The extrapolated results at the physical point δm_{phys} are summarized in table 4.3 for the constrained fit and table 4.4 for the unconstrained fit. For all quantities the first error refers to a combined statistical and extrapolation error, while the second error is an estimate of the uncertainty due to the renormalization procedure. As already mentioned in the previous section, we estimate any finite volume effects to be small due to the relatively large size of our lattices. Since the overall quality of the unconstrained fit is better, indicated by $\chi^2/\text{d.o.f.} < 1.5$ for all observables, we present the corresponding numbers as our final results for this lattice spacing (see table 4.4) and view the differences compared to the constrained chiral extrapolation as part of the systematic uncertainty. All further tables and figures in this section are generated using these values.

For the case of the nucleon, we can compare our results to a previous $N_f = 2$ lattice study [44], where a continuum extrapolation was performed for f^N as well as for the higher twist normalization constants λ_1^N and λ_2^N. It turns out that our results at $a \approx 0.0857$ fm are approximately 30% larger for f^N and about 20% larger for λ_1^N and λ_2^N than the continuum extrapolated results. However, including the fact that the continuum extrapolation of lattices in the region $a \approx 0.06 - 0.08$ fm decreases f^N and $\lambda_{1,2}^N$ by a similar percentage, which is shown in figure 7 of [44],[4] our results are in fact very compatible. Given that we

[4] We refer to the figure numbers of the journal version of ref. [44].

B	N	Σ	Ξ	Λ
$f^B \times 10^3$	3.61(3)(1)	5.26(4)(2)	5.48(4)(2)	4.85(3)(2)
$f_T^B \times 10^3$	3.61(3)(1)	5.10(3)(2)	5.54(4)(2)	—
$\varphi_{11}^B \times 10^3$	0.06(1)(1)	0.13(1)(2)	−0.01(1)(3)	0.17(1)(1)
$\pi_{11}^B \times 10^3$	0.06(1)(1)	−0.09(1)(3)	0.30(1)(1)	—
$\varphi_{10}^B \times 10^3$	0.074(10)(4)	−0.052(7)(2)	0.15(1)(1)	0.50(2)(3)
$\pi_{10}^B \times 10^3$	—	—	—	0.035(11)(2)
$\varphi_{00,(1)}^B \times 10^3$	3.47(4)(2)	5.05(5)(2)	5.26(6)(2)	4.67(5)(2)
$\pi_{00,(1)}^B \times 10^3$	3.47(4)(2)	4.88(4)(2)	5.35(6)(2)	—
$\lambda_1^B \times 10^3$	−48.4(4)(23)	−46.4(3)(22)	−47.6(3)(23)	−40(1)(2)
$\lambda_T^B \times 10^3$	—	—	—	−52.5(4)(25)
$\lambda_2^B \times 10^3$	95(1)(5)	87(1)(4)	95(1)(5)	105(1)(5)

Table 4.3: Couplings and shape parameters obtained by the constrained fit method. All values are given in units of GeV^2 in the $\overline{\mathrm{MS}}$ scheme at a scale $\mu^2 = 4\ \mathrm{GeV}^2$. The number in the first parentheses gives a combined statistical and chiral extrapolation error. The second one is an estimate of the error due to the renormalization procedure.

use a similar lattice action, we have to expect discretization effects of the same magnitude as in [44], and therefore, a thorough continuum extrapolation is crucial and a primary goal for future studies. Our results for the momentum sums $\varphi_{00,(1)}^B$ and $\pi_{00,(1)}^B$ are within 5% of the corresponding couplings, which allows us to expect that this difference will vanish in the limit $a \to 0$, as discretization errors in the derivatives seem to be under control, cf. figure 8 in ref. [44].

Our results for the nucleon shape parameters $\varphi_{11}^N = \pi_{11}^N$ and φ_{10}^N agree with the results in ref. [44][5] as well as with the parameters extracted from the study of the nucleon electromagnetic form factors in light-cone sum rules [137]. Note that our φ_{nk}^N correspond to $f_N \varphi_{nk}^N$ in refs. [44, 137]. In agreement with ref. [44], we also observe the approximate equality $\varphi_{10}^N \approx \varphi_{11}^N$. Compared to QCD sum rule calculations [138], our results for the shape parameters of hyperons are up to an order of magnitude smaller as shown in table 4.5. This phenomenon has already been observed as ref. [44] states that, in general, modern lattice simulations and light-cone sum rule calculations yield estimates of the first moments of the nucleon DA that are one order of magnitude smaller than in "old" phenomenological papers, cf. refs. [25, 138]. Our measurements confirm this observation also for the hyperons.

It is interesting to note that the SU(3) breaking in the shape parameters of the octet baryons turns out to be large, e.g., $\pi_{11}^\Xi \gtrsim 3\varphi_{11}^N$ and $\varphi_{10}^\Lambda \gtrsim 7\varphi_{10}^N$. This relative effect is much stronger than predicted by QCD sum rule calculations [138], even though the absolute values are much smaller. As the shape parameters have autonomous scale dependence

[5] Note that in [44] no continuum extrapolation has been performed for the first moments.

B	N	Σ	Ξ	Λ
$f^B \times 10^3$	3.60(6)(2)	5.07(5)(2)	5.38(5)(2)	4.38(6)(2)
$f_T^B \times 10^3$	3.60(6)(2)	4.88(5)(2)	5.47(5)(2)	—
$\varphi_{11}^B \times 10^3$	0.08(2)(1)	0.17(1)(2)	0.01(1)(2)	0.18(1)(1)
$\pi_{11}^B \times 10^3$	0.08(2)(1)	−0.10(1)(3)	0.30(1)(1)	—
$\varphi_{10}^B \times 10^3$	0.060(19)(3)	−0.069(10)(3)	0.14(1)(1)	0.48(2)(3)
$\pi_{10}^B \times 10^3$	—	—	—	0.010(16)(1)
$\varphi_{00,(1)}^B \times 10^3$	3.53(9)(2)	4.91(7)(2)	5.19(6)(2)	4.25(8)(2)
$\pi_{00,(1)}^B \times 10^3$	3.53(9)(2)	4.70(6)(2)	5.31(6)(2)	—
$\lambda_1^B \times 10^3$	−49(1)(2)	−45.4(4)(21)	−47.6(4)(23)	−39(1)(2)
$\lambda_T^B \times 10^3$	—	—	—	−51(1)(2)
$\lambda_2^B \times 10^3$	98(1)(5)	86(1)(4)	96(1)(5)	101(1)(5)

Table 4.4: Couplings and shape parameters obtained from the unconstrained fits. All values are given in units of GeV^2 in the $\overline{\text{MS}}$ scheme at a scale $\mu^2 = 4\,\text{GeV}^2$. The number in the first parentheses gives a combined statistical and chiral extrapolation error. The second one is an estimate of the error due to the renormalization procedure. The numbers from this table should be quoted as the final results at our lattice spacing.

and should be viewed as independent non-perturbative parameters, the observed large SU(3) breaking effects for the shape parameters are unexpected and in stark contrast to the situation for the normalization constants, where the differences between octet baryons are at most 50%. As a consequence, SU(3) breaking in hard exclusive reactions that are sensitive to the deviations of the DAs from their asymptotic form can be enhanced.

Since the absolute values of the asymptotic DAs are much bigger than the shape parameters themselves, the mentioned SU(3) breaking effects are best visualized by subtracting the asymptotic DAs from $[V-A]^B$ and T^B, as shown in figure 4.12. As a consequence of the approximate equality of the two nucleon shape parameters φ_{10}^N and φ_{11}^N, we observe an approximate symmetry of $[V-A]^N$ under the exchange of x_2 and x_3. We note that this is a non-trivial result in contrast to the behavior of the amplitudes $T^{B\neq\Lambda}$, which are merely by construction symmetric under the interchange of x_1 and x_2. In the nucleon Fock state $u^\uparrow u^\downarrow d^\uparrow$ this is equivalent to a symmetric distribution of momentum between the second and third quark. In agreement with earlier studies [44, 138, 140], we observe that the "leading" $u^\uparrow$ quark, which has the same helicity as the nucleon, carries a larger momentum fraction. In the $u^\uparrow u^\uparrow d^\downarrow$ nucleon state, which is described by T^N, the peak of the distribution is shifted towards the two u quarks in a symmetric manner. T^N, however, is not an independent DA. Taking into account the isospin relation (4.14), the spin-flavor structure of the nucleon light-cone wave function (4.22a) can be presented, schematically, as $[V-A]^N u^\uparrow(u^\downarrow d^\uparrow - d^\downarrow u^\uparrow)$. In this picture our result for $[V-A]^N$ corresponds to a shift of the momentum distribution towards the $u^\uparrow$ quark, which again carries the nucleon helicity.

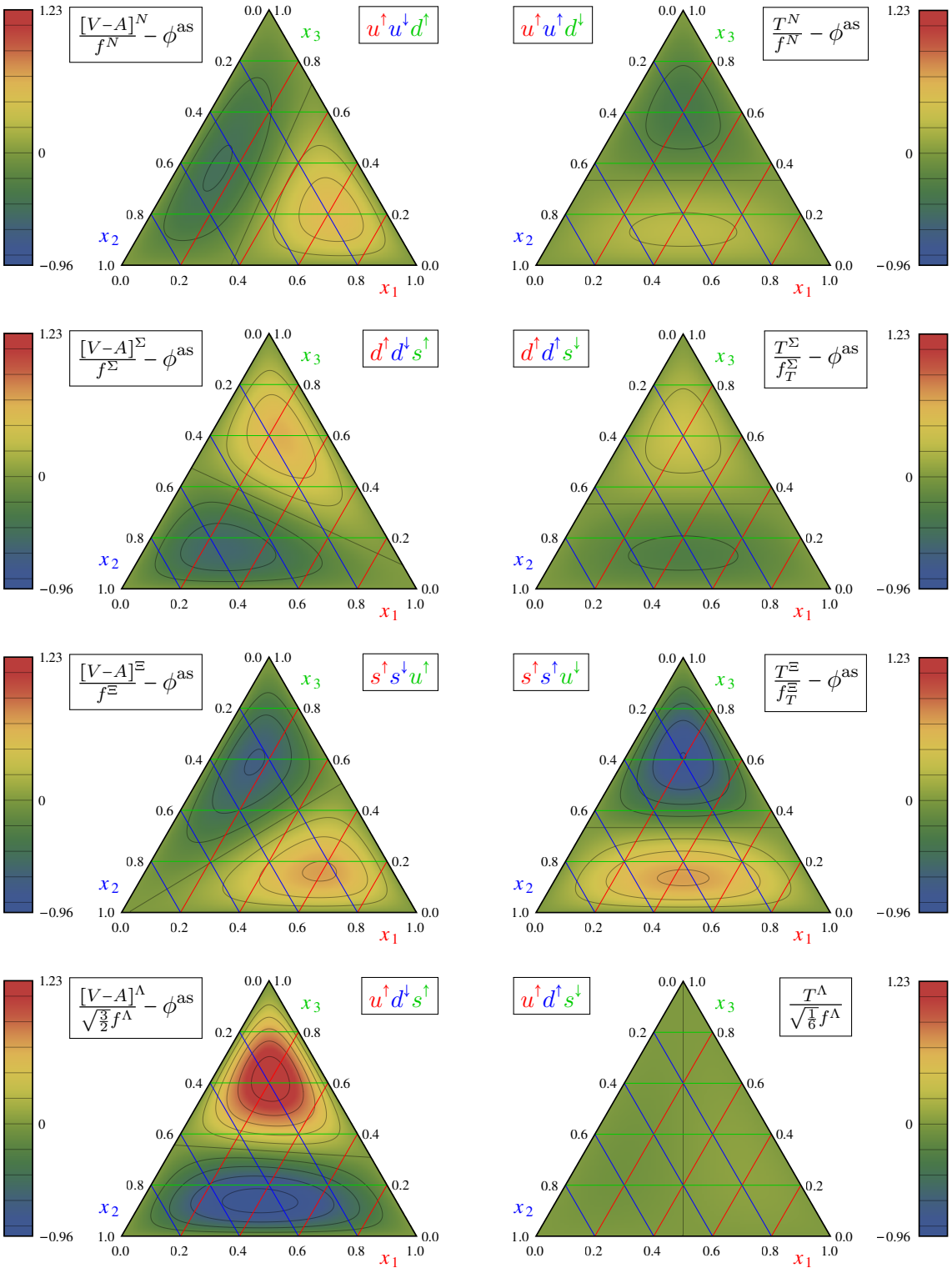

Figure 4.12: Barycentric plots ($x_1+x_2+x_3 = 1$) showing the deviations of the DAs $[V-A]^B$ and T^B from the asymptotic shape $\phi^{\text{as}} \equiv 120 x_1 x_2 x_3$. T^Λ vanishes in the asymptotic limit, see eq. (4.20d). In this representation the coordinates x_i directly correspond to quarks of definite flavor and helicity.

B	work	method	$f^B \times 10^3$	$f_T^B \times 10^3$	$\varphi_{11}^B \times 10^3$	$\pi_{11}^B \times 10^3$	$\varphi_{10}^B \times 10^3$	$\pi_{10}^B \times 10^3$
N	ours	$N_f = 2+1$	3.60	3.60	0.08	0.08	0.06	—
	[44]	$N_f = 2$	2.84	2.84	0.085	0.085	0.082	—
	[138]	COZ	4.55	4.55	0.885	0.885	0.748	—
Σ	ours	$N_f = 2+1$	5.07	4.88	0.17	−0.10	−0.069	—
	[138]	COZ	4.65	4.46	1.11	0.511	0.523	—
Ξ	ours	$N_f = 2+1$	5.38	5.47	0.01	0.30	0.14	—
	[138]	COZ	4.83	4.92	0.685	1.10	0.883	—
Λ	ours	$N_f = 2+1$	4.38	—	0.18	—	0.48	0.01
	[138]	COZ	4.69	—	1.05	—	1.39	1.32

Table 4.5: Comparison of the central values of our $N_f = 2+1$ results (unconstrained fit, see table 4.4) with the $N_f = 2$ lattice study for the nucleon [44] and the Chernyak–Ogloblin–Zhitnitsky (COZ) model [138]. All values are given in units of GeV^2. All quantities have been converted to the conventions established in this work and rescaled to $\mu^2 = 4\,\mathrm{GeV}^2$, using the three-loop evolution equation for the couplings with the anomalous dimensions calculated in ref. [139], and the one-loop equation for the shape parameters. Note that f_Λ^T in ref. [138] is proportional to the first moment π_{10}^Λ in our nomenclature.

For the Σ baryon state $d^\uparrow d^\downarrow s^\uparrow$ one sees that the maximum of the distribution is shifted from $d^\downarrow$ towards $s^\uparrow$, whereas in the $d^\uparrow d^\uparrow s^\downarrow$ state the s quark gathers additional momentum from both d quarks equally. The overall size of the deviations from the asymptotic distribution is, however, quite small, similar to the nucleon case. For the Ξ baryon the deviations are slightly larger. In the $s^\uparrow s^\downarrow u^\uparrow$ state, the distribution is tilted towards the $s^\uparrow$ quark and leaves less momentum for the $u^\uparrow$ quark. T^Ξ is clearly dominated by the two s quarks. In summary, for the isospin-nonsinglet baryons one can identify two competing patterns: First, the strange quarks carry, in general, a larger fraction of the momentum. This behavior can be explained with the fact that the mass of the strange quarks is much higher compared to the light quarks. Second, in the $|\uparrow\downarrow\uparrow\rangle$ state the first quark is favored over the second, while in the $|\uparrow\uparrow\downarrow\rangle$ state the first two quarks behave identically. These rules do not apply to the Λ baryon due to its reversed symmetry properties, see eqs. (4.13): In the $u^\uparrow d^\downarrow s^\uparrow$ state the maximum of the distribution is shifted towards the s quark. T^Λ is a special case, since it does not contain the leading asymptotic part due to the antisymmetry under exchange of x_1 and x_2. Hence, for the Λ baryon, the Fock state $u^\uparrow d^\uparrow s^\downarrow$ is expected to be highly suppressed.

Having calculated the first order shape parameters of the DAs allows us additionally to determine the so-called average momentum fractions, defined as

$$\langle x_i \rangle^B = \frac{1}{\varphi_{00,(1)}^B} \int [dx]\, x_i [V-A]^B\,, \qquad \langle x_i \rangle_T^{B\neq\Lambda} = \frac{1}{\pi_{00,(1)}^B} \int [dx]\, x_i T^B\,. \tag{4.51}$$

B	N		Σ		Ξ		Λ	
$\langle x_1\rangle^B$	$u^\uparrow$	0.358	$d^\uparrow$	0.331	$s^\uparrow$	0.361	$u^\uparrow$	0.310
$\langle x_2\rangle^B$	$u^\downarrow$	0.319	$d^\downarrow$	0.310	$s^\downarrow$	0.333	$d^\downarrow$	0.304
$\langle x_3\rangle^B$	$d^\uparrow$	0.323	$s^\uparrow$	0.359	$u^\uparrow$	0.306	$s^\uparrow$	0.386
$\langle x_1\rangle_T^B$	$u^\uparrow$	0.340	$d^\uparrow$	0.326	$s^\uparrow$	0.352	—	
$\langle x_2\rangle_T^B$	$u^\uparrow$	0.340	$d^\uparrow$	0.326	$s^\uparrow$	0.352	—	
$\langle x_3\rangle_T^B$	$d^\downarrow$	0.319	$s^\downarrow$	0.348	$u^\downarrow$	0.296	—	

Table 4.6: Normalized first moments of the DAs $[V-A]^B$ and $T^{B\neq\Lambda}$ in the $\overline{\text{MS}}$ scheme at a scale $\mu^2 = 4\,\text{GeV}^2$, obtained via eq. (4.52).

Note that the name momentum fraction is somewhat misleading as this indicates averaging with respect to the full wave function squared instead of the DA. The various $\langle x_i\rangle$ can be calculated as follows:

$$\langle x_1\rangle^{B\neq\Lambda} = \frac{1}{3} + \frac{1}{3}\widehat{\varphi}_{11}^B + \widehat{\varphi}_{10}^B\,, \qquad \langle x_2\rangle^{B\neq\Lambda} = \frac{1}{3} - \frac{2}{3}\widehat{\varphi}_{11}^B\,, \quad \langle x_3\rangle^{B\neq\Lambda} = \frac{1}{3} + \frac{1}{3}\widehat{\varphi}_{11}^B - \widehat{\varphi}_{10}^B\,, \tag{4.52a}$$

$$\langle x_1\rangle_T^{B\neq\Lambda} = \frac{1}{3} + \frac{1}{3}\widehat{\pi}_{11}^B\,, \qquad \langle x_2\rangle_T^{B\neq\Lambda} = \frac{1}{3} + \frac{1}{3}\widehat{\pi}_{11}^B\,, \quad \langle x_3\rangle_T^{B\neq\Lambda} = \frac{1}{3} - \frac{2}{3}\widehat{\pi}_{11}^B\,, \tag{4.52b}$$

$$\langle x_1\rangle^{\Lambda} = \frac{1}{3} + \frac{1}{3}\widehat{\varphi}_{11}^\Lambda - \frac{1}{3}\widehat{\varphi}_{10}^\Lambda\,, \qquad \langle x_2\rangle^{\Lambda} = \frac{1}{3} - \frac{2}{3}\widehat{\varphi}_{11}^\Lambda\,, \qquad \langle x_3\rangle^{\Lambda} = \frac{1}{3} + \frac{1}{3}\widehat{\varphi}_{11}^\Lambda + \frac{1}{3}\widehat{\varphi}_{10}^\Lambda\,, \tag{4.52c}$$

where

$$\widehat{\varphi}_{nk}^B = \frac{\varphi_{nk}^B}{\varphi_{00,(1)}^B}\,, \qquad\qquad \widehat{\pi}_{11}^{B\neq\Lambda} = \frac{\pi_{11}^B}{\pi_{00,(1)}^B}\,. \tag{4.53}$$

The results are summarized in table 4.6 and support the qualitative picture suggested by the discussion of figure 4.12.

Regarding the higher twist matrix elements λ_i^B, which correspond to the normalization of the P-wave light-cone wave functions and appear as LECs in effective theories for generic GUT models [128], we make the following observations: Our results confirm very well the already known relation [117, 132]

$$\lambda_2^N \approx -2\lambda_1^N\,. \tag{4.54}$$

In addition, we can generalize this statement also to the Σ and Ξ hyperons but not to the Λ baryon. Instead, we find

$$\lambda_2^\Lambda \approx -2\lambda_T^\Lambda\,. \tag{4.55}$$

The likely interpretation (similar to the familiar relations for isospin-nonsinglet baryons) is that the corresponding matrix elements vanish in the non-relativistic quark model limit.

4.6 Summary and outlook

The main achievement of the work presented in this chapter is the calculation of the normalization constants and the first moments of the octet baryon distribution amplitudes using $N_f = 2+1$ dynamical fermions. To this end, we have analysed lattice ensembles with pion masses down to 222 MeV at a single lattice spacing of $a \approx 0.0857$ fm. The quark masses of the lattices were chosen such that the normalized average quadratic meson mass corresponds to its physical value, i.e., they fulfill $\mathrm{Tr}\, M = \text{const}$. We have performed a non-perturbative renormalization in an RI′/SMOM scheme, followed by a conversion to the $\overline{\mathrm{MS}}$ scheme applying continuum perturbation theory at one-loop accuracy [120]. The renormalized lattice results have been extrapolated to the physical point using formulas derived from three-flavor baryon chiral perturbation theory [121]. The resulting leading twist normalization constants show definite SU(3) flavor breaking effects

$$\frac{f^\Sigma}{f^N} = 1.41(4)\,, \quad \frac{f_T^\Sigma}{f^N} = 1.36(4)\,, \quad \frac{f^\Xi}{f^N} = 1.50(4)\,, \quad \frac{f_T^\Xi}{f^N} = 1.52(4)\,, \quad \frac{f^\Lambda}{f^N} = 1.22(4)\,, \tag{4.56}$$

whereas the breaking for the higher twist couplings turns out to be somewhat smaller

$$\frac{\lambda_1^\Sigma}{\lambda_1^N} = 0.93(2)\,, \qquad \frac{\lambda_1^\Xi}{\lambda_1^N} = 0.98(2)\,, \qquad \frac{\lambda_1^\Lambda}{\lambda_1^N} = 0.81(2)\,, \qquad \frac{\lambda_T^\Lambda}{\lambda_1^N} = 1.05(3)\,. \tag{4.57}$$

The magnitude of the shape parameters represents a measure for the deviation of the respective DA from its asymptotic limit. In agreement with previous lattice results for the nucleon [44], we find that the shape parameters of the octet baryons are rather small. In particular, we obtain much smaller values than old QCD sum rule calculations [138]. In spite of this, we observe large SU(3) breaking effects of the shape parameters, see table 4.4. We identify two competing patterns for the isospin-nonsinglet baryons: First, the momentum is generally shifted towards strange quarks. Second, the first quark is favored over the second one in the $f^\uparrow g^\downarrow h^\uparrow$ state, while in the $f^\uparrow g^\uparrow h^\downarrow$ state the first two quarks behave identically. This behavior does not apply to the Λ baryon due to its reversed symmetry properties. The interplay of these two patterns leads to the rather elaborate structure shown in figure 4.12.

Regarding our chiral extrapolations, the symmetry constraints in eqs. (4.49) can only be implemented with a varying degree of success. As these relations stem from continuum ChPT calculations and since we use Wilson fermions which explicitly break chiral symmetry at $a \neq 0$, we have identified lattice spacing effects as a possible origin of this problem. Moreover, previous studies suggest that the extrapolation $a \to 0$ affects the normalization constants at our lattice spacing up to $20 - 30\%$. Therefore, in order to obtain physical results, our next goal is to conduct a controlled continuum extrapolation by including various CLS ensembles with a wide range of lattice spacings.

5 Meson distribution amplitudes

5.1 Pion distribution amplitude

5.1.1 Overview

The pion DA is maybe the simplest test case of DAs and has been studied over decades. Nevertheless, its shape is still hotly debated as seen for the classical example of the experimentally accessible $\gamma\gamma^* \to \pi^0$ process, cf. figure 5.1, which can be used to test QCD factorization. Over the past years, partially disagreeing measurements of the BaBar- [141] and Belle-collaboration [142] of this form factor have fueled intense discussions [143–147] about this process and even caused speculations about a possible breakdown of QCD factorization [148].

Like all distribution amplitudes, the pion DA is universal, i.e., once determined, it can be used to describe other hard exclusive processes that involve a pion. Prominent examples, which are important for the determination of the quark mixing matrix in the Standard Model, are the semileptonic $B^\pm \to \pi^0 l^\pm \nu_l$ decays [149–151], as well as the weak $B \to \pi\pi$ hadronic decays [152, 153].

As for the baryon DAs, the standard lattice approach employs local operators to calculate Mellin moments of the pion distribution amplitude. There also exist alternative methods [154–157] for the direct calculation of the distribution amplitude in position-space which, however, all require large hadron momenta on the lattice. With the development of

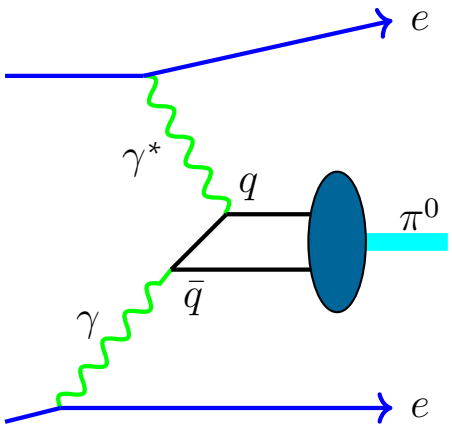

Figure 5.1: Leading Feynman diagram for the process $\gamma\gamma^* \to q\bar{q} \to \pi^0$.

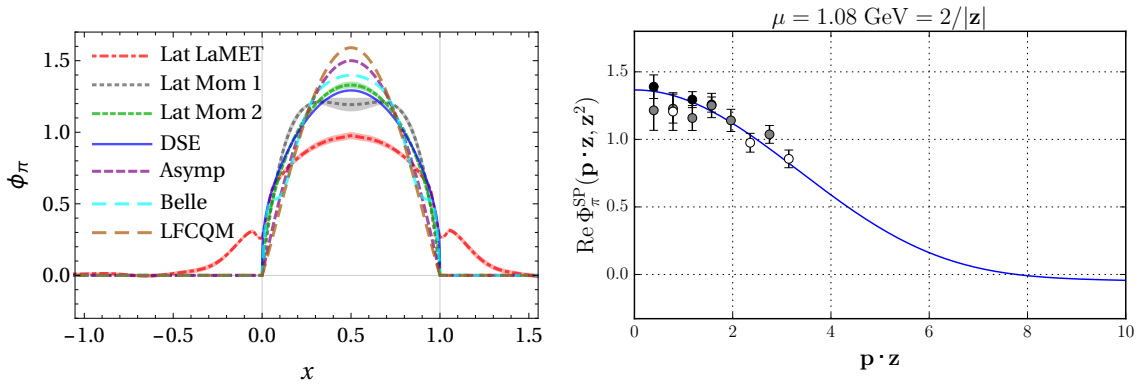

Figure 5.2: This figure is taken from [159] and shows a comparison of various determinations of the pion distribution amplitude. **Left:** Results for $\phi(x)$ obtained from the large-momentum effective theory (Lat LaMET) [159], the standard Mellin moment method (Lat Mom 1 and Lat Mom 2) [42], a Dyson–Schwinger equation approach (DSE) [160], a fit to the Belle data [146] and a calculation using the light-front constituent quark model (LFCQM) [161]. The DA in the asymptotic limit (Asymp) is given by $6x(1-x)$. **Right:** Plot showing the pseudoscalar-scalar channel of the Braun–Müller approach [154] as a function of the product of the pion momentum $\mathbf{p}$ and the spatial distance $\mathbf{z}$ of the two currents. The data points were calculated in ref. [162] while the blue curve was determined using the one-loop coefficient function for the scalar-pseudoscalar channel from [162] evaluated with the distribution amplitude of the LaMET approach [159] together with sum rule estimates for the higher twist normalization [163].

the momentum smearing technique [158], these approaches became applicable in practice, see for example figure 5.2. In [154] one calculates matrix elements of space-like separated currents,

$$T(pz, z^2) = \langle 0|\bar{d}(\mathbf{z}/2)\Gamma_1 q(\mathbf{z}/2)\bar{q}(-\mathbf{z}/2)\Gamma_2 u(-\mathbf{z}/2)|\pi^+(p)\rangle\,, \tag{5.1}$$

and matches them to the corresponding pQCD factorization in terms of the distribution amplitude. In this way, the renormalization problem for composite lattice operators is completely avoided, but in return, a large spatial momentum is required in order to become sensitive to the DA. We have successfully applied the position-space method to a single ensemble with a pion mass of $m_\pi \approx 295$ MeV in a recent publication [162]. This approach, however, is still in its early stages as even though we employed momentum smearing, the accessible momenta are barely large enough to determine the second Gegenbauer coefficient with an acceptable precision. Therefore, for the time being the Mellin moment technique described in this work is the only lattice method which is able to obtain precise results on DAs. In the future, the position-space method will complement the standard Mellin moments method.

Previous simulations lack a reliable continuum extrapolation of the lattice results due

to statistical uncertainties, see for example [42] for a recent study using $N_f = 2$ dynamical fermions. In the following sections, we will present the results of an exploratory RQCD study (recently published in [164]) which employs the mentioned momentum smearing technique in order to reduce the statistical errors also when using the Mellin moments method.

5.1.2 Continuum formulation

Neglecting both isospin breaking and electromagnetic effects, the DAs of the charged pseudoscalar $\pi^\pm$ and the neutral π^0 are trivially related such that it is sufficient to consider only one of them. The pion has one independent leading twist DA, ϕ, which is defined via a meson-to-vacuum matrix element of renormalized non-local quark-antiquark light-ray operator,

$$\begin{aligned}\langle 0|\bar{d}(z_2 n)\not{n}[z_2 n, z_1 n]\gamma_5 u(z_1 n)|\pi^+(p)\rangle &= \\ = i f_\pi p\cdot n \int_0^1 dx\, e^{-i(z_1 x + z_2(1-x))p\cdot n}\phi(x,\mu^2),&\end{aligned} \tag{5.2}$$

where $z_{1,2}$ are real numbers, n^μ is an auxiliary light-like vector with $n^2 = 0$, and $|\pi^+(p)\rangle$ represents the ground state pseudoscalar π^+ meson with on-shell momentum $p^2 = m_\pi^2$. The straight path-ordered Wilson line connecting the quark fields, $[z_2 n, z_1 n]$, is inserted to ensure gauge invariance. The scale dependence of ϕ is indicated by the argument μ^2.

The decay constant f_π appearing in eq. (5.2) can be obtained from the matrix element of a local operator,

$$\langle 0|\bar{d}(0)\gamma_0\gamma_5 u(0)|\pi^+(p)\rangle = i f_\pi p_0\,, \tag{5.3}$$

and has the value $f_\pi \approx 130\,\text{MeV}$ [165].

The physical interpretation of eq. (5.2) is that the fraction x of the pion momentum is carried by the u quark, while the $\bar{d}$ antiquark carries the remaining fraction $1 - x$. Hence the difference of the momentum fractions,

$$\xi = x - (1-x) = 2x - 1\,, \tag{5.4}$$

is the only relevant parameter. Consequently, the Mellin moments,

$$\langle \xi^n \rangle = \int_0^1 dx\,(2x-1)^n \phi(x,\mu^2)\,, \tag{5.5}$$

contain all non-trivial information on the pion DA. As we assume isospin symmetry and

neglect electromagnetic effects, the pion DA is symmetric under the interchange $x \leftrightarrow 1-x$,

$$\phi(x,\mu^2) = \phi(1-x,\mu^2)\,, \tag{5.6}$$

such that all odd moments $\langle \xi^{2n+1} \rangle$ vanish.

Since the Gegenbauer polynomials $C_n^{3/2}(2x-1)$, which correspond to irreducible representations of the collinear conformal group $\mathrm{SL}(2,\mathbb{R})$, form a complete set of functions, the DAs can be expanded as

$$\phi(x,\mu^2) = 6x(1-x)\left[1 + \sum_{n=1}^{\infty} a_n(\mu^2) C_n^{3/2}(2x-1)\right], \tag{5.7}$$

where the Gegenbauer moments a_n renormalize multiplicatively in leading logarithmic order. Higher-order contributions in the Gegenbauer expansion are suppressed at large scales, since the anomalous dimensions of a_n increase with n. Hence, in the limit $\mu \to \infty$ only the leading term survives, which gives the asymptotic DA:

$$\phi(x,\mu\to\infty) = \phi^{\mathrm{as}}(x) = 6x(1-x)\,. \tag{5.8}$$

5.1.3 Lattice formulation

The Mellin moments of the DAs can be expressed in terms of matrix elements of local operators and can be evaluated using lattice QCD. In order to calculate the second moment of the pion DA ($n = 2$), we define the bare operators

$$\mathcal{P}(x) = \bar{d}(x)\gamma_5 u(x)\,, \tag{5.9a}$$

$$\mathcal{A}_\rho(x) = \bar{d}(x)\gamma_\rho\gamma_5 u(x)\,, \tag{5.9b}$$

$$\mathcal{O}^-_{\rho\mu\nu}(x) = \bar{d}(x)\big[\overleftarrow{D}_{(\mu}\overleftarrow{D}_\nu - 2\overleftarrow{D}_{(\mu}\overrightarrow{D}_\nu + \overrightarrow{D}_{(\mu}\overrightarrow{D}_\nu\big]\gamma_{\rho)}\gamma_5 u(x)\,, \tag{5.9c}$$

$$\mathcal{O}^+_{\rho\mu\nu}(x) = \bar{d}(x)\big[\overleftarrow{D}_{(\mu}\overleftarrow{D}_\nu + 2\overleftarrow{D}_{(\mu}\overrightarrow{D}_\nu + \overrightarrow{D}_{(\mu}\overrightarrow{D}_\nu\big]\gamma_{\rho)}\gamma_5 u(x)\,, \tag{5.9d}$$

where D_μ is the covariant derivative, which will be replaced by a symmetric discretized version on the lattice. In order to obtain a leading twist projection we symmetrize over all Lorentz indices and subtract all traces. This procedure is indicated by enclosing the indices in parentheses, for example $\mathcal{O}_{(\mu\nu)} = \frac{1}{2}(\mathcal{O}_{\mu\nu} + \mathcal{O}_{\nu\mu}) - \frac{1}{4}\delta_{\mu\nu}\mathcal{O}_{\lambda\lambda}$.

Often the shorthand notation $\overleftrightarrow{D}_\mu = \overrightarrow{D}_\mu - \overleftarrow{D}_\mu$ is used such that the operator $\mathcal{O}^-_{\rho\mu\nu}$ can be written as

$$\mathcal{O}^-_{\rho\mu\nu}(x) = \bar{d}(x)\overleftrightarrow{D}_{(\mu}\overleftrightarrow{D}_\nu\gamma_{\rho)}\gamma_5 u(x)\,. \tag{5.10}$$

The matrix element of $\mathcal{O}^-_{\rho\mu\nu}(x)$ between the vacuum and the π state is proportional to

the bare value of $\langle \xi^2 \rangle$:

$$\langle 0|\mathcal{O}^-_{\rho\mu\nu}|\pi^+(p)\rangle = \mathcal{N}^{\pi^+}_{(\rho\mu\nu)}\langle \xi^2 \rangle_{\text{bare}}\,, \tag{5.11}$$

where $\mathcal{N}^{\pi^+}_{(\rho\mu\nu)}$ is a kinematic prefactor. The operator $\mathcal{O}^+_{\rho\mu\nu}$ is, in the continuum, given by the second derivative of the axialvector current:

$$\mathcal{O}^+_{\rho\mu\nu}(x) = \partial_{(\mu}\partial_\nu \mathcal{A}_{\rho)}(x)\,, \tag{5.12}$$

which leads to the matrix element

$$\langle 0|\mathcal{O}^+_{\rho\mu\nu}|\pi^+(p)\rangle = \mathcal{N}^{\pi^+}_{(\rho\mu\nu)}\langle 1^2 \rangle_{\text{bare}}\,. \tag{5.13}$$

Possible admixtures of lower-dimensional operators can be prevented by selecting lattice operators that belong to a suitable irreducible representation of the hypercubic group H(4) [43, 166]. For our case, this corresponds to choosing all indices different for the operators $\mathcal{O}^\pm$. Identifying one index with the temporal direction, this leaves us with the operators

$$\mathcal{O}^\pm_{4jk}, \quad j,k \in \{1,2,3\},\, j \neq k\,. \tag{5.14}$$

In order to extract the desired moments we use two-point correlation functions of the operators $\mathcal{O}^\pm_{4jk}$ and $\mathcal{A}_\rho$ with an interpolating field,

$$C_\rho(t,\mathbf{p}) = a^3 \sum_{\mathbf{x}} e^{-i\mathbf{p}\mathbf{x}}\langle \mathcal{A}_\rho(\mathbf{x},t) J^\dagger(0)\rangle\,, \tag{5.15}$$

$$C^\pm_{\rho\mu\nu}(t,\mathbf{p}) = a^3 \sum_{\mathbf{x}} e^{-i\mathbf{p}\mathbf{x}}\langle \mathcal{O}^\pm_{\rho\mu\nu}(\mathbf{x},t) J^\dagger(0)\rangle\,, \tag{5.16}$$

where $J = \mathcal{P}$ or $J = \mathcal{A}_4$. For sufficiently large t, the ground state dominates and the correlation functions give

$$C_{\mathcal{O}}(t,\mathbf{p}) = \frac{1}{2E}\langle 0|\mathcal{O}(0)|\pi^+(\mathbf{p})\rangle\langle \pi^+(\mathbf{p})|J^\dagger(0)|0\rangle\Big(e^{-Et} + \tau_{\mathcal{O}}\tau_J e^{-E(T-t)}\Big)\,, \tag{5.17}$$

where the sign factors $\tau_{\mathcal{O}}, \tau_J = \pm 1$ depend on the transformation properties of the correlation functions under time reversal. Following ref. [42], the required matrix elements for the second moments can be extracted from the ratios

$$\mathcal{R}^\pm_{4ik} = \frac{C^\pm_{4ik}(t,\mathbf{p})}{C_4(t,\mathbf{p})} = -p_i p_k R^\pm\,, \tag{5.18}$$

where $R^+ = \langle 1^2 \rangle_{\text{bare}}$ and $R^- = \langle \xi^2 \rangle_{\text{bare}}$. In order to test the effects of the new smearing technique introduced in the next section it is sufficient to restrict oneself to the

interpolator $J = \mathcal{P}$. The renormalized moments in the $\overline{\text{MS}}$ scheme read

$$\langle \xi^2 \rangle^{\overline{\text{MS}}} = \zeta_{11} R^- + \zeta_{12} R^+ , \tag{5.19}$$

$$a_2^{\overline{\text{MS}}} = \frac{7}{12}\big[5\zeta_{11} R^- + (5\zeta_{12} - \zeta_{22}) R^+\big] , \tag{5.20}$$

$$\langle 1^2 \rangle^{\overline{\text{MS}}} = \zeta_{22} R^+ , \tag{5.21}$$

where ζ_{ij} are ratios of renormalization constants. Even though by construction,

$$\langle 1^2 \rangle^{\overline{\text{MS}}} = 1 \tag{5.22}$$

in the continuum, this is no longer true on the lattice because the Leibniz rule holds for discretized derivatives only up to lattice artifacts. This has to be taken into account for the calculation of the Gegenbauer moment a_2, as for finite lattice spacings a the continuum relation

$$a_2^{\overline{\text{MS}}} = \frac{7}{12}\big[5\langle \xi^2 \rangle^{\overline{\text{MS}}} - 1\big] , \tag{5.23}$$

is modified to

$$a_2^{\overline{\text{MS}}} = \frac{7}{12}\big[5\langle \xi^2 \rangle^{\overline{\text{MS}}} - \langle 1^2 \rangle^{\overline{\text{MS}}}\big] . \tag{5.24}$$

5.1.4 Simulation details and momentum smearing

On the lattice, the spatial momentum components are quantized in terms of integer multiples of $2\pi/L$. It follows from eq. (5.18), that the calculation of the second moment of the DA requires a spatial momentum $\mathbf{p} = (2\pi/L)\mathbf{n_p}$ with at least two non-vanishing components, i.e., $\mathbf{n_p}^2 \geq 2$. In addition, taking two derivatives considerably deteriorates the signal-to-noise ratio. The problem is ameliorated by using momentum smearing first introduced in [158].

Quark-smearing on the lattice is used in order to increase the overlap with the ground state. The smearing operator F should be self-adjoint, gauge covariant and a singlet with respect to all global transformations that act on a timeslice. In the non-interacting case its action on a quark field q can be expressed as a convolution with a scalar kernel function f:

$$(Fq)_{\mathbf{x}} = \sum_{\mathbf{y}} f(\mathbf{x} - \mathbf{y}) q_{\mathbf{y}} . \tag{5.25}$$

In momentum space this convolution becomes a product.

If our smearing kernel is a real Gaussian, then in momentum space it will remain a Gaussian centred around $\mathbf{q} = \mathbf{0}$ (see figure 5.3) and large hadron momenta will be strongly suppressed. If the hadron carries a non-vanishing momentum $\mathbf{p}$, it is natural to assume

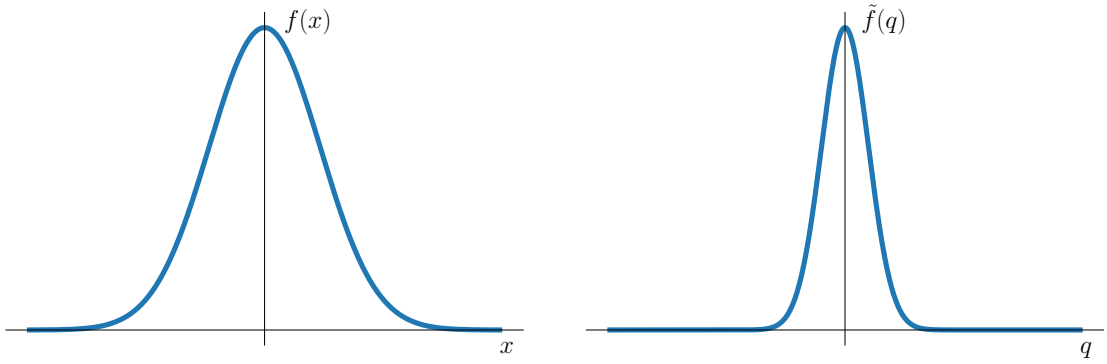

Figure 5.3: One dimensional (not to scale) illustration of the Wuppertal smearing process: A Gaussian smearing kernel $f(x) \propto \exp(-\frac{x^2}{2\sigma^2})$ in position-space corresponds to a Gaussian distribution $\tilde{f}(q) \propto \exp(-\frac{\sigma^2 q^2}{2})$ in momentum space.

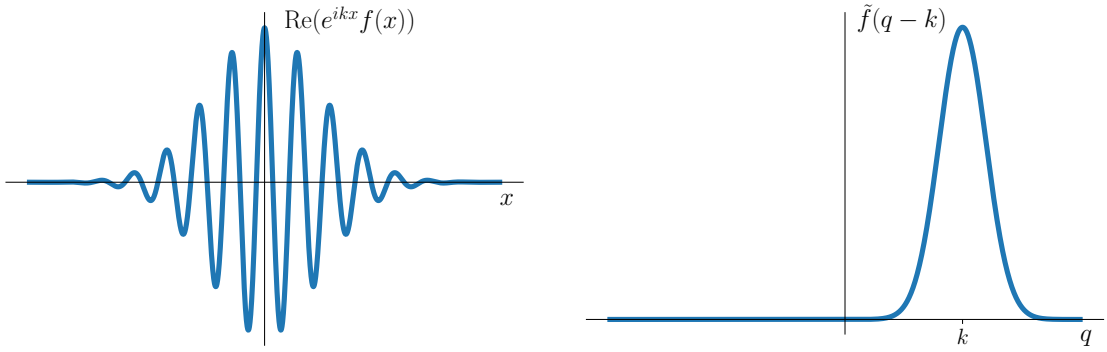

Figure 5.4: One dimensional (not to scale) illustration of the momentum smearing process: By introducing the phase factor $\exp(ikx)$ in position-space, the smearing kernel in momentum space is shifted, $\tilde{f}(q) \to \tilde{f}(q-k)$, such that the resulting Gaussian is now centered around the non-zero momentum k.

that the quark will carry a momentum fraction $\mathbf{k} = \zeta\mathbf{p}$. Therefore, a better overlap with the state can be expected if the Gaussian in momentum space is centered around $\mathbf{q} = \mathbf{k}$ instead of $\mathbf{q} = \mathbf{0}$. Within the momentum smearing approach, this is achieved by multiplying a phase factor to the smearing kernel in position-space, see figure 5.4. We remark that there is no obvious relation between ζ and the longitudinal momentum fraction x of the light-cone wave function. The modified Gaussian wave function with width σ has the form

$$f_{(\mathbf{k})}(\mathbf{x}-\mathbf{y}) = f_{(\mathbf{0})}(\mathbf{0}) \exp\left[-\frac{(\mathbf{x}-\mathbf{y})^2}{2\sigma^2} + i\mathbf{k}(\mathbf{x}-\mathbf{y})\right], \tag{5.26}$$

where $f_{(\mathbf{0})} = f$. Our periodic lattice appears to imply a quantization of the possible values of $\mathbf{k}$. However, eq. (5.26) can also be cast into an iterative process, lifting this limitation. In an infinite volume, the above convolution $F_{(\mathbf{k})}q$ can be obtained as the result of evolving

the heat equation with a drift term,

$$\frac{\partial q(\tau)}{\partial \tau} = \alpha(\nabla - i\mathbf{k})^2 q(\tau)\,, \tag{5.27}$$

starting from a spatial delta source at $\tau = 0$, to the fictitious time $\tau = \sigma^2/(2\alpha)$.

One can approximate eq. (5.27) by a discrete process, defining $F_{(\mathbf{k})} = \Phi^n_{(\mathbf{k})}$ as the nth application of an elementary iteration,

$$(\Phi_{(\mathbf{k})} q)_{\mathbf{x}} = \frac{1}{1+6\varepsilon}\left[q_{\mathbf{x}} + \varepsilon \sum_{j=\pm 1}^{\pm 3} U_{\mathbf{x},j} e^{-i\mathbf{k}\hat{\mathbf{j}}} q_{\mathbf{x}+\hat{\mathbf{j}}} \right], \tag{5.28}$$

where $U_{\mathbf{x},j}$ is the gauge link connecting the lattice points $\mathbf{x}$ and $\mathbf{x}+\hat{\mathbf{j}}$, for details see refs. [83, 158]. In practice this smearing is implemented by multiplying the spatial connectors within the timeslice in question by the appropriate phases, $U_{\mathbf{x},j} \mapsto e^{-iak_j} U_{\mathbf{x},j}$. For $\mathbf{k} = \mathbf{0}$ eq. (5.28) corresponds to the well-known Wuppertal smearing [92, 167]. The time coordinate is suppressed as the smearing is local in time.

The gauge connectors within eq. (5.28), $U_{\mathbf{x},j}$ and $U_{\mathbf{x},-j} \equiv U^\dagger_{\mathbf{x}-\hat{\mathbf{j}},j}$, are spatially APE-smeared [93]:

$$U^{(m+1)}_{\mathbf{x},i} = \mathcal{P}_{\mathrm{SU}(3)}\left(\delta\, U^{(m)}_{\mathbf{x},i} + \sum_{|j|\neq i} U^{(m)}_{\mathbf{x},i} U^{(m)}_{\mathbf{x}+\hat{\mathbf{j}},i} U^{(m)\dagger}_{\mathbf{x}+\hat{\mathbf{i}},j} \right), \tag{5.29}$$

where the sum runs over the four spatial staples that surround $U_{\mathbf{x},i}$ with $i \in \{1,2,3\}$ and $j \in \{\pm 1, \pm 2, \pm 3\}$. The gauge-covariant projector $\mathcal{P}_{\mathrm{SU}(3)}$ projects onto the gauge group $\mathrm{SU}(3)$ by maximizing $\mathrm{Re}\,\mathrm{Tr}\{A^\dagger \mathcal{P}_{\mathrm{SU}(3)}(A)\}$. If the APE smeared links are close to unit fields then the width parameter of the resulting Gaussian is given by [158]

$$\sigma \approx \sqrt{2na^2}\sqrt{\frac{\varepsilon}{1+6\varepsilon}}\,, \tag{5.30}$$

where large values of ε will allow for smaller iteration counts n, but the resulting function will be less smooth.

In the meson case the quark creation operator at the source needs to be smeared with $F_{(\mathbf{k})}$ and the quark destruction operator with $F_{(-\mathbf{k})}$, while for baryons all three quarks should be smeared with $F_{(\mathbf{k})}$, see ref. [158] for details.

We illustrate the reduction of statistical errors for the two-point functions that enter the calculation of the second moment of the pion DA when using the momentum smearing technique instead of the standard Wuppertal smearing. For this purpose we consider the CLS ensembles introduced in table 3.1. The statistical errors were evaluated using the bootstrap procedure combined with the binning method, where blocks of N_{bin} consecutive configurations are randomly chosen. We have observed that a binsize of $N_{\mathrm{bin}} = 10$ saturates

the statistical error.

The gauge links entering the quark smearing were APE smeared according to eq. (5.29), employing 25 iterations with the parameter $\delta = 2.5$. We applied both, the standard Wuppertal smearing [92, 167] and the novel momentum smearing, i.e., we implemented eq. (5.28) setting $\mathbf{k} = \mathbf{0}$ and $\mathbf{k} \neq \mathbf{0}$, respectively, and applied 300 smearing steps with the smearing parameter $\varepsilon = 0.25$. The root mean squared width of the squared pion interpolator wave function can be estimated using eq. (5.30). This gives $\sqrt{3}\sigma \approx \sqrt{3} \cdot 0.664\,\text{fm} \approx 1.14\,\text{fm}$. After studying the improvement achieved through momentum smearing, we attempt a chiral extrapolation of our results at a fixed lattice spacing $a \approx 0.0857\,\text{fm}$.

5.1.5 Optimizing the smearing and the momentum

In order to obtain the second moment of the pion DA we compute ratios of two-point functions that are smeared at the source and local at the sink (smeared-point), where the physical momenta $\mathbf{p}$ and smearing vectors $\mathbf{k}$ are parallel:

$$\mathbf{k} = \zeta \mathbf{p}. \tag{5.31}$$

One may naively expect that a value $\zeta \lesssim 1/2$ is optimal, as this would distribute the meson momentum evenly between quark and antiquark. However, ref. [158] indicated that a value $\zeta \approx 0.8$ was preferable. We confirm that by decreasing ζ from 0.8 to 0.6, no discernable improvement of the ground state overlap can be observed, see figure 5.5 for the example of the ratio R^-. If at all, the statistical errors become slightly larger. In the following we therefore stick to the suggested value of $\zeta = 0.8$.

Using the momentum smearing for mesons, one needs two inversions per momentum vector $\mathbf{n_p}$. In contrast to baryonic two-point functions, where all quarks propagate in the forward direction and therefore are smeared using $f_{(\mathbf{k})}$, the antiquark in mesonic two-point functions needs to be smeared with $f_{(-\mathbf{k})}$. It is instructive to determine which momentum vector $\mathbf{n_p}$ produces the best signal for a given ensemble. We make a crude approximation for the signal-to-noise ratio $S(t)$ by assuming a time-independent noise function. Then the signal-to-noise ratio of the numerator (which dominates the error of the combination eq. (5.18)) can be estimated as

$$S(t) \propto p_i p_j \exp\left(-\sqrt{m_\pi^2 + \mathbf{p}^2}\, t\right). \tag{5.32}$$

Maximizing this expression with respect to $\mathbf{p}^2$ gives the positive solution

$$\mathbf{p}^2 = \frac{2}{t^2}\left(1 + \sqrt{1 + m_\pi^2 t^2}\right). \tag{5.33}$$

Clearly, the optimal choice of momentum for a given correlation function depends on t

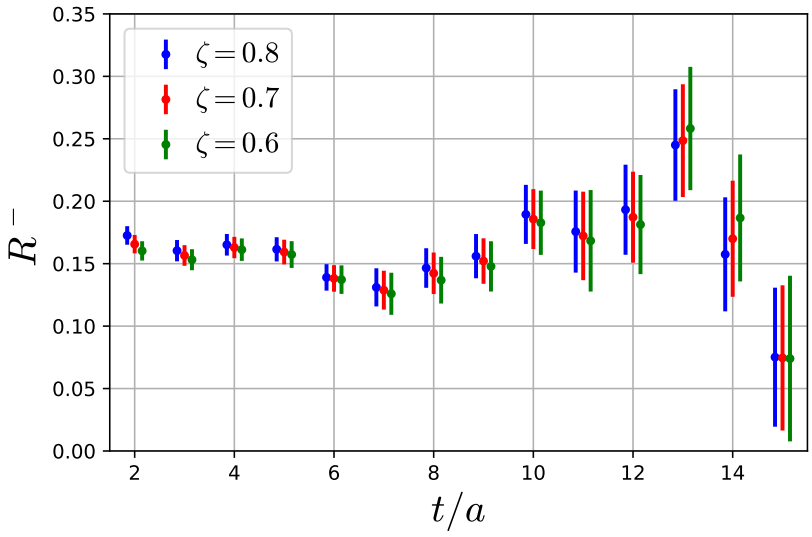

Figure 5.5: Comparison of different values for the parameter ζ, using the bare lattice value of R^- (see eq. (5.18)) at the squared momentum $\mathbf{p}^2 = 2(2\pi/L)^2 \approx (0.64\,\mathrm{GeV})^2$ obtained from 331 configurations of the ensemble H105.

and lower momenta will always be preferred at large values of t. This means the outcome will depend on the fit window in t and this in turn will depend on the available statistics. To find the most appropriate momentum, we plot eq. (5.33) in figure 5.8 for the typical fit range for our different ensembles, $4 \leq t/a \leq 12$. Based on this model, we can read off that for the $L = 32a$ lattices squared momenta in the vicinity of $\mathbf{n}_\mathbf{p}^2 = 2$ should give reasonable results, whereas for the larger $L = 48a$ lattice values of $\mathbf{n}_\mathbf{p}^2$ closer to 5 should be investigated. As an example, in figure 5.6 we show the results of the bare observables $R^\pm$ calculated for different momenta $\mathbf{p}$ on the $L = 48a$ C101 ensemble. For small values of t/a, larger $\mathbf{p}^2$ exhibit smaller statistical errors, whereas for large values of t/a, the error increases with $\mathbf{p}^2$. Thus there is a window for an optimal choice of momentum. In our further analysis we choose $\mathbf{n}_\mathbf{p} = (1,1,0)$, $\mathbf{n}_\mathbf{p} = (1,0,1)$ and $\mathbf{n}_\mathbf{p} = (0,1,1)$ for the ensembles with a spatial extent of $L = 32a$ and $\mathbf{n}_\mathbf{p} = (2,1,0)$, $\mathbf{n}_\mathbf{p} = (2,0,1)$ and $\mathbf{n}_\mathbf{p} = (0,2,1)$ for the C101 ensemble. For the $L = 32a$ lattices we employ a single source position, while for C101 we realize on average 2 source positions on each configuration.

5.1.6 Momentum smearing versus Wuppertal smearing

As a direct comparison, figure 5.7 shows the plateau of R^+ (left) and R^- (right) for the H105 lattice with $N_c = 2830$ for both smearing methods. Clearly the momentum smearing generates a much cleaner and longer plateau with very small statistical errors. In contrast to the standard Wuppertal smearing, where errors increase rapidly for high values of t, the signal-to-noise problem is less severe for the momentum smearing. Moreover, in some

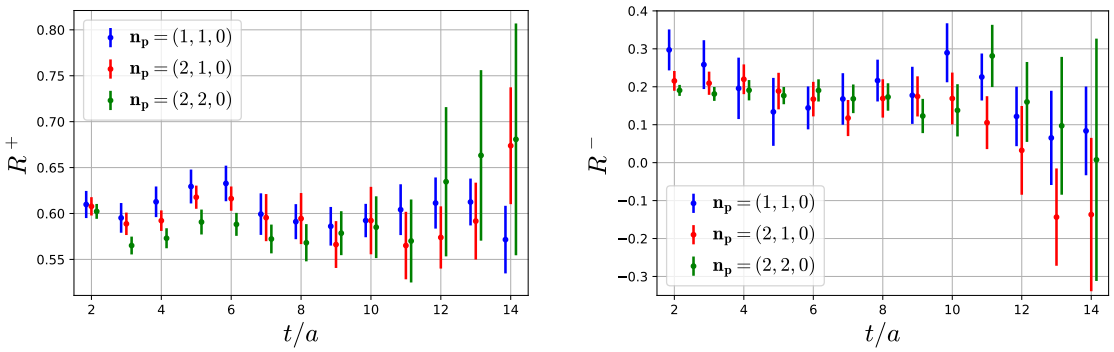

Figure 5.6: Value of $R^{\pm}$ for C101 (m_π = 222 MeV) with different momenta $\mathbf{p}$ using 52 configurations.

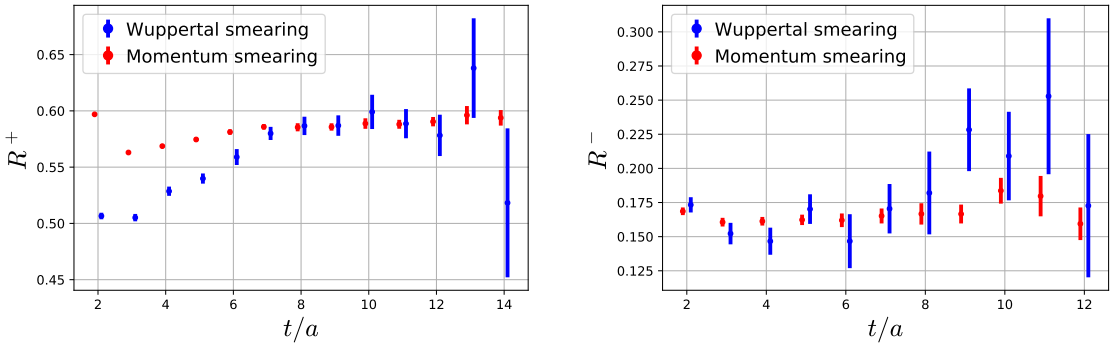

Figure 5.7: Comparison of the bare lattice values of R^- for H105 (m_π = 280 MeV) using the standard Wuppertal smearing and the new momentum smearing techniques.

cases, such as R^+ (shown in figure 5.7), we notice reduced contaminations from excited states.

In figure 5.7 we compared the results for the same number of configurations. However, the novel momentum smearing method is computationally more expensive. In general one can average over momenta that are equivalent in terms of the cubic symmetry group. Taking into account that the results for $\mathbf{p}$ and $-\mathbf{p}$ are trivially related, this gives, depending on the momentum, up to 12 possible lattice directions. For the Wuppertal smearing, additional momenta are computationally almost for free, as they only require additional Fourier sums. In contrast, for the momentum smearing each momentum direction requires new, differently smeared sources. For the pion two inversions, with momenta $\mathbf{k}$ and $-\mathbf{k}$, are necessary as discussed in section 5.1.4. For $\mathbf{n}_\mathbf{p}^2 = 2$ this means that momentum smearing is by a factor of almost 6 more expensive than Wuppertal smearing for a given configuration. In table 5.1 we provide an equal cost comparison of the ratios of errors obtained using both methods for the H105 lattice. Even at equal cost, we still see a reduction of the squared

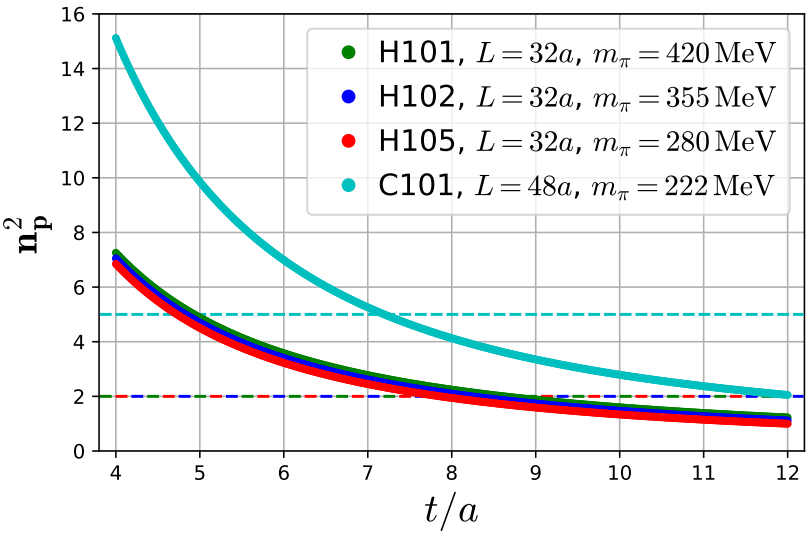

Figure 5.8: The optimal $\mathbf{n}_\mathbf{p}^2$, according to the model eq. (5.33), as a function of t/a for each ensemble.

error by up to a factor 3, in particular for the physically more relevant R^- ratio. Note that for R^+, this factor is around 1 for small t/a, but grows after the ground state plateau is reached for $t > 7a$. The reduction in error is not only a local effect on individual timeslices, it persists also when performing a fully correlated fit in the plateau region. For a fixed number of measurements the gain of momentum smearing is even larger than at a fixed computational cost. However, the reduction of errors that can be achieved by increasing the number of measurements on each configuration is limited, as additional measurements will become increasingly correlated. One could also argue that the computational cost of the generation of configurations can be decreased by momentum smearing, as fewer configurations have to be generated in order to achieve a certain statistical precision. In general, however, this is not true since observables plagued by long autocorrelation times require a large number of Monte Carlo updates anyway.

Note that for mesons containing non-degenerate quarks, the traditional method becomes more expensive as this will also require two inversions, while for baryon interpolators no momentum smearing with $-\mathbf{k}$ is required. This means that in terms of a real cost comparison the pion is the least favorable case for momentum smearing.

5.1.7 Chiral extrapolation

We use ChPT to extrapolate the results obtained with the new momentum smearing to physical quark masses. Up to one-loop order, $\langle \xi^2 \rangle^{\overline{\mathrm{MS}}}$ and $a_2^{\overline{\mathrm{MS}}}$ do not contain chiral

t/a	3	4	5	6	7	8	9	10	11	12
R^-	1.01	1.64	1.35	2.60	1.82	2.51	3.20	1.96	2.48	3.21
R^+	0.85	0.97	1.03	1.64	1.03	0.85	1.28	1.76	1.77	3.24

Table 5.1: Equal cost comparison of the errors obtained with both methods on the H105 lattice for $R^{\pm}$. We show the squared ratio of the statistical errors of Wuppertal smearing over momentum smearing divided by the number of inversions needed for each method.

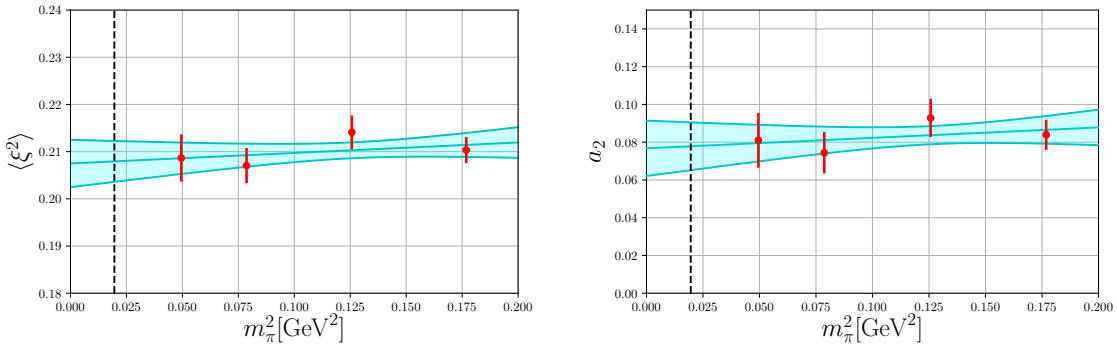

Figure 5.9: Mean and one standard deviation error bands of the chiral extrapolation of $\langle \xi^2 \rangle$ (left) and a_2 (right). The vertical dotted line indicates the physical pion mass.

logarithms [168], which yields a linear behavior in m_π^2,

$$\langle \xi^2 \rangle = \langle \xi^2 \rangle^{(0)} + \langle \xi^2 \rangle^{(2)} m_\pi^2 \,, \tag{5.34}$$

$$a_2 = a_2^{(0)} + a_2^{(2)} m_\pi^2 \,, \tag{5.35}$$

where $\langle \xi^2 \rangle^{(n)}$ are LECs of the fit. Higher order corrections would start at $\mathcal{O}(m_\pi^4)$ and are not considered here. The chiral extrapolation is depicted in figure 5.9. At the physical point we find

$$\langle \xi^2 \rangle^{\overline{\text{MS}}}(2\text{ GeV}) = 0.2077(43) \,, \tag{5.36}$$

$$a_2^{\overline{\text{MS}}}(2\text{ GeV}) = 0.0762(127) \,. \tag{5.37}$$

These numbers were obtained at the fixed lattice spacing $a \approx 0.0857$ fm and no continuum limit has been performed yet.

Note that by inserting eq. (5.36) into eq. (5.23), one obtains

$$\begin{aligned} a_2^{\overline{\mathrm{MS}}} &= \frac{7}{12}\left[5\langle\xi^2\rangle^{\overline{\mathrm{MS}}} - 1\right] \\ &= \frac{7}{12}\left[5 \cdot 0.2077 - 1\right] \\ &\approx 0.0225 \neq 0.0762\,, \end{aligned} \tag{5.38}$$

in contradiction to the obtained results for a_2 in eq. (5.37). However, due to the effects of the finite lattice spacing a, one has to use eq. (5.24) instead of eq. (5.23). Thus we also extrapolate $\langle 1^2\rangle^{\overline{\mathrm{MS}}}$ linear in m_π^2 to obtain

$$\langle 1^2\rangle^{\overline{\mathrm{MS}}}(2\ \mathrm{GeV}) = 0.905(3)\,. \tag{5.39}$$

Finally, inserting eq. (5.39) and eq. (5.36) into eq. (5.24) gives

$$\begin{aligned} a_2^{\overline{\mathrm{MS}}} &= \frac{7}{12}\left[5\langle\xi^2\rangle^{\overline{\mathrm{MS}}} - \langle 1^2\rangle^{\overline{\mathrm{MS}}}\right] \\ &= \frac{7}{12}\left[5 \cdot 0.2077 - 0.905\right] \\ &\approx 0.0779\,, \end{aligned} \tag{5.40}$$

which agrees well with eq. (5.37). This also shows that a_2 is a much more sensitive quantity than $\langle\xi^2\rangle$.

5.1.8 Summary and outlook

In the previous sections we have demonstrated the capabilities and advantages of the momentum smearing technique by comparing it to the standard Wuppertal smearing. It is important to note that we obtained smaller errors with a similar computational effort even though we performed this comparison for the example of the pion, where the momentum smearing requires an additional inversion compared to the Wuppertal smearing. Thus, the gain of the method is even higher for mesons like the kaon where already two inversions are required for the Wuppertal smearing. In total, the momentum smearing proves to be especially useful if only a fixed number of configurations is available, as it yields smaller statistical errors than other techniques. As a next step, we will apply this technique to the whole meson octet on multiple CLS lattices, including ensembles at (nearly) physical quark masses and various lattice spacings down to $a \approx 0.04$ fm. This will expand our previous work on the pion DA [42] and allow us to perform a combined chiral and continuum extrapolation.

5.2 Rho-meson distribution amplitudes

5.2.1 Overview

The DAs of the ρ-meson are essential in describing processes like the radiative $B \to \rho\gamma$ [169] or the semileptonic $B \to \rho l\nu$ decays [170]. The interest in these decays arose due to the possibility to extract Cabibbo–Kobayashi–Maskawa (CKM) matrix elements, in this case $|V_{ub}|$ and $|V_{td}/V_{ts}|$, as well as the sensitivity of B meson decays to physics beyond the Standard Model [171]. Other applications are deeply-virtual exclusive meson production (DVMP) like the electron-nucleon collision $eN \to e\rho N$, which allows to probe the transverse distribution of partons inside the nucleon, as well as deeply-virtual Compton scattering (DVCS), see [172]. The ρ DA can then be used within global fits of generalized parton distributions from the DVMP and DVCS data [173].

In the following sections we will present a lattice calculation of the coupling constants and the second moments of the ρ DA, which has been published in [97]. The analysis runs of this work were performed on the ensembles introduced in section 3.3.4, which feature pion masses down to $m_\pi = 150$ MeV. In the real world, the ρ-meson decays through strong interaction to a pair of pions, $\rho \to \pi\pi$, with a branching ratio of more than 99%. Due to the high computational costs of two-particle interpolators, we neglect the effects of this decay in this work but refer to [174], where a method to include such contributions is explained.[1]

5.2.2 Continuum formulation

In contrast to the pseudoscalar pion in section 5.1.2, the vector ρ-meson has two independent leading twist (twist two) DAs, $\phi_\rho^\parallel$ and $\phi_\rho^\perp$ [25], corresponding to longitudinal and transverse polarization, respectively. By neglecting isospin breaking and electromagnetic effects, the DAs of charged $\rho^\pm$ and neutral ρ^0 mesons, in a similar manner as for the pion triplet, are related such that it is sufficient to consider one of them. The corresponding meson-to-vacuum matrix elements of renormalized non-local quark-antiquark light-ray operators are given by [25, 175]

$$\begin{aligned}
&\langle 0|\bar{d}(z_2 n)\not{n}[z_2 n, z_1 n]u(z_1 n)|\rho^+(p,\lambda)\rangle \\
&\qquad = m_\rho f_\rho e^{(\lambda)}\cdot n \int_0^1 dx\, e^{-ip\cdot n(z_1 x + z_2(1-x))}\phi_\rho^\parallel(x,\mu)\,, \qquad (5.41a)\\
&e_{\perp,\mu}^{(\lambda')} n_\nu \langle 0|\bar{d}(z_2 n)\sigma^{\mu\nu}[z_2 n, z_1 n]u(z_1 n)|\rho^+(p,\lambda)\rangle \\
&\qquad = i f_\rho^T \big(e_\perp^{(\lambda')}\cdot e_\perp^{(\lambda)}\big) p\cdot n \int_0^1 dx\, e^{-ip\cdot n(z_1 x + z_2(1-x))}\phi_\rho^\perp(x,\mu)\,, \qquad (5.41b)
\end{aligned}$$

[1] A posteriori, our approximation can at least be partly justified by the fact that the final results are not influenced significantly when including the ensemble below the decay threshold, see also the discussion in section 5.2.9.

where again $z_{1,2}$ are real numbers, n is an auxiliary light-like vector ($n^2 = 0$), and $|\rho^+(p,\lambda)\rangle$ is the state of the ρ^+ meson with on-shell momentum $p^2 = m_\rho^2$ and polarization λ. The polarization vector $e_\mu^{(\lambda)}$ of the ρ-meson fulfills

$$e^{(\lambda)} \cdot p = 0\,, \qquad \sum_\lambda e_\mu^{(\lambda)} e_\nu^{(\lambda)*} = -g_{\mu\nu} + \frac{p_\mu p_\nu}{m_\rho^2}\,, \tag{5.42}$$

with the projection

$$e_{\perp,\mu}^{(\lambda)} = g_{\mu\nu}^\perp e^{(\lambda)\,\nu}\,. \tag{5.43}$$

Similar to the pseudoscalar case, x corresponds to the fraction of the ρ^+-meson's light-cone momentum $p\cdot n$ which is carried by the u-quark, whereas $1-x$ is the momentum fraction carried by the antiquark $\bar{d}$. The couplings f_ρ and f_ρ^T appearing in (5.41) are defined as matrix elements of local operators:

$$\langle 0|\bar{d}(0)\gamma_\mu u(0)|\rho^+(p,\lambda)\rangle = f_\rho m_\rho e_\mu^{(\lambda)}\,, \tag{5.44a}$$

$$\langle 0|\bar{d}(0)\sigma_{\mu\nu} u(0)|\rho^+(p,\lambda)\rangle = i f_\rho^T \big(e_\mu^{(\lambda)} p_\nu - e_\nu^{(\lambda)} p_\mu\big)\,. \tag{5.44b}$$

In the following, we will refer to them as vector and tensor couplings, respectively. The vector coupling f_ρ is scale independent and can be extracted from experiment, see appendix C in ref. [176] for a detailed discussion. One obtains [176]

$$f_{\rho^+} = (210 \pm 4)\ \text{MeV}\,, \qquad f_{\rho^0}^{(u)} = (221.5 \pm 3)\ \text{MeV}\,, \qquad f_{\rho^0}^{(d)} = (209.7 \pm 3)\ \text{MeV}\,, \tag{5.45}$$

where for the neutral ρ-meson we quote separate values for the $\bar{u}u$ and $\bar{d}d$ currents. The difference in the given three values is due to isospin breaking and electromagnetic corrections, which will be neglected throughout this study.

The tensor coupling f_ρ^T is scale dependent and is not directly accessible from experiment. To leading order one obtains

$$f_\rho^T(\mu) = f_\rho^T(\mu_0)\left(\frac{\alpha_s(\mu)}{\alpha_s(\mu_0)}\right)^{C_F/\beta_0}\,, \tag{5.46}$$

where $C_F = (N_{\text{color}}^2 - 1)/(2N_{\text{color}})$, $\beta_0 = (11 N_{\text{color}} - 2N_f)/3$, $N_{\text{color}} = 3$ is the number of colors and N_f the number of active flavors. The definitions (5.44) correspond to DAs that are normalized to unity,

$$\int_0^1 dx\, \phi_\rho^{\parallel,\perp}(x) = 1\,, \tag{5.47}$$

and, as for the pion DA, we introduce the variable $\xi = 2x - 1$, which corresponds to the

difference of the momentum fractions of quark and antiquark. We define the corresponding Mellin moments

$$\langle \xi^n \rangle^{\parallel,\perp} = \int_0^1 dx\, (2x-1)^n\, \phi_\rho^{\parallel,\perp}(x)\ , \qquad n = 2,4,6,\dots\ , \tag{5.48}$$

which can be related algebraically to the Gegenbauer moments. We are again interested in the first non-vanishing case, $n = 2$. The second Gegenbauer moment is given by

$$a_2^{\parallel,\perp} = \frac{7}{12}\big(5\langle \xi^2 \rangle^{\parallel,\perp} - 1\big)\,. \tag{5.49}$$

The rationale for using Gegenbauer moments is that they are eigenfunctions of the one-loop evolution equation and therefore show autonomous scale dependence at the one-loop level, see [97]. Similar to eq. (5.7) for the pion, we expand the DAs of the ρ-meson and obtain

$$\phi_\rho^{\parallel,\perp}(x,\mu) = 6x(1-x)\left[1 + \sum_{n=2,4,\dots}^{\infty} a_n^{\parallel,\perp}(\mu) C_n^{3/2}(2x-1)\right]. \tag{5.50}$$

The asymptotic DA is again obtained in the limit $\mu \to \infty$:

$$\phi_\rho^{\parallel,\perp}(x,\mu\to\infty) = \phi_{\text{as}}(x) = 6x(1-x)\,. \tag{5.51}$$

5.2.3 Lattice formulation

As already mentioned, our aim is to calculate the couplings f_ρ and f_ρ^T as well as the second DA moments. To this end we define bare operators

$$V_\mu(x) = \bar{d}(x)\gamma_\mu u(x)\,, \tag{5.52a}$$

$$T_{\mu\nu}(x) = \bar{d}(x)\sigma_{\mu\nu} u(x)\,, \tag{5.52b}$$

and

$$V^{\pm}_{\mu\nu\rho}(x) = \bar{d}(x)\gamma_\mu\big(\overleftarrow{D}_\nu\overleftarrow{D}_\rho \pm 2\overleftarrow{D}_\nu\overrightarrow{D}_\rho + \overrightarrow{D}_\nu\overrightarrow{D}_\rho\big)u(x)\,, \tag{5.53a}$$

$$T^{\pm}_{\mu\nu\rho\sigma}(x) = \bar{d}(x)\sigma_{\mu\nu}\big(\overleftarrow{D}_\rho\overleftarrow{D}_\sigma \pm 2\overleftarrow{D}_\rho\overrightarrow{D}_\sigma + \overrightarrow{D}_\rho\overrightarrow{D}_\sigma\big)u(x)\,. \tag{5.53b}$$

As in section 5.1.3, the projection onto leading twist corresponds to symmetrization over the maximal possible set of Lorentz indices and subtraction of traces. However, the DAs of the ρ involve operators containing the $\sigma_{\mu\nu}$-matrix. In this case, also those traces have to be subtracted which correspond to index pairs where one of the indices equals μ or ν. The operator $V^-_{(\mu\nu\rho)}(x)$ can be rewritten as

$$V^-_{(\mu\nu\rho)}(x) = \bar{d}(x)\gamma_{(\mu}\overleftrightarrow{D}_\nu\overleftrightarrow{D}_{\rho)}u(x) \tag{5.54}$$

and its matrix element between the vacuum and the ρ state is proportional to the bare value of the second moment $\langle\xi^2\rangle^{\parallel}$:

$$\langle 0|V^-_{(\mu\nu\rho)}|\rho^+(p,\lambda)\rangle = \mathcal{N}^{\rho^+}_{(\mu\nu\rho)}\langle\xi^2\rangle^{\parallel}_{\text{bare}}\,, \tag{5.55}$$

where $\mathcal{N}^{\rho^+}_{(\mu\nu\rho)}$ is again a kinematic prefactor. The operator $V^+_{(\mu\nu\rho)}(x)$ in the continuum reduces to the second derivative of the vector current,

$$V^+_{(\mu\nu\rho)}(x) = \partial_{(\mu}\partial_\nu\bar{d}(x)\gamma_{\rho)}u(x)\,, \tag{5.56}$$

so that

$$\langle 0|V^+_{(\mu\nu\rho)}|\rho^+(p,\lambda)\rangle = \mathcal{N}^{\rho^+}_{(\mu\nu\rho)}\langle 1^2\rangle^{\parallel}_{\text{bare}}\,. \tag{5.57}$$

The situation with the tensor operators $T^{\pm}_{\mu(\nu\rho\sigma)}$ and the corresponding matrix elements $\langle\cdots\rangle^{\perp}$ is similar. For the bare moments, we use the same notation as for the pion DA and define

$$R^{\parallel,\perp}_{+} = \langle 1^2\rangle^{\parallel,\perp}_{\text{bare}}\,, \tag{5.58a}$$
$$R^{\parallel,\perp}_{-} = \langle\xi^2\rangle^{\parallel,\perp}_{\text{bare}}\,. \tag{5.58b}$$

The operators $V^-_{(\mu\nu\rho)}$ and $V^+_{(\mu\nu\rho)}$ mix under renormalization even in the continuum, as do $T^-_{\mu(\nu\rho\sigma)}$ and $T^+_{\mu(\nu\rho\sigma)}$. Additional mixing could result from the fact that the continuous $O(4)$ symmetry of Euclidean space is reduced to the discrete $H(4)$ symmetry of the hypercubic lattice. This is particularly worrisome if operators of lower dimension are involved. Fortunately, in the case at hand it is possible to avoid additional mixing by using suitably chosen operators, which will be detailed in section 5.2.6.

5.2.4 Lattice correlation functions

In order to "create" the ρ-meson we use the interpolating current $\mathcal{V}_\nu(x)$, which is defined as $V_\nu(x)$ with smeared quark fields. In this section, quark smearing refers to the standard Wuppertal smearing, i.e., the momentum smearing in the limit $\mathbf{k}\to\mathbf{0}$, see section 5.1.4.[2] Let $\mathcal{O}$ be a local (unsmeared) operator, e.g., one of the operators defined in eqs. (5.53) above. One then obtains for the two-point function in the region where the ground state

[2] Momentum smearing would also help in this case but was only developed after this analysis had already started.

Γ	$\mathbb{1}$	γ_j	γ_4	$\gamma_j\gamma_5$	$\gamma_4\gamma_5$	γ_5	$\gamma_j\gamma_k$	$\gamma_j\gamma_4$
σ	1	1	−1	−1	1	−1	1	−1

Table 5.2: Sign factors σ for the different Dirac matrices Γ. Here $j, k \in \{1, 2, 3\}$ and $j \neq k$.

dominates

$$\begin{aligned} C_{\mathcal{O}}(t, \mathbf{p}) &= a^3 \sum_{\mathbf{x}} e^{-i\mathbf{p}\,\cdot\,\mathbf{x}} \langle \mathcal{O}(t, \mathbf{x}) \mathscr{V}_\nu^\dagger(0) \rangle \\ &= \frac{1}{2E} A(\mathcal{O}, \mathscr{V}_\nu \mid \mathbf{p}) \left(e^{-Et} + \sigma\, \sigma_{\mathcal{O}}\, (-1)^{n_t} e^{-E(T-t)} \right) \end{aligned} \tag{5.59}$$

with

$$A(\mathcal{O}, \mathscr{V}_\nu \mid \mathbf{p}) = \sum_\lambda \langle 0 | \mathcal{O}(0) | \rho^+(\mathbf{p}, \lambda) \rangle \langle \rho^+(\mathbf{p}, \lambda) | \mathscr{V}_\nu^\dagger(0) | 0 \rangle \,. \tag{5.60}$$

The sign factors σ are determined by the Dirac matrices in the creation operator (which is in our case always γ_ν), while $\sigma_{\mathcal{O}}$ are the analogous factors for $\mathcal{O}$ (see table 5.2), and n_t is the number of time derivatives in $\mathcal{O}$.

For the decay constants and the second DA moments of the ρ-meson we have to evaluate the following set of correlation functions:

$$\mathscr{C}_{\mu_1\nu}(t, \mathbf{p}) = a^3 \sum_{\mathbf{x}} e^{-i\mathbf{p}\,\cdot\,\mathbf{x}} \langle \mathscr{V}_{\mu_1}(t, \mathbf{x}) \mathscr{V}_\nu^\dagger(0) \rangle \,, \tag{5.61a}$$

$$C_{\mu_1\nu}(t, \mathbf{p}) = a^3 \sum_{\mathbf{x}} e^{-i\mathbf{p}\,\cdot\,\mathbf{x}} \langle V_{\mu_1}(t, \mathbf{x}) \mathscr{V}_\nu^\dagger(0) \rangle \,, \tag{5.61b}$$

$$C_{\mu_0\mu_1\nu}(t, \mathbf{p}) = a^3 \sum_{\mathbf{x}} e^{-i\mathbf{p}\,\cdot\,\mathbf{x}} \langle T_{\mu_0\mu_1}(t, \mathbf{x}) \mathscr{V}_\nu^\dagger(0) \rangle \,, \tag{5.61c}$$

$$C^\pm_{\mu_1\mu_2\mu_3\nu}(t, \mathbf{p}) = a^3 \sum_{\mathbf{x}} e^{-i\mathbf{p}\,\cdot\,\mathbf{x}} \langle V^\pm_{\mu_1\mu_2\mu_3}(t, \mathbf{x}) \mathscr{V}_\nu^\dagger(0) \rangle \,, \tag{5.61d}$$

$$C^\pm_{\mu_0\mu_1\mu_2\mu_3\nu}(t, \mathbf{p}) = a^3 \sum_{\mathbf{x}} e^{-i\mathbf{p}\,\cdot\,\mathbf{x}} \langle T^\pm_{\mu_0\mu_1\mu_2\mu_3}(t, \mathbf{x}) \mathscr{V}_\nu^\dagger(0) \rangle \,. \tag{5.61e}$$

5.2.5 Decay constants

In order to determine the leading twist couplings of the ρ-meson, we use the correlation functions

$$\mathscr{C}_{jj}(t, \mathbf{0}) = Z_\rho \frac{1}{2m_\rho} \left(e^{-m_\rho t} + e^{-m_\rho (T-t)} \right) + \dots \,, \tag{5.62a}$$

$$C_{jj}(t, \mathbf{0}) = m_\rho f_\rho \sqrt{Z_\rho} \frac{1}{2m_\rho} \left(e^{-m_\rho t} + e^{-m_\rho (T-t)} \right) + \dots \,, \tag{5.62b}$$

$$C_{4jj}(t, \mathbf{0}) = -i m_\rho f_\rho^T \sqrt{Z_\rho} \frac{1}{2m_\rho} \left(e^{-m_\rho t} - e^{-m_\rho (T-t)} \right) + \dots \,, \tag{5.62c}$$

with $j = 1, 2, 3$, assuming the dominance of the lowest one-particle state. In the actual fits we average over the forward and backward running states. In our simulations, the signal disappears in the noise well before the middle point $t = T/2$ in the time direction is reached (see figure 5.10 for an example), and the "mixing" of these two contributions is completely negligible. Therefore we work with simple exponential fits,

$$\frac{1}{3}\sum_{j=1}^{3} \hat{t}_+ \mathscr{C}_{jj}(t, \mathbf{0}) = \frac{Z_\rho}{2m_\rho} e^{-m_\rho t}\,, \tag{5.63a}$$

$$\frac{1}{3}\sum_{j=1}^{3} \hat{t}_+ C_{jj}(t, \mathbf{0}) = f_\rho \frac{\sqrt{Z_\rho}}{2} e^{-m_\rho t}\,, \tag{5.63b}$$

$$\frac{1}{3}\sum_{j=1}^{3} \hat{t}_- C_{4jj}(t, \mathbf{0}) = -i f_\rho^T \frac{\sqrt{Z_\rho}}{2} e^{-m_\rho t}\,, \tag{5.63c}$$

where the averaging operator $\hat{t}_\pm$ is defined as

$$\hat{t}_\pm C(t, \mathbf{p}) = \tfrac{1}{2}\big(C(t, \mathbf{p}) \pm C(T - t, \mathbf{p})\big)\,. \tag{5.64}$$

The decay constants f_ρ and f_ρ^T can be obtained by simultaneously fitting the correlation functions (5.63a)–(5.63c). The result for the mass is then dominated by the two smeared-local correlation functions (5.63b) and (5.63c), as they have much smaller statistical errors. However, they exhibit larger contributions from excited states so that the isolation of the ground state is less reliable. Therefore we first fit the correlator with a smeared operator at the sink, (5.63a), to extract Z_ρ and m_ρ. These values are then inserted into eqs. (5.63b) and (5.63c) in order to obtain f_ρ and f_ρ^T as well as f_ρ^T/f_ρ from a second fit. This procedure is repeated for every bootstrap sample allowing an estimation of the statistical error.

5.2.6 Second moments

Multiplets of twist-2 operators suitable for the evaluation of the second longitudinal moments consist of the operators

$$\mathcal{O}_1^\pm = V_{\{234\}}^\pm\,, \qquad \mathcal{O}_2^\pm = V_{\{134\}}^\pm\,, \qquad \mathcal{O}_3^\pm = V_{\{124\}}^\pm\,, \qquad \mathcal{O}_4^\pm = V_{\{123\}}^\pm\,. \tag{5.65}$$

Here and in the following, $\{\cdots\}$ denotes symmetrization of the enclosed n indices with an overall factor $1/n!$ included. The two multiplets $\mathcal{O}_1^+, \ldots, \mathcal{O}_4^+$ and $\mathcal{O}_1^-, \ldots, \mathcal{O}_4^-$ both transform according to the irreducible representation τ_2^4 of the hypercubic group $H(4)$ [177]. Their symmetry properties ensure that under renormalization they can only mix with each other, while mixing with additional operators of the same or lower dimension is forbidden. The amplitudes (5.60) of the 2-point functions (5.59) where $\mathcal{O}$ is one member of these multiplets

are related to the amplitudes where $\mathcal{O}$ is a component of the vector current V_μ by

$$A(\mathcal{O}_1^\pm, \mathscr{V}_\nu \mid \mathbf{p}) = -\tfrac{1}{3} R_\pm^{\parallel}\big(p_2 p_3\, A(V_4, \mathscr{V}_\nu \mid \mathbf{p}) + i p_2 E\, A(V_3, \mathscr{V}_\nu \mid \mathbf{p}) + i p_3 E\, A(V_2, \mathscr{V}_\nu \mid \mathbf{p})\big)\,, \tag{5.66a}$$

$$A(\mathcal{O}_2^\pm, \mathscr{V}_\nu \mid \mathbf{p}) = -\tfrac{1}{3} R_\pm^{\parallel}\big(p_1 p_3\, A(V_4, \mathscr{V}_\nu \mid \mathbf{p}) + i p_1 E\, A(V_3, \mathscr{V}_\nu \mid \mathbf{p}) + i p_3 E\, A(V_1, \mathscr{V}_\nu \mid \mathbf{p})\big)\,, \tag{5.66b}$$

$$A(\mathcal{O}_3^\pm, \mathscr{V}_\nu \mid \mathbf{p}) = -\tfrac{1}{3} R_\pm^{\parallel}\big(p_1 p_2\, A(V_4, \mathscr{V}_\nu \mid \mathbf{p}) + i p_2 E\, A(V_1, \mathscr{V}_\nu \mid \mathbf{p}) + i p_1 E\, A(V_2, \mathscr{V}_\nu \mid \mathbf{p})\big)\,, \tag{5.66c}$$

$$A(\mathcal{O}_4^\pm, \mathscr{V}_\nu \mid \mathbf{p}) = -\tfrac{1}{3} R_\pm^{\parallel}\big(p_1 p_2\, A(V_3, \mathscr{V}_\nu \mid \mathbf{p}) + p_1 p_3\, A(V_2, \mathscr{V}_\nu \mid \mathbf{p}) + p_2 p_3\, A(V_1, \mathscr{V}_\nu \mid \mathbf{p})\big)\,. \tag{5.66d}$$

We will try to increase the signal-to-noise ratio by considering only correlation functions with the smallest non-zero momentum in one spatial direction, which is equal to $2\pi/L$ on a lattice of spatial extent L. Therefore we exclude $\mathcal{O}_4^\pm$ from our calculation. After averaging over all suitable combinations as well as over forward and backward running states, the second longitudinal moments can be obtained from the ratio

$$\frac{1}{6}\sum_{j=1}^{3}\sum_{\substack{k=1\\k\neq j}}^{3}\frac{\hat{p}_-\hat{t}_- C^\pm_{\{4jk\}k}\big(t, \frac{2\pi}{L}\mathbf{e}_j\big)}{\hat{p}_+\hat{t}_+ C_{kk}\big(t, \frac{2\pi}{L}\mathbf{e}_j\big)} = -\frac{2\pi}{L} E \frac{1}{3} i R_\pm^{\parallel}\,, \tag{5.67}$$

where momentum averaging is accounted for by the operator $\hat{p}_\pm$:

$$\hat{p}_\pm C(t, \mathbf{p}) = \tfrac{1}{2}\big(C(t, \mathbf{p}) \pm C(t, -\mathbf{p})\big)\,. \tag{5.68}$$

In the transverse case we consider the following multiplets:

$$\mathcal{O}^\pm_{1,T} = T^\pm_{13\{32\}} + T^\pm_{23\{31\}} - T^\pm_{14\{42\}} - T^\pm_{24\{41\}}\,, \tag{5.69a}$$

$$\mathcal{O}^\pm_{2,T} = T^\pm_{12\{23\}} + T^\pm_{32\{21\}} - T^\pm_{14\{43\}} - T^\pm_{34\{41\}}\,, \tag{5.69b}$$

$$\mathcal{O}^\pm_{3,T} = T^\pm_{12\{24\}} + T^\pm_{42\{21\}} - T^\pm_{13\{34\}} - T^\pm_{43\{31\}}\,, \tag{5.69c}$$

$$\mathcal{O}^\pm_{4,T} = T^\pm_{21\{13\}} + T^\pm_{31\{12\}} - T^\pm_{24\{43\}} - T^\pm_{34\{42\}}\,, \tag{5.69d}$$

$$\mathcal{O}^\pm_{5,T} = T^\pm_{21\{14\}} + T^\pm_{41\{12\}} - T^\pm_{23\{34\}} - T^\pm_{43\{32\}}\,, \tag{5.69e}$$

$$\mathcal{O}^\pm_{6,T} = T^\pm_{31\{14\}} + T^\pm_{41\{13\}} - T^\pm_{32\{24\}} - T^\pm_{42\{23\}}\,. \tag{5.69f}$$

The two multiplets $\mathcal{O}^+_{1,T}, \ldots, \mathcal{O}^+_{6,T}$ and $\mathcal{O}^-_{1,T}, \ldots, \mathcal{O}^-_{6,T}$ both transform according to the irreducible representation $\tau_2^{(6)}$ of the hypercubic group $H(4)$. As in the case of the multiplets (5.65), mixing with additional operators of the same or lower dimension is forbidden by symmetry. The amplitudes (5.60) of the 2-point functions (5.59) where $\mathcal{O}$ is one member of the multiplets (5.69) are related to the amplitudes where $\mathcal{O}$ is a component of the tensor

current $T_{\mu\nu}$ by

$$\begin{aligned}
A(\mathcal{O}^{\pm}_{1,T}, \mathcal{V}_\nu \mid \mathbf{p}) = -R^{\perp}_{\pm}\big(&p_2p_3\, A(T_{13}, \mathcal{V}_\nu \mid \mathbf{p}) + p_1p_3\, A(T_{23}, \mathcal{V}_\nu \mid \mathbf{p}) \\
&+ ip_2E\, A(T_{41}, \mathcal{V}_\nu \mid \mathbf{p}) + ip_1E\, A(T_{42}, \mathcal{V}_\nu \mid \mathbf{p})\big)\,, \qquad (5.70a)\\
A(\mathcal{O}^{\pm}_{2,T}, \mathcal{V}_\nu \mid \mathbf{p}) = -R^{\perp}_{\pm}\big(&p_2p_3\, A(T_{12}, \mathcal{V}_\nu \mid \mathbf{p}) + p_1p_2\, A(T_{32}, \mathcal{V}_\nu \mid \mathbf{p}) \\
&+ ip_3E\, A(T_{41}, \mathcal{V}_\nu \mid \mathbf{p}) + ip_1E\, A(T_{43}, \mathcal{V}_\nu \mid \mathbf{p})\big)\,, \qquad (5.70b)\\
A(\mathcal{O}^{\pm}_{3,T}, \mathcal{V}_\nu \mid \mathbf{p}) = -R^{\perp}_{\pm}\big(&p_1p_2\, A(T_{42}, \mathcal{V}_\nu \mid \mathbf{p}) - p_1p_3\, A(T_{43}, \mathcal{V}_\nu \mid \mathbf{p}) \\
&+ ip_2E\, A(T_{12}, \mathcal{V}_\nu \mid \mathbf{p}) + ip_3E\, A(T_{31}, \mathcal{V}_\nu \mid \mathbf{p})\big)\,, \qquad (5.70c)\\
A(\mathcal{O}^{\pm}_{4,T}, \mathcal{V}_\nu \mid \mathbf{p}) = -R^{\perp}_{\pm}\big(&p_1p_3\, A(T_{21}, \mathcal{V}_\nu \mid \mathbf{p}) + p_1p_2\, A(T_{31}, \mathcal{V}_\nu \mid \mathbf{p}) \\
&+ ip_3E\, A(T_{42}, \mathcal{V}_\nu \mid \mathbf{p}) + ip_2E\, A(T_{43}, \mathcal{V}_\nu \mid \mathbf{p})\big)\,, \qquad (5.70d)\\
A(\mathcal{O}^{\pm}_{5,T}, \mathcal{V}_\nu \mid \mathbf{p}) = -R^{\perp}_{\pm}\big(&p_1p_2\, A(T_{41}, \mathcal{V}_\nu \mid \mathbf{p}) - p_2p_3\, A(T_{43}, \mathcal{V}_\nu \mid \mathbf{p}) \\
&+ ip_1E\, A(T_{21}, \mathcal{V}_\nu \mid \mathbf{p}) + ip_3E\, A(T_{32}, \mathcal{V}_\nu \mid \mathbf{p})\big)\,, \qquad (5.70e)\\
A(\mathcal{O}^{\pm}_{6,T}, \mathcal{V}_\nu \mid \mathbf{p}) = -R^{\perp}_{\pm}\big(&p_1p_3\, A(T_{41}, \mathcal{V}_\nu \mid \mathbf{p}) - p_2p_3\, A(T_{42}, \mathcal{V}_\nu \mid \mathbf{p}) \\
&+ ip_1E\, A(T_{31}, \mathcal{V}_\nu \mid \mathbf{p}) + ip_2E\, A(T_{23}, \mathcal{V}_\nu \mid \mathbf{p})\big)\,. \qquad (5.70f)
\end{aligned}$$

As in the longitudinal case, we only consider correlation functions with the smallest non-zero momentum in one spatial direction and perform averages similar to those in eq. (5.67). This leads to the following ratio for the second transverse moments:

$$\begin{aligned}
\frac{1}{6}\sum_{j=1}^{3}\sum_{\substack{l=1\\ l\neq j}}^{3}\sum_{\substack{k=1\\ k\neq j\\ k\neq l}}^{3}\Bigg(&\frac{\hat{p}_-\hat{t}_+\big(C^{\pm}_{4\{4jl\}l}\big(t, \frac{2\pi}{L}\mathbf{e}_j\big) - C^{\pm}_{k\{kjl\}l}\big(t, \frac{2\pi}{L}\mathbf{e}_j\big)\big)}{\hat{p}_+\hat{t}_-C_{4ll}\big(t, \frac{2\pi}{L}\mathbf{e}_j\big)} \\
&+ \frac{\hat{p}_+\hat{t}_-\big(C^{\pm}_{j\{j4l\}l}\big(t, \frac{2\pi}{L}\mathbf{e}_j\big) - C^{\pm}_{k\{k4l\}l}\big(t, \frac{2\pi}{L}\mathbf{e}_j\big)\big)}{\hat{p}_-\hat{t}_+C_{jll}\big(t, \frac{2\pi}{L}\mathbf{e}_j\big)}\Bigg) = -\frac{2\pi}{L}E\frac{2}{3}iR^{\perp}_{\pm}\,. \qquad (5.71)
\end{aligned}$$

5.2.7 Details of the lattice simulations

In order to increase the overall statistics we performed multiple measurements per configuration. The source positions of these measurements were selected randomly to reduce the correlations. To obtain a better overlap with the ground state we applied Wuppertal smearing [92] in the interpolating current $\mathcal{V}_\nu$ using APE smeared gauge links [93].

For the statistical analysis we generated 1000 bootstrap samples per ensemble using a binsize of 4 to further eliminate autocorrelations. For the purpose of maximizing the statistics of the second moments, we average for each bootstrap sample over all suitable combinations of 2-point functions, all possible momentum directions as well as over forward and backward running states as pointed out in eqs. (5.67) and (5.71). In order to reduce contributions from excited states the choice of the starting point of the fit range is important. As an example, figure 5.10 demonstrates that, with increasing source-sink distance, the excited states fall below the noise and plateaus of the correlation functions

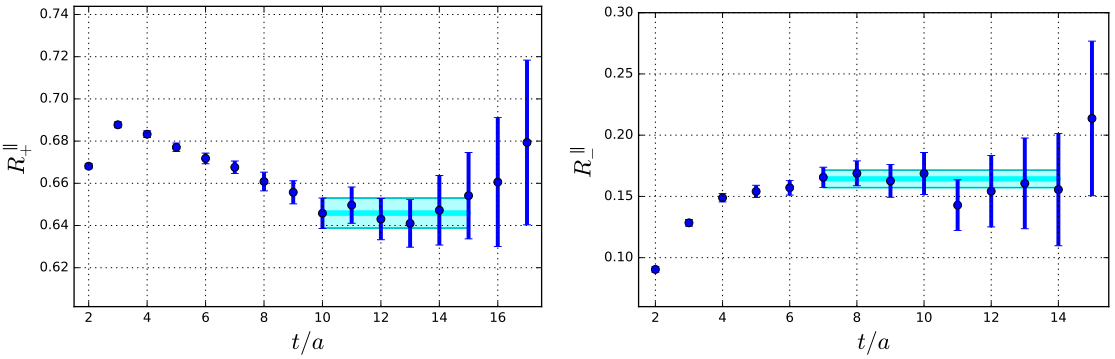

Figure 5.10: The data points in these plots show $R_{\pm}^{\parallel}$ as a function of the sink position t, calculated from the time- and momentum-averaged correlation functions according to eq. (5.67) on the $\beta = 5.29$, $\kappa = 0.13632$, $L = 32a$, $T = 64a$ ensemble, cf. table 3.2 on page 26. The cyan-colored bar indicates the fitted value of $R_{\pm}^{\parallel}$, the error and the fitting range.

for $R_{\pm}^{\parallel}$ emerge. The starting time t_{start} is then chosen in such a way that fits with even larger starting times no longer show any systematic trend in the fitted values. Multi-state fits (over larger fit ranges) yield consistent results.

5.2.8 Data analysis

Before being able to conduct a chiral extrapolation, the raw lattice data has to be renormalized. Again, we employ a non-perturbative method in an RI′/SMOM scheme and convert the results to the $\overline{\text{MS}}$ scheme using continuum perturbation theory. The full renormalization procedure is worked out explicitly in [97]. The bare operators are chosen such that there is only mixing between the + and − operator multiplets. In this way, one merely has to determine the 2×2 mixing matrices

$$\mathcal{O}^{-}_{\overline{\text{MS}}} = Z_{11}\mathcal{O}^{-} + Z_{12}\mathcal{O}^{+}\,, \tag{5.72a}$$
$$\mathcal{O}^{+}_{\overline{\text{MS}}} = Z_{22}\mathcal{O}^{+}\,, \tag{5.72b}$$

and obtains for the second moments of the DAs in the $\overline{\text{MS}}$ scheme

$$a^{\parallel,\perp}_{2,\overline{\text{MS}}} = \tfrac{7}{12}\big[5\zeta^{\parallel,\perp}_{11}R^{\parallel,\perp}_{-} + \big(5\zeta^{\parallel,\perp}_{12} - \zeta^{\parallel,\perp}_{22}\big)R^{\parallel,\perp}_{+}\big]\,, \tag{5.73}$$
$$\langle\xi^2\rangle^{\parallel,\perp}_{\overline{\text{MS}}} = \zeta^{\parallel,\perp}_{11}R^{\parallel,\perp}_{-} + \zeta^{\parallel,\perp}_{12}R^{\parallel,\perp}_{+}\,, \tag{5.74}$$
$$\langle 1^2\rangle^{\parallel,\perp}_{\overline{\text{MS}}} = \zeta^{\parallel,\perp}_{22}R^{\parallel,\perp}_{+}\,, \tag{5.75}$$

where

$$\zeta^{\parallel}_{ij} = \frac{Z^{\parallel}_{ij}}{Z_V}\,, \quad \zeta^{\perp}_{ij} = \frac{Z^{\perp}_{ij}}{Z_T}\,, \tag{5.76}$$

with the renormalization factors Z_V and Z_T of the vector and the tensor currents, respectively. Again, we will observe on the lattice that

$$\langle 1^2 \rangle^{\parallel,\perp}_{\overline{\text{MS}}} \neq 1 \,. \tag{5.77}$$

Similar to the pseudoscalar case in section 5.1.3, the Leibniz rule does not hold for finite lattice spacings and eq. (5.56) is violated by cut-off effects. We expect this relation to be recovered in the continuum, i.e.,

$$\langle 1^2 \rangle^{\parallel,\perp}_{\overline{\text{MS}}} \overset{a\to 0}{\to} 1 \,. \tag{5.78}$$

However, due to the small range of available lattice spacings, a reliable continuum extrapolation cannot be performed with the data at hand. Therefore we restrict ourselves to perform a chiral extrapolation which incorporates the renormalized results of all available lattice ensembles. Following [178–180], we obtain for the pion mass dependence of the decay constants

$$\operatorname{Re} f_\rho = f_\rho^{(0)} \left(1 - \frac{m_\pi^2}{16\pi^2 F_\pi^2} \log\left(\frac{m_\pi^2}{\mu_\chi^2} \right) \right) + f_\rho^{(2)} m_\pi^2 + f_\rho^{(3)} m_\pi^3 + \mathcal{O}(m_\pi^4) \,, \tag{5.79a}$$

$$\operatorname{Re} f_\rho^T = f_\rho^{T(0)} \left(1 - \frac{m_\pi^2}{32\pi^2 F_\pi^2} \log\left(\frac{m_\pi^2}{\mu_\chi^2} \right) \right) + f_\rho^{T(2)} m_\pi^2 + f_\rho^{T(3)} m_\pi^3 + \mathcal{O}(m_\pi^4) \,, \tag{5.79b}$$

$$\operatorname{Re} \frac{f_\rho^T}{f_\rho} = \delta f_\rho^{(0)} \left(1 + \frac{m_\pi^2}{32\pi^2 F_\pi^2} \log\left(\frac{m_\pi^2}{\mu_\chi^2} \right) \right) + \delta f_\rho^{(2)} m_\pi^2 + \delta f_\rho^{(3)} m_\pi^3 + \mathcal{O}(m_\pi^4) \,, \tag{5.79c}$$

see appendix B in [97] for details on the ChPT calculation. For $2m_\pi < m_\rho$, i.e., below the decay threshold, this infinite-volume calculation yields complex numbers. However, as we neglect instability effects in our lattice computation, which is necessarily done on finite volumes, we use only the real part to fit the mass dependence of our data. The pion decay constant $F_\pi = f_\pi/\sqrt{2} \approx 92\,\text{MeV}$ is kept fixed at its physical value, and the chiral renormalization scale μ_χ is chosen to be $m_\rho \approx 775\,\text{MeV}$.

A priori ChPT estimates, suggesting that the third-order terms in eq. (5.79) are not negligible, are confirmed by our results. In fact, it turns out that the terms $\propto m_\pi^3$ are necessary to obtain reasonable fits over the full range of pion masses. Restricting oneself to second-order approaches for ensembles with $m_\pi < 300\,\text{MeV}$ also yields consistent fits, although merely two pion masses are available in this range. For the sake of consistency we have also performed third-order polynomial fits which also yield similar results. Due to the relatively small spatial extent of the ensemble at $m_\pi = 150\,\text{MeV}$ ($m_\pi L \approx 3.4$), we expect that the full chiral extrapolation yields more reliable results than simply the values of this ensemble alone. In order to estimate the influence of the instability of the ρ we perform both fits including and excluding the results at $m_\pi = 150\,\text{MeV}$, which should contain most

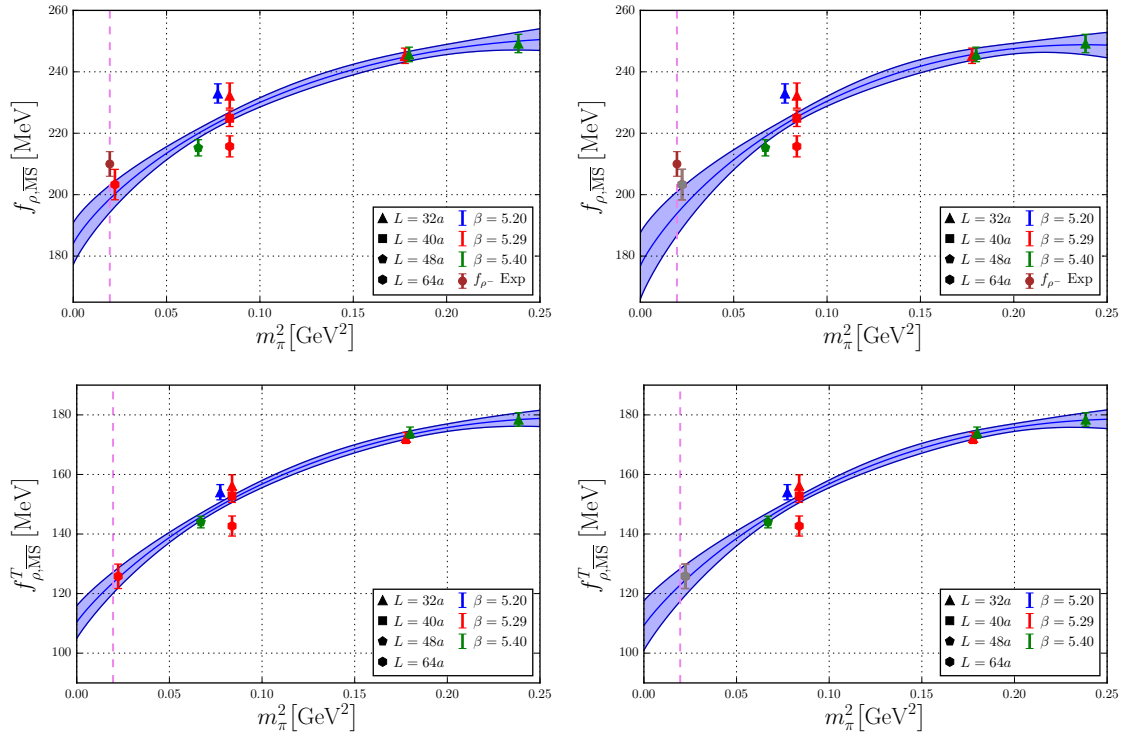

Figure 5.11: ChPT fits using eqs. (5.79) for the decay constants f_ρ, f_ρ^T, including (left) and excluding (right) the data point at $m_\pi = 150\,\mathrm{MeV}$. The violet dashed line indicates the position of the physical pion mass. The band indicates the one sigma statistical error.

effects of the $\rho \to \pi\pi$ decay. The resulting ChPT extrapolations for the normalization constants and their ratio are shown in figure 5.11 and figure 5.12, respectively. It turns out that the extrapolated values at the physical point are reasonably consistent with the data point corresponding to the lowest pion mass.

Since no ChPT calculations are available for the second moments of the ρ, we perform fits linear in m_π^2 as depicted in figure 5.13. This generic approach is based on the experience with the corresponding quantities for pseudoscalar mesons [168,181] and the nucleon [121], where no chiral logarithms appear in leading one-loop order. Within our limited set of lattice ensembles, we do not observe discernible discretization effects.

Although the available data does not allow us to study finite-size and discretization effects systematically, significant statements can still be made. With respect to finite size effects, we have ensembles with three different volumes for $\beta = 5.29$, $\kappa = 0.13632$ at our disposal ($m_\pi L = 3.4$–6.7). A closer look at figures 5.11 and 5.14 reveals that the finite-volume effects for the decay constants are sizable. Unlike the well-known cases of pseudoscalar meson and baryon masses, the chiral extrapolations cannot be converted directly to predictions for the leading large-volume behavior. The problematic contributions cancel, however, in the ratio of the decay constants f_ρ^T/f_ρ, so that it is straightforward to

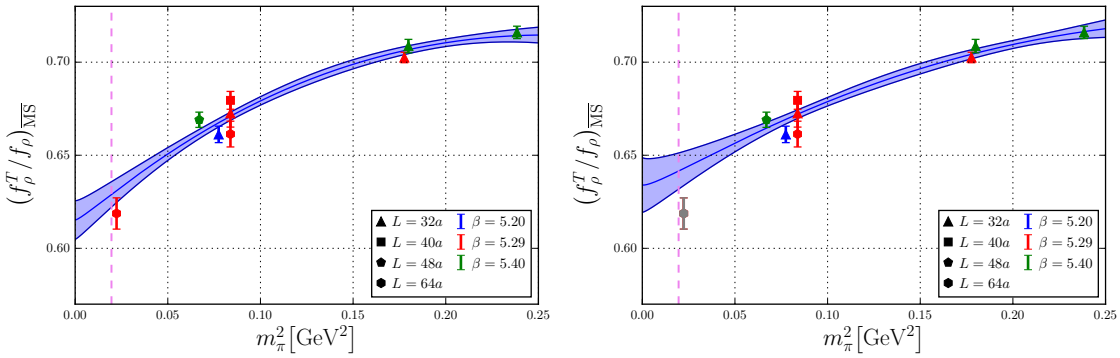

Figure 5.12: ChPT fits using eqs. (5.79) for the ratio f_ρ/f_ρ^T, including (left) and excluding (right) the data point at $m_\pi = 150\,\mathrm{MeV}$. The violet dashed line indicates the position of the physical pion mass. The band indicates the one sigma statistical error.

compute the leading finite-volume corrections for this ratio, see appendix B in [97]. As anticipated for a ratio, the corrections turn out to be numerically tiny such that its finite-volume effects are expected to be much smaller than for the couplings themselves. This expectation is also met by our results, as shown in figure 5.14: The finite-volume effects for the ratio f_ρ^T/f_ρ (right panel) are considerably smaller than for the vector coupling f_ρ itself (left panel). In relation to the statistical errors, the observed volume dependence of f_ρ^T/f_ρ is small and an infinite-volume extrapolation would not have any significant effect. Since in phenomenological studies of hard reactions f_ρ will always be set to the experimental value, the ratio f_ρ^T/f_ρ, which is not experimentally accessible, is a much more interesting quantity. One can see from figure 5.13 that the second moments tend to increase with the spatial volume, however, less significantly than for the normalization constants and the data points have comparatively much larger error bars. As mentioned above, the ChPT analysis of the second moments is not available but the corresponding quantities for stable hadrons have no leading chiral logarithms and a very mild finite-volume dependence. We have checked that excluding the smallest-volume lattice with $m_\pi L = 3.4$ from the fits does not have any noticeable influence on our results.

Due to their elusive nature, discretization errors are difficult to assess. An important reference point is given by the Leibniz sum rule, see eq. (5.77), which leads us to examine the quantities $\langle 1^2\rangle^{\parallel}_{\overline{\rm MS}}$ and $\langle 1^2\rangle^{\perp}_{\overline{\rm MS}}$ as shown in figure 5.15. In the continuum limit they should equal one for all pion masses. While $\langle 1^2\rangle^{\parallel}_{\overline{\rm MS}}$ equals one within the statistical errors with a maximal deviation of about 1%, we observe deviations from one of up to 2% for $\langle 1^2\rangle^{\perp}_{\overline{\rm MS}}$. Note that these deviations are considerably smaller than what we found in the case of the pion [42].

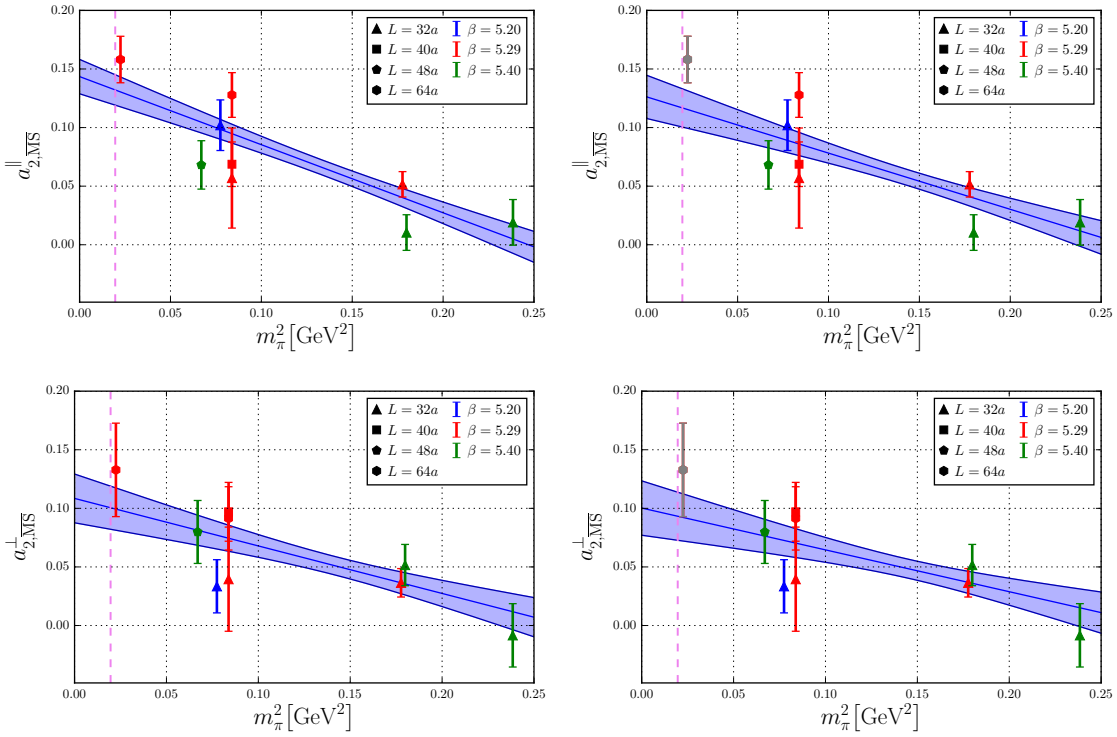

Figure 5.13: Linear fits for the second Gegenbauer moments $a^{\parallel}_{2,\overline{\mathrm{MS}}}$, $a^{\perp}_{2,\overline{\mathrm{MS}}}$ of the linearly and the transversely polarized leading twist distribution amplitudes, including (left) and excluding (right) the data point at $m_\pi = 150\,\mathrm{MeV}$. The violet dashed line indicates the position of the physical pion mass. The band indicates the one sigma statistical error.

5.2.9 Results and conclusion

The final results of our chiral extrapolations are given in table 5.3, where the rows labeled "analysis 1" and "analysis 2" include and exclude the ensemble at $m_\pi = 150\,\mathrm{MeV}$, respectively. The errors stemming from the renormalization were estimated by performing multiple chiral extrapolations, each with a different set of renormalization coefficients, which were determined by using different fit intervals for the renormalization factors themselves. Details on this procedure are found in section 5 of [97]. For the coupling constants and their ratio we have used the fit functions (5.79), whereas the second Gegenbauer moments have been fitted with linear functions of m_π^2. The fact that the results of the two fits are in very good agreement may indicate that the ρ-meson decay $\rho \to \pi\pi$ is not of major importance for the short-distance quantities that we are considering here. Although possibly more relevant with respect to the final values, the available set of lattices does not allow us to estimate discretization errors and finite-size effects in depth. However, we expect to be able to systematically quantify the discretization errors using the new $N_f = 2 + 1$ lattice configurations of the CLS initiative [83]. Compared with the pseudoscalar case,

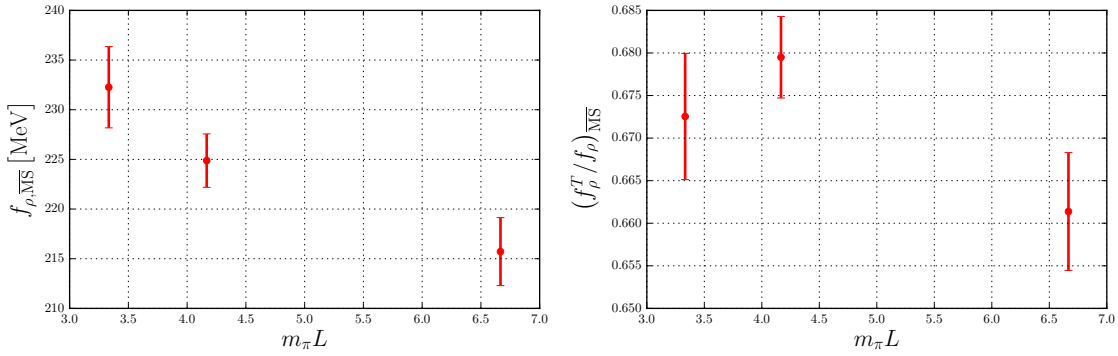

Figure 5.14: Volume dependence of f_ρ (left panel) and f_ρ^T/f_ρ (right panel) at $\beta = 5.29$, $\kappa = 0.13632$.

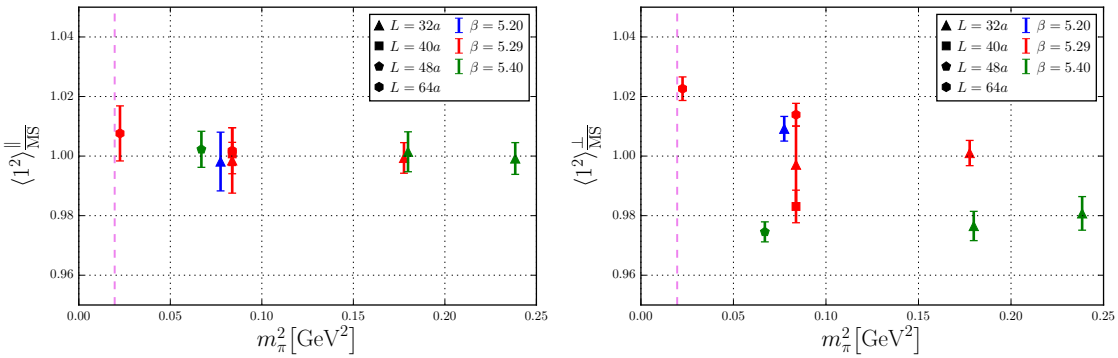

Figure 5.15: The left and the right plot show $\langle 1^2 \rangle^{\parallel}_{\overline{\mathrm{MS}}}$ and $\langle 1^2 \rangle^{\perp}_{\overline{\mathrm{MS}}}$, respectively. The violet dashed line indicates the position of the physical pion mass.

where two non-vanishing momentum components are necessary (see eq. (5.18)), the vector structures of the ρ allow us to extract the second Gegenbauer moments with solely a single non-zero momentum component (see eqs. (5.66) and (5.70)). This results in a significantly smaller error, which can in future studies be even further reduced by employing momentum smearing, cf. section 5.1.4.

We state the values of analysis 1 as our final result. In spite of an absent continuum extrapolation, our final value for the vector coupling, $f_\rho = 199(4)(1)$ MeV, agrees reasonably well with the experimental value $f_{\rho^+} = 210(4)$ MeV, see eq. (5.45). It is interesting to note that sum rule calculations yield a similar result for the vector coupling, $f_\rho^{\mathrm{SR}} = 206(7)$ MeV, but a somewhat bigger value for the tensor coupling, $f_\rho^{T\mathrm{SR}} = 155(8)$ MeV, cf. [175, 182].[3] Although systematic effects are not yet fully under control, the deviations seem to be consistent with the cited errors. In table 5.4 we compare our results for the second moments and the ratio of the coupling constants with QCD sum rule estimates and previous lattice results. Our result for the ratio f_ρ^T/f_ρ is somewhat smaller than the values obtained in

[3] The sum rule results have been evolved from $\mu = 1$ GeV to our reference scale $\mu = 2$ GeV

	f_ρ[MeV]	f_ρ^T[MeV]	f_ρ^T/f_ρ	$a_2^\parallel$	$a_2^\perp$
analysis 1	199(4)(1)	124(4)(1)	0.629(7)(4)	0.132(13)(24)	0.101(18)(12)
analysis 2	194(7)(1)	123(5)(1)	0.642(10)(4)	0.117(16)(24)	0.093(20)(11)

Table 5.3: Results in the $\overline{\text{MS}}$ scheme at $\mu = 2\,\text{GeV}$ from the two analysis methods explained in the main text. The numbers in parentheses denote the statistical error and our estimate of the uncertainty introduced by the renormalization procedure.

	f_ρ^T/f_ρ	$a_2^\parallel$	$a_2^\perp$
this work	0.629(8)	0.132(27)	0.101(22)
sum rules [175, 182]	0.74(5)	0.11(5)	0.11(5)
lattice [183]	0.72(3)	—	—
lattice [184]	0.742(14)	—	—
lattice [185]	0.687(27)	—	—
lattice [43]	—	0.20(6)	—

Table 5.4: Comparison of our results to QCD sum rule estimates and older lattice QCD data. The renormalization scale is $\mu = 2\,\text{GeV}$. Statistical and renormalization errors of our results have been added in quadrature.

other investigations. At our level of accuracy, the observed discrepancies could be a result of the $\rho \to \pi\pi$ decay, the strong pion mass dependence of the ratio (see figure 5.12), possible cut-off effects, or a combination of these. Our final values for the second moments $a_2^\parallel$ and $a_2^\perp$ are in good agreement with other investigations. However, we achieve smaller statistical errors of approximately 20% and therefore start to be sensitive to the difference between the longitudinally and transversely polarized mesons. So far, their values indicate that $a_2^\parallel$ may be slightly larger than $a_2^\perp$, although the difference is not yet statistically significant.

The obtained results are relevant for studies of deeply-virtual vector meson production in electron nucleon scattering using the GPD formalism [173]. Such processes will be investigated with high priority at the JLAB@12 GeV upgrade [26] and, in the future, at the EIC [27]. Also, the tensor coupling appears in calculations of the B-decay form factors at large recoil [176], where in some cases there is a tension with predictions of the Standard Model. As a next step, we will expand our analysis to the $N_f = 2{+}1$ lattice ensembles of the CLS effort. This will not only allow us to perform a controlled continuum extrapolation but also to consider the DAs of the whole $\text{SU}(3)_f$ meson octet, including the K^* meson, whose production is sensitive to strange quarks in the proton [27, 186].

6 Conclusion and outlook

Let us emphasize once again the main results of this thesis. We have argued that hadron distribution amplitudes are QCD functions that are instrumental for the description of hard exclusive processes. A hadron DA corresponds to the probability amplitude to find a hadron in a particular Fock state with a certain momentum distributed between its constituents. Experimentally, DAs appear in convolutions with hard scattering kernels and therefore cannot be measured directly. In order to calculate DAs from first principles we have carried out multiple lattice QCD computer simulations. Although recently a new position-space method was developed for this purpose, we have used the traditional approach which allows to extract the leading Mellin moments of distribution amplitudes more precisely on the lattice.

In chapter 4 we have extended previous lattice calculations of the nucleon DA and performed the first calculation of the DAs of the whole $J^P = \frac{1}{2}^+$ baryon octet. We employed CLS ensembles that incorporate $N_f = 2 + 1$ dynamical sea quarks and hence are particularly suited for this purpose. Taking into account the missing continuum extrapolation, our results for the nucleon decay constant are in good agreement with previous calculations. For the coupling constants of the remaining octet baryons, we observe SU(3) flavor breaking effects between $20 - 50\%$. In agreement with state of the art LCSR and previous lattice calculations, our results for the shape parameters are up to an order of magnitude smaller than predicted by early QCD sum rule calculations. Despite their small absolute values, we unexpectedly noticed considerable SU(3) splitting effects of the octet shape parameters. This behavior is especially interesting for hard exclusive processes that are sensitive to deviations of DAs from their asymptotic form. As our results come from ensembles at a single lattice spacing of $a \approx 0.0857$ fm, we could not examine possible lattice cut-off effects which we expect to be of order $20 - 30\%$.

Chapter 5 was devoted to the determination of meson distribution amplitudes on the lattice. With regard to the pion, previous attempts to calculate the second Gegenbauer moment lacked the capability to perform a reliable continuum extrapolation. The main reason for this are large statistical errors due to the requirement of at least two non-vanishing momentum components in the two-point function. In section 5.1 we have employed a new smearing technique in an exploratory calculation of the second moment. The momentum smearing shifts the smearing kernel in momentum-space, which results in an improved overlap with the actual hadron state. This comes, unfortunately, at the

computational cost of two inversions per desired meson momentum. However, in the case of the pion, we were able to show that the new technique allows drastically reduced statistical errors to be achieved with the same computational effort. We expect this to be even more effective for non-degenerate mesons like the K or the K^*, since in these cases two inversions are already required with the standard Wuppertal smearing. In contrast to the pion, the nucleon two-point function does not involve quarks that propagate in the backward direction and therefore a significant statistical gain can be anticipated.

Section 5.2 contains an analysis of the DAs of the ρ-meson using the standard Wuppertal smearing. In this calculation, we have considered the coupling constants as well as the second moments of both, the vector and tensor current. In contrast to the pion, the extraction of the second moments requires only one non-vanishing momentum component which improves the statistical errors of the correlation functions. The included ensembles have $N_f = 2$ sea quarks and pion masses down to $m_\pi = 150\,\mathrm{MeV}$. In order to examine the effects of the $\rho \to \pi\pi$ decay we have conducted chiral extrapolations with and without the ensemble with $m_\pi = 150\,\mathrm{MeV}$. However, we have not observed any significant difference between these two approaches and conclude that the effects of the decay are only of minor importance for short-distant quantities. Our result for the vector decay constant is consistent with experimental measurements while our final value for the ratio of the tensor and vector decay constants turns out to be smaller than in other publications. This might be linked to a significant pion mass dependence or cut-off effects. Our results for the second moments are in good agreement with other studies whilst at the same time achieving smaller statistical errors.

We conclude this thesis by stressing that the methods and know-how obtained from these projects lay the foundation for the upcoming continuum extrapolations of both, the distribution amplitudes of the baryon octet as well as the pseudoscalar and vector meson octets. We aim to conduct combined fits along $\mathrm{Tr}\,M = \text{const.}$ and $m_s = \text{const.}$ mass trajectories that include a joint chiral and continuum extrapolation, such that all ChPT constraints will automatically be fulfilled in the limit $a \to 0$. For this purpose we will employ numerous $N_f = 2 + 1$ CLS ensembles with multiple lattice spacings.

Acknowledgments

First and foremost I would like to thank *Andreas Schäfer* for his excellent supervision and guidance throughout this work. He always had an open ear for every problem and offered valuable advice while at the same time creating an outstanding working atmosphere. In addition, I am very much obliged to *Vladimir Braun* for his assistance and support during my time at the Regensburg QCD group. He has been mentoring me since my bachelor thesis and has always provided exceptional advice and insight into complex circumstances. I also thank *Gunnar Bali*, *Sara Collins*, *Meinulf Göckeler* and *Wolfgang Söldner* for consulting me in many technical matters as well as *Rainer Schiel* for his excellent introduction to lattice QCD. I am especially grateful to the *Studienstiftung des deutschen Volkes* for the scholarship and financial support of this thesis.

Many projects would not have been possible without the wonderful collaborations with my colleagues from the Regensburg QCD group. In particular I take great pleasure in acknowledging gratitude to *Philipp Wein*, *Michael Gruber*, *Piotr Korcyl*, *Thomas Wurm*, *Rudolf Rödl* and *Simon Bürger* for uncountable fruitful discussions and joint projects. Through them I learned that a team can achieve much more than the sum of its parts.

Last but not least, I would like to thank my parents *Peter* and *Silvia* for their unconditional love and support at all times, as well as my beloved girlfriend *Vera*, who accompanied and supported me wholeheartedly at every step of the way.

7 Bibliography

[1] T. Y. Cao, *From Current Algebra to Quantum Chromodynamics*. Cambridge University Press, Cambridge, UK, 2010.

[2] G. F. Chew and S. C. Frautschi, "Potential Scattering as Opposed to Scattering Associated with Independent Particles in the S-Matrix Theory of Strong Interactions," *Phys. Rev.* **124** (1961) 264.

[3] G. F. Chew and S. C. Frautschi, "Principle of Equivalence for all Strongly Interacting Particles within the S-Matrix Framework," *Phys. Rev. Lett.* **7** (1961) 394.

[4] M. Gell-Mann, "Particle theory from S-matrix to quarks," *Conf. Proc.* **C8309201** (1983) 473.

[5] W. Pauli, "The Connection Between Spin and Statistics," *Phys. Rev.* **58** (1940) 716.

[6] O. W. Greenberg, "Spin and Unitary-Spin Independence in a Paraquark Model of Baryons and Mesons," *Phys. Rev. Lett.* **13** (1964) 598.

[7] F. Tkachov, "A contribution to the history of quarks: Boris Struminsky's 1965 JINR publication," `arXiv:0904.0343 [physics.hist-ph]`.

[8] M. Y. Han and Y. Nambu, "Three-Triplet Model with Double SU(3) Symmetry," *Phys. Rev.* **139** (1965) B1006.

[9] C. N. Yang and R. L. Mills, "Conservation of Isotopic Spin and Isotopic Gauge Invariance," *Phys. Rev.* **96** (1954) 191.

[10] **Particle Data Group** Collaboration, C. Patrignani *et al.*, "Review of Particle Physics," *Chin. Phys.* **C40** (2016) 100001.

[11] R. D. Ball *et al.*, "Parton distribution benchmarking with LHC Data," *JHEP* **04** (2013) 125, `arXiv:1211.5142`.

[12] J. Rojo *et al.*, "The PDF4LHC report on PDFs and LHC data: results from Run I and preparation for Run II," *J. Phys.* **G42** (2015) 103103, `arXiv:1507.00556`.

[13] L. A. Harland-Lang, A. D. Martin, P. Motylinski, and R. S. Thorne, "Parton distributions in the LHC era: MMHT 2014 PDFs," *Eur. Phys. J.* **C75** (2015) 204, arXiv:1412.3989.

[14] **NNPDF** Collaboration, R. D. Ball *et al.*, "Parton distributions for the LHC run II," *JHEP* **04** (2015) 040, arXiv:1410.8849.

[15] S. Dulat *et al.*, "New parton distribution functions from a global analysis of quantum chromodynamics," *Phys. Rev.* **D93** (2016) 033006, arXiv:1506.07443.

[16] **H1 and ZEUS** Collaborations, H. Abramowicz *et al.*, "Combination of measurements of inclusive deep inelastic $e^{\pm}p$ scattering cross sections and QCD analysis of HERA data," *Eur. Phys. J.* **C75** (2015) 580, arXiv:1506.06042.

[17] R. P. Feynman, "Very High-Energy Collisions of Hadrons," *Phys. Rev. Lett.* **23** (1969) 1415.

[18] J. D. Bjorken, "Asymptotic Sum Rules at Infinite Momentum," *Phys. Rev.* **179** (1969) 1547.

[19] D. H. Perkins, "Neutrino interactions," *eConf* **C720906** (1972) 189.

[20] V. N. Gribov and L. N. Lipatov, "Deep inelastic *ep* scattering in perturbation theory," *Sov. J. Nucl. Phys.* **15** (1972) 438. [*Yad. Fiz.* **15** (1972) 781].

[21] G. Altarelli and G. Parisi, "Asymptotic freedom in parton language," *Nucl. Phys.* **B126** (1977) 298.

[22] Y. L. Dokshitser, "Calculation of structure functions for deep- inelastic scattering and e^+e^- annihilation by perturbation theory in quantum chromodynamics.," *Sov. Phys. JETP* **46** (1977) 641. [*Zh. Eksp. Teor. Fiz.* **73** (1977) 1216].

[23] G. P. Lepage and S. J. Brodsky, "Exclusive processes in perturbative quantum chromodynamics," *Phys. Rev.* **D22** (1980) 2157.

[24] G. S. Bali *et al.*, "Light-cone distribution amplitudes of the baryon octet," *JHEP* **02** (2016) 070, arXiv:1512.02050.

[25] V. L. Chernyak and A. R. Zhitnitsky, "Asymptotic behavior of exclusive processes in QCD," *Phys. Rept.* **112** (1984) 173.

[26] J. Dudek *et al.*, "Physics opportunities with the 12 GeV upgrade at Jefferson Lab," *Eur. Phys. J.* **A48** (2012) 187, arXiv:1208.1244.

[27] A. Accardi *et al.*, "Electron Ion Collider: The next QCD frontier," *Eur. Phys. J.* **A52** (2016) 268, arXiv:1212.1701.

[28] A. V. Efremov and A. V. Radyushkin, "Factorization and asymptotic behaviour of pion form factor in QCD," *Phys. Lett.* **94B** (1980) 245.

[29] V. M. Braun, "Hadron Wave Functions from Lattice QCD," *Few-Body Syst.* **57** (2016) 1019.

[30] V. Braun and I. Halperin, "Soft contribution to the pion form factor from light-cone QCD sum rules," *Phys. Lett.* **B328** (1994) 457, `arXiv:hep-ph/9402270`.

[31] V. M. Braun, A. Lenz, N. Mahnke, and E. Stein, "Light cone sum rules for the nucleon form factors," *Phys. Rev.* **D65** (2002) 074011, `arXiv:hep-ph/0112085`.

[32] K. G. Wilson, "Confinement of quarks," *Phys. Rev.* **D10** (1974) 2445.

[33] M. Creutz, L. Jacobs, and C. Rebbi, "Experiments with a Gauge Invariant Ising System," *Phys. Rev. Lett.* **42** (1979) 1390.

[34] K. G. Wilson, "Monte-Carlo Calculations for the Lattice Gauge Theory," *NATO Sci. Ser.* **B59** (1980) 363.

[35] M. Creutz, "Monte Carlo study of quantized SU(2) gauge theory," *Phys. Rev.* **D21** (1980) 2308.

[36] D. Weingarten, "Monte Carlo evaluation of hadron masses in lattice gauge theories with fermions," *Phys. Lett.* **109B** (1982) 57.

[37] H. Hamber and G. Parisi, "Numerical Estimates of Hadronic Masses in a Pure SU(3) Gauge Theory," *Phys. Rev. Lett.* **47** (1981) 1792.

[38] S. Schaefer, "Algorithms for lattice QCD: progress and challenges," *AIP Conf. Proc.* **1343** (2011) 93, `arXiv:1011.5641`.

[39] A. S. Kronfeld and D. M. Photiadis, "Phenomenology on the lattice: Composite operators in lattice gauge theory," *Phys. Rev.* **D31** (1985) 2939.

[40] G. Martinelli and C. T. Sachrajda, "A lattice calculation of the second moment of the pion's distribution amplitude," *Phys. Lett.* **B190** (1987) 151.

[41] G. Martinelli and C. T. Sachrajda, "The quark distribution amplitude of the Proton: A lattice computation of the lowest two moments," *Phys. Lett.* **B217** (1989) 319.

[42] V. M. Braun *et al.*, "Second moment of the pion light-cone distribution amplitude from lattice QCD," *Phys. Rev.* **D92** (2015) 014504, `arXiv:1503.03656`.

[43] **RBC and UKQCD** Collaborations, R. Arthur *et al.*, "Lattice results for low moments of light meson distribution amplitudes," *Phys. Rev.* **D83** (2011) 074505, arXiv:1011.5906.

[44] V. M. Braun *et al.*, "Light-cone distribution amplitudes of the nucleon and negative parity nucleon resonances from lattice QCD," *Phys. Rev.* **D89** (2014) 094511, arXiv:1403.4189.

[45] L. D. Faddeev and V. N. Popov, "Feynman diagrams for the Yang-Mills field," *Phys. Lett.* **25B** (1967) 29.

[46] C. Becchi, A. Rouet, and R. Stora, "The abelian Higgs Kibble model, unitarity of the S- operator," *Phys. Lett.* **52B** (1974) 344.

[47] C. Becchi, A. Rouet, and R. Stora, "Renormalization of the Abelian Higgs-Kibble Model," *Commun. Math. Phys.* **42** (1975) 127.

[48] C. Becchi, A. Rouet, and R. Stora, "Renormalization of Gauge Theories," *Annals Phys.* **98** (1976) 287.

[49] I. V. Tyutin, "Gauge Invariance in Field Theory and Statistical Physics in Operator Formalism," arXiv:0812.0580.

[50] M. Göckeler and T. Schücker, *Differential geometry, gauge theories, and gravity.* Cambridge University Press, Cambridge, UK, 1989.

[51] M. E. Peskin and D. V. Schroeder, *An Introduction to Quantum Field Theory.* Westview Press, Boulder, USA, 1995.

[52] M. Gell-Mann, "Symmetries of baryons and mesons," *Phys. Rev.* **125** (1962) 1067.

[53] C. G. Callan, Jr., R. F. Dashen, and D. J. Gross, "The Structure of the Gauge Theory Vacuum," *Phys. Lett.* **63B** (1976) 334.

[54] M. Pospelov and A. Ritz, "Theta-Induced Electric Dipole Moment of the Neutron via QCD Sum Rules," *Phys. Rev. Lett.* **83** (1999) 2526, arXiv:hep-ph/9904483.

[55] M. Pospelov and A. Ritz, "Theta vacua, QCD sum rules, and the neutron electric dipole moment," *Nucl. Phys.* **B573** (2000) 177, arXiv:hep-ph/9908508.

[56] S. A. Abel and O. Lebedev, "Neutron-electron EDM correlations in supersymmetry and prospects for EDM searches," *JHEP* **01** (2006) 133, arXiv:hep-ph/0508135.

[57] C. A. Baker *et al.*, "Improved Experimental Limit on the Electric Dipole Moment of the Neutron," *Phys. Rev. Lett.* **97** (2006) 131801, arXiv:hep-ex/0602020.

[58] K. Ottnad, B. Kubis, U.-G. Meißner, and F.-K. Guo, "New insights into the neutron electric dipole moment," *Phys. Lett.* **B687** (2010) 42, arXiv:0911.3981.

[59] R. D. Peccei and H. R. Quinn, "CP Conservation in the Presence of Pseudoparticles," *Phys. Rev. Lett.* **38** (1977) 1440.

[60] F. J. Dyson, "The S Matrix in Quantum Electrodynamics," *Phys. Rev.* **75** (1949) 1736.

[61] K. Osterwalder and R. Schrader, "Axioms for Euclidean Green's Functions," *Commun. Math. Phys.* **31** (1973) 83.

[62] C. Gattringer and C. B. Lang, *Quantum Chromodynamics on the Lattice*. Springer, Berlin, Germany, 2010.

[63] J. Smit, *Introduction to Quantum Fields on a Lattice*. Cambridge University Press, Cambridge, UK, 2002.

[64] H. J. Rothe, *Lattice Gauge Theories*. World Scientific, Singapore, 2012.

[65] B. Sheikholeslami and R. Wohlert, "Improved continuum limit lattice action for QCD with Wilson fermions," *Nucl. Phys.* **B259** (1985) 572.

[66] M. Lüscher, S. Sint, R. Sommer, and P. Weisz, "Chiral symmetry and O(a) improvement in lattice QCD," *Nucl. Phys.* **B478** (1996) 365, arXiv:hep-lat/9605038.

[67] K. Jansen and R. Sommer, "$O(a)$ improvement of lattice QCD with two flavors of Wilson quarks," *Nucl. Phys.* **B530** (1998) 185, arXiv:hep-lat/9803017. [Erratum: *Nucl. Phys.* **B643** (2002) 517].

[68] P. Weisz, "Continuum limit improved lattice action for pure Yang-Mills theory (I)," *Nucl. Phys.* **B212** (1983) 1.

[69] M. Lüscher and P. Weisz, "On-shell Improved Lattice Gauge Theories," *Commun. Math. Phys.* **97** (1985) 59. [Erratum: *Commun. Math. Phys.* **98** (1985) 433].

[70] A. Haar, "Der Massbegriff in der Theorie der kontinuierlichen Gruppen," *Ann. Math.* (1933) 147.

[71] N. Metropolis, A. W. Rosenbluth, M. N. Rosenbluth, A. H. Teller, and E. Teller, "Equation of State Calculations by Fast Computing Machines," *J. Chem. Phys.* **21** (1953) 1087.

[72] C. Itzykson and J.-M. Drouffe, *Statistical Field Theory: Volume 2, Strong Coupling, Monte Carlo Methods, Conformal Field Theory and Random Systems*. Cambridge University Press, Cambridge, UK, 1989.

[73] **CP-PACS** Collaboration, S. Aoki *et al.*, "Light hadron spectrum and quark masses from quenched lattice QCD," *Phys. Rev.* **D67** (2003) 034503, arXiv:hep-lat/0206009.

[74] **UKQCD** Collaboration, K. C. Bowler *et al.*, "Quenched QCD with $O(a)$ improvement: The spectrum of light hadrons," *Phys. Rev.* **D62** (2000) 054506, arXiv:hep-lat/9910022.

[75] S. Duane, A. D. Kennedy, B. J. Pendleton, and D. Roweth, "Hybrid Monte Carlo," *Phys. Lett.* **B195** (1987) 216.

[76] M. Creutz, "Global Monte Carlo algorithms for many-fermion systems," *Phys. Rev.* **D38** (1988) 1228.

[77] R. Gupta, G. W. Kilcup, and S. R. Sharpe, "Tuning the hybrid Monte Carlo algorithm," *Phys. Rev.* **D38** (1988) 1278.

[78] M. Lüscher, "Computational Strategies in Lattice QCD," arXiv:1002.4232.

[79] I. Horváth, A. D. Kennedy, and S. Sint, "A New Exact Method for Dynamical Fermion Computations with Non-Local Actions," *Nucl. Phys. B (Proc. Suppl.)* **73** (1999) 834, arXiv:hep-lat/9809092.

[80] M. A. Clark and A. D. Kennedy, "Accelerating Dynamical-Fermion Computations Using the Rational Hybrid Monte Carlo Algorithm with Multiple Pseudofermion Fields," *Phys. Rev. Lett.* **98** (2007) 051601, arXiv:hep-lat/0608015.

[81] M. Lüscher and S. Schaefer, "Lattice QCD with open boundary conditions and twisted-mass reweighting," *Comput. Phys. Commun.* **184** (2013) 519, arXiv:1206.2809.

[82] N. I. Achieser, *Theory of Approximation*. Courier Corporation, North Chelmsford, USA, 2013.

[83] M. Bruno *et al.*, "Simulation of QCD with $N_f = 2 + 1$ flavors of non-perturbatively improved Wilson fermions," *JHEP* **02** (2015) 043, arXiv:1411.3982.

[84] J. Bulava and S. Schaefer, "Improvement of $N_f = 3$ lattice QCD with Wilson fermions and tree-level improved gauge action," *Nucl. Phys.* **B874** (2013) 188, arXiv:1304.7093.

[85] M. Lüscher, "Topology, the Wilson flow and the HMC algorithm," *PoS* **LATTICE 2010** (2010) 015, arXiv:1009.5877.

[86] M. Lüscher and S. Schaefer, "Lattice QCD without topology barriers," *JHEP* **07** (2011) 036, arXiv:1105.4749.

[87] L. Del Debbio, L. Giusti, M. Lüscher, R. Petronzio, and N. Tantalo, "Stability of lattice QCD simulations and the thermodynamic limit," *JHEP* **02** (2006) 011, arXiv:hep-lat/0512021.

[88] M. Lüscher and F. Palombi, "Fluctuations and reweighting of the quark determinant on large lattices," *PoS* **LATTICE 2008** (2008) 049, arXiv:0810.0946.

[89] T. A. DeGrand, "A conditioning technique for matrix inversion for Wilson fermions," *Comput. Phys. Commun.* **52** (1988) 161.

[90] **RQCD** Collaboration, G. S. Bali, E. E. Scholz, J. Simeth, and W. Söldner, "Lattice simulations with $N_f = 2 + 1$ improved Wilson fermions at a fixed strange quark mass," *Phys. Rev.* **D94** (2016) 074501, arXiv:1606.09039.

[91] **RQCD** Collaboration, G. S. Bali *et al.*, "Direct determinations of the nucleon and pion σ terms at nearly physical quark masses," *Phys. Rev.* **D93** (2016) 094504, arXiv:1603.00827.

[92] S. Güsken, "A study of smearing techniques for hadron correlation functions," *Nucl. Phys. B (Proc. Suppl.)* **17** (1990) 361.

[93] M. Falcioni, M. L. Paciello, G. Parisi, and B. Taglienti, "Again on SU(3) glueball mass," *Nucl. Phys.* **B251** (1985) 624.

[94] **QCDSF and UKQCD** Collaborations, W. Bietenholz *et al.*, "Flavour blindness and patterns of flavour symmetry breaking in lattice simulations of up, down and strange quarks," *Phys. Rev.* **D84** (2011) 054509, arXiv:1102.5300.

[95] **QCDSF and UKQCD** Collaborations, M. Göckeler *et al.*, "Baryon axial charges and momentum fractions with $N_f = 2 + 1$ dynamical fermions," *PoS* **LATTICE 2010** (2010) 163, arXiv:1102.3407.

[96] **QCDSF and UKQCD** Collaborations, A. N. Cooke *et al.*, "SU(3) flavour breaking and baryon structure," *PoS* **LATTICE 2013** (2014) 278, arXiv:1311.4916.

[97] V. M. Braun *et al.*, "The ρ-meson light-cone distribution amplitudes from lattice QCD," *JHEP* **04** (2017) 082.

[98] C.-Y. Wong, *Introduction to High-Energy Heavy-Ion Collisions*. World Scientific, Singapore, 1994.

[99] I. G. Aznauryan *et al.*, "Studies of Nucleon Resonance Structure in Exclusive Meson Electroproduction," *Int. J. Mod. Phys.* **E22** (2013) 1330015, arXiv:1212.4891.

[100] V. M. Braun, A. Lenz, and M. Wittmann, "Nucleon form factors in QCD," *Phys. Rev.* **D73** (2006) 094019, arXiv:hep-ph/0604050.

[101] I. I. Balitsky, V. M. Braun, and A. V. Kolesnichenko, "Radiative decay $\Sigma^+ \to p\gamma$ in quantum chromodynamics," *Nucl. Phys.* **B312** (1989) 509.

[102] V. L. Chernyak and I. R. Zhitnitsky, "B-meson exclusive decays into baryons," *Nucl. Phys.* **B345** (1990) 137.

[103] M. A. Shifman, A. I. Vainshtein, and V. I. Zakharov, "QCD and resonance physics. Theoretical foundations," *Nucl. Phys.* **B147** (1979) 385.

[104] M.-Q. Huang and D.-W. Wang, "Light-cone QCD sum rules for the semileptonic decay $\Lambda_b \to pl\bar{\nu}$," *Phys. Rev.* **D69** (2004) 094003, arXiv:hep-ph/0401094.

[105] V. M. Braun, A. Lenz, G. Peters, and A. V. Radyushkin, "Light cone sum rules for $\gamma^* N \to \Delta$ transition form-factors," *Phys. Rev.* **D73** (2006) 034020, arXiv:hep-ph/0510237.

[106] J. Arrington, C. D. Roberts, and J. M. Zanotti, "Nucleon electromagnetic form factors," *J. Phys.* **G34** (2007) S23, arXiv:nucl-th/0611050.

[107] C. F. Perdrisat, V. Punjabi, and M. Vanderhaeghen, "Nucleon electromagnetic form factors," *Prog. Part. Nucl. Phys.* **59** (2007) 694, arXiv:hep-ph/0612014.

[108] J. Arrington, K. de Jager, and C. F. Perdrisat, "Nucleon Form Factors: A Jefferson Lab Perspective," *J. Phys. Conf. Ser.* **299** (2011) 012002, arXiv:1102.2463.

[109] V. Punjabi, C. F. Perdrisat, M. K. Jones, E. J. Brash, and C. E. Carlson, "The structure of the nucleon: Elastic electromagnetic form factors," *Eur. Phys. J.* **A51** (2015) 79, arXiv:1503.01452.

[110] Z. Ye, J. Arrington, R. J. Hill, and G. Lee, "Proton and neutron electromagnetic form factors and uncertainties," *Phys. Lett.* **B777** (2018) 8, arXiv:1707.09063.

[111] **DM2** Collaboration, D. Bisello *et al.*, "Baryon pairs production in e^+e^- annihilation at $\sqrt{s} = 2.4$ GeV," *Z. Phys.* **C48** (1990) 23.

[112] **BaBar** Collaboration, B. Aubert *et al.*, "Study of $e^+e^- \to \Lambda\bar{\Lambda}$, $\Lambda\bar{\Sigma}^0$, $\Sigma^0\bar{\Sigma}^0$ using initial state radiation with BABAR," *Phys. Rev.* **D76** (2007) 092006, arXiv:0709.1988.

[113] S. Dobbs, A. Tomaradze, T. Xiao, K. K. Seth, and G. Bonvicini, "First measurements of timelike form factors of the hyperons, $\Lambda^0, \Sigma^0, \Sigma^+, \Xi^0, \Xi^-$ and Ω^-, and evidence of diquark correlations," *Phys. Lett.* **B739** (2014) 90, arXiv:1410.8356.

[114] **PANDA** Collaboration, W. Erni *et al.*, "Physics Performance Report for PANDA: Strong Interaction Studies with Antiprotons," arXiv:0903.3905.

[115] **CDF** Collaboration, T. Aaltonen *et al.*, "Observation of the Baryonic Flavor-Changing Neutral Current Decay $\Lambda_b^0 \to \Lambda\mu^+\mu^-$," *Phys. Rev. Lett.* **107** (2011) 201802, arXiv:1107.3753.

[116] **LHCb** Collaboration, R. Aaij *et al.*, "Measurement of the differential branching fraction of the decay $\Lambda_b^0 \to \Lambda\mu^+\mu^-$," *Phys. Lett.* **B725** (2013) 25, arXiv:1306.2577.

[117] **QCDSF** Collaboration, V. M. Braun *et al.*, "Nucleon distribution amplitudes and proton decay matrix elements on the lattice," *Phys. Rev.* **D79** (2009) 034504, arXiv:0811.2712.

[118] **QCDSF** Collaboration, V. M. Braun *et al.*, "Nucleon and $N^*(1535)$ Distribution Amplitudes," *PoS* **LATTICE 2010** (2010) 158, arXiv:1011.1092.

[119] V. Braun, R. J. Fries, N. Mahnke, and E. Stein, "Higher twist distribution amplitudes of the nucleon in QCD," *Nucl. Phys.* **B589** (2000) 381, arXiv:hep-ph/0007279. [Erratum: *Nucl. Phys.* **B607** (2001) 433].

[120] M. Gruber, *Renormalization of three-quark operators for baryon distribution amplitudes.* PhD thesis, Universität Regensburg, 2017.

[121] P. Wein and A. Schäfer, "Model-independent calculation of $\mathrm{SU}(3)_f$ violation in baryon octet light-cone distribution amplitudes," *JHEP* **05** (2015) 073, arXiv:1501.07218.

[122] V. M. Braun, A. N. Manashov, and J. Rohrwild, "Baryon operators of higher twist in QCD and nucleon distribution amplitudes," *Nucl. Phys.* **B807** (2009) 89, arXiv:0806.2531.

[123] X. Ji, J.-P. Ma, and F. Yuan, "Three-quark light-cone amplitudes of the proton and quark orbital-motion-dependent observables," *Nucl. Phys.* **B652** (2003) 383, arXiv:hep-ph/0210430.

[124] A. V. Belitsky and A. V. Radyushkin, "Unraveling hadron structure with generalized parton distributions," *Phys. Rept.* **418** (2005) 1, arXiv:hep-ph/0504030.

[125] R. L. Jaffe and X. Ji, "Chiral-Odd Parton Distributions and Polarized Drell-Yan Process," *Phys. Rev. Lett.* **67** (1991) 552.

[126] J. B. Kogut and D. E. Soper, "Quantum Electrodynamics in the Infinite Momentum Frame," *Phys. Rev.* **D1** (1970) 2901.

[127] P. Ball and V. M. Braun, "Higher twist distribution amplitudes of vector mesons in QCD: twist-4 distributions and meson mass corrections," *Nucl. Phys.* **B543** (1999) 201, arXiv:hep-ph/9810475.

[128] M. Claudson, M. B. Wise, and L. J. Hall, "Chiral lagrangian for deep mine physics," *Nucl. Phys.* **B195** (1982) 297.

[129] V. M. Belyaev and B. L. Ioffe, "Determination of the baryon mass and baryon resonances from the quantum-chromodynamics sum rule. Strange baryons," *Sov. Phys. JETP* **57** (1983) 716. [*Zh. Eksp. Teor. Fiz.* **84** (1983) 1236].

[130] B. L. Ioffe and A. V. Smilga, "Hyperon magnetic moments in QCD," *Phys. Lett.* **133B** (1983) 436.

[131] T. M. Aliev and M. Savcı, "Octet negative parity to octet positive parity electromagnetic transitions in light cone QCD," *J. Phys.* **G41** (2014) 075007, arXiv:1403.0096.

[132] D. B. Leinweber, W. Melnitchouk, D. G. Richards, A. G. Williams, and J. M. Zanotti, "Baryon Spectroscopy in Lattice QCD," *Lect. Notes Phys.* **663** (2005) 71, arXiv:nucl-th/0406032.

[133] T. Kaltenbrunner, M. Göckeler, and A. Schäfer, "Irreducible multiplets of three-quark operators on the lattice: Controlling mixing under renormalization," *Eur. Phys. J.* **C55** (2008) 387, arXiv:0801.3932.

[134] S. Weinberg, "Phenomenological Lagrangians," *Physica* **96A** (1979) 327.

[135] P. Wein, P. C. Bruns, T. R. Hemmert, and A. Schäfer, "Chiral extrapolation of nucleon wave function normalization constants," *Eur. Phys. J.* **A47** (2011) 149, arXiv:1106.3440.

[136] **QCDSF** Collaboration, R. W. Schiel *et al.*, "An Update on Distribution Amplitudes of the Nucleon and its Parity Partner," *PoS* **LATTICE 2011** (2011) 175, arXiv:1112.0473.

[137] I. V. Anikin, V. M. Braun, and N. Offen, "Nucleon form factors and distribution amplitudes in QCD," *Phys. Rev.* **D88** (2013) 114021, arXiv:1310.1375.

[138] V. L. Chernyak, A. A. Ogloblin, and I. R. Zhitnitsky, "Wave functions of octet baryons," *Z. Phys.* **C42** (1989) 569.

[139] J. A. Gracey, "Three loop renormalization of 3-quark operators in QCD," *JHEP* **09** (2012) 052, arXiv:1208.5619.

[140] V. L. Chernyak and I. R. Zhitnitsky, "Nucleon wave function and nucleon form factors in QCD," *Nucl. Phys.* **B246** (1984) 52.

[141] **BaBar** Collaboration, B. Aubert *et al.*, "Measurement of the $\gamma\gamma^* \to \pi^0$ transition form factor," *Phys. Rev.* **D80** (2009) 052002, arXiv:0905.4778.

[142] **Belle** Collaboration, S. Uehara *et al.*, "Measurement of $\gamma\gamma^* \to \pi^0$ transition form factor at Belle," *Phys. Rev.* **D86** (2012) 092007, arXiv:1205.3249.

[143] A. V. Radyushkin, "Shape of pion distribution amplitude," *Phys. Rev.* **D80** (2009) 094009, arXiv:0906.0323.

[144] S. S. Agaev, V. M. Braun, N. Offen, and F. A. Porkert, "Light cone sum rules for the $\pi^0\gamma^*\gamma$ form factor revisited," *Phys. Rev.* **D83** (2011) 054020, arXiv:1012.4671.

[145] A. P. Bakulev, S. V. Mikhailov, A. V. Pimikov, and N. G. Stefanis, "Comparing antithetic trends of data for the pion-photon transition form factor," *Phys. Rev.* **D86** (2012) 031501, arXiv:1205.3770.

[146] S. S. Agaev, V. M. Braun, N. Offen, and F. A. Porkert, "Belle data on the $\pi^0\gamma^*\gamma$ form factor: A game changer?," *Phys. Rev.* **D86** (2012) 077504, arXiv:1206.3968.

[147] V. L. Chernyak and S. I. Eidelman, "Hard exclusive two photon processes in QCD," *Prog. Part. Nucl. Phys.* **80** (2014) 1, arXiv:1409.3348.

[148] A. E. Dorokhov, "Photon-pion transition form factor: BABAR puzzle is cracked," arXiv:1003.4693.

[149] P. Ball and R. Zwicky, "New results on $B \to \pi, K, \eta$ decay form factors from light-cone sum rules," *Phys. Rev.* **D71** (2005) 014015, arXiv:hep-ph/0406232.

[150] G. Duplančić, A. Khodjamirian, T. Mannel, B. Melić, and N. Offen, "Light-cone sum rules for $B \to \pi$ form factors revisited," *JHEP* **04** (2008) 014, arXiv:0801.1796.

[151] A. Khodjamirian, T. Mannel, N. Offen, and Y. M. Wang, "$B \to \pi \ell \nu_\ell$ width and $|V_{ub}|$ from QCD light-cone sum rules," *Phys. Rev.* **D83** (2011) 094031, arXiv:1103.2655.

[152] M. Beneke, G. Buchalla, M. Neubert, and C. T. Sachrajda, "QCD Factorization for $B \to \pi\pi$ Decays: Strong Phases and CP Violation in the Heavy Quark Limit," *Phys. Rev. Lett.* **83** (1999) 1914, arXiv:hep-ph/9905312.

[153] M. Beneke and M. Neubert, "QCD factorization for $B \to PP$ and $B \to PV$ decays," *Nucl. Phys.* **B675** (2003) 333, arXiv:hep-ph/0308039.

[154] V. M. Braun and D. Müller, "Exclusive processes in position space and the pion distribution amplitude," *Eur. Phys. J.* **C55** (2008) 349, arXiv:0709.1348.

[155] X. Ji, "Parton Physics on a Euclidean Lattice," *Phys. Rev. Lett.* **110** (2013) 262002, arXiv:1305.1539 [hep-ph].

[156] A. V. Radyushkin, "Quasi-parton distribution functions, momentum distributions, and pseudo-parton distribution functions," *Phys. Rev.* **D96** (2017) 034025, arXiv:1705.01488 [hep-ph].

[157] A. V. Radyushkin, "Pion distribution amplitude and quasidistributions," *Phys. Rev.* **D95** (2017) 056020, arXiv:1701.02688 [hep-ph].

[158] **RQCD** Collaboration, G. S. Bali, B. Lang, B. U. Musch, and A. Schäfer, "Novel quark smearing for hadrons with high momenta in lattice QCD," *Phys. Rev.* **D93** (2016) 094515, arXiv:1602.05525.

[159] **LP^3** Collaboration, J.-W. Chen *et al.*, "Kaon Distribution Amplitude from Lattice QCD and the Flavor SU(3) Symmetry," arXiv:1712.10025 [hep-ph].

[160] L. Chang *et al.*, "Imaging dynamical chiral symmetry breaking: pion wave function on the light front," *Phys. Rev. Lett.* **110** (2013) 132001, arXiv:1301.0324.

[161] J. P. B. C. de Melo, I. Ahmed, and K. Tsushima, "Parton Distribution in Pseudoscalar Mesons with a Light-Front Constituent Quark Model," *AIP Conf. Proc.* **1735** (2016) 080012, arXiv:1512.07260.

[162] G. S. Bali *et al.*, "Pion distribution amplitude from Euclidean correlation functions," *Eur. Phys. J.* **C78** (2018) 217, arXiv:1709.04325 [hep-lat].

[163] P. Ball, V. M. Braun, and A. Lenz, "Higher-twist distribution amplitudes of the K meson in QCD," *JHEP* **05** (2006) 004, arXiv:hep-ph/0603063.

[164] **RQCD** Collaboration, G. S. Bali *et al.*, "Second moment of the pion distribution amplitude with the momentum smearing technique," *Phys. Lett.* **B774** (2017) 91, arXiv:1705.10236.

[165] J. L. Rosner, S. Stone, and R. S. Van de Water, "Leptonic Decays of Charged Pseudoscalar Mesons – 2015," arXiv:1509.02220.

[166] **QCDSF and UKQCD** Collaborations, V. M. Braun *et al.*, "Moments of pseudoscalar meson distribution amplitudes from the lattice," *Phys. Rev.* **D74** (2006) 074501, arXiv:hep-lat/0606012.

[167] S. Güsken, U. Löw, K.-H. Mütter, R. Sommer, A. Patel, and K. Schilling, "Non-Singlet axial vector couplings of the baryon octet in lattice QCD," *Phys. Lett.* **B227** (1989) 266.

[168] J.-W. Chen, H.-M. Tsai, and K.-C. Weng, "Model-independent results for SU(3) violation in twist-3 light-cone distribution functions," *Phys. Rev.* **D73** (2006) 054010, arXiv:hep-ph/0511036.

[169] P. Ball, G. W. Jones, and R. Zwicky, "$B \to V\gamma$ beyond QCD factorisation," *Phys. Rev.* **D75** (2007) 054004, arXiv:hep-ph/0612081.

[170] P. Ball and V. M. Braun, "Use and misuse of QCD sum rules in heavy-to-light transitions: The Decay $B \to \rho e \nu$ reexamined," *Phys. Rev.* **D55** (1997) 5561, arXiv:hep-ph/9701238.

[171] T. Hurth, "Present status of inclusive rare B decays," *Rev. Mod. Phys.* **75** (2003) 1159, arXiv:hep-ph/0212304.

[172] A. Bruni, X. Janssen, and P. Marage, "Exclusive Vector Meson Production and Deeply Virtual Compton Scattering at HERA," arXiv:0812.0539.

[173] D. Müller, T. Lautenschlager, K. Passek-Kumerički, and A. Schäfer, "Towards a fitting procedure to deeply virtual meson production – the next-to-leading order case," *Nucl. Phys.* **B884** (2014) 438, arXiv:1310.5394.

[174] **RQCD** Collaboration, G. S. Bali *et al.*, "ρ and K^* resonances on the lattice at nearly physical quark masses and $N_f = 2$," *Phys. Rev.* **D93** (2016) 054509, arXiv:1512.08678.

[175] P. Ball and V. M. Braun, "ρ meson light-cone distribution amplitudes of leading twist reexamined," *Phys. Rev.* **D54** (1996) 2182, arXiv:hep-ph/9602323.

[176] A. Bharucha, D. M. Straub, and R. Zwicky, "$B \to V\ell^+\ell^-$ in the Standard Model from light-cone sum rules," *JHEP* **08** (2016) 098, arXiv:1503.05534.

[177] M. Göckeler *et al.*, "Lattice operators for moments of the structure functions and their transformation under the hypercubic group," *Phys. Rev.* **D54** (1996) 5705, arXiv:hep-lat/9602029.

[178] G. Ecker, J. Gasser, A. Pich, and E. De Rafael, "The role of resonances in chiral perturbation theory," *Nucl. Phys.* **B321** (1989) 311.

[179] G. Ecker, J. Gasser, H. Leutwyler, A. Pich, and E. De Rafael, "Chiral lagrangians for massive spin-1 fields," *Phys. Lett.* **B223** (1989) 425.

[180] E. E. Jenkins, A. V. Manohar, and M. B. Wise, "Chiral Perturbation Theory for Vector Mesons," *Phys. Rev. Lett.* **75** (1995) 2272, arXiv:hep-ph/9506356.

[181] J.-W. Chen and I. W. Stewart, "Model Independent Results for SU(3) Violation in Light-Cone Distribution Functions," *Phys. Rev. Lett.* **92** (2004) 202001, arXiv:hep-ph/0311285.

[182] P. Ball and R. Zwicky, "$|V_{td}/V_{ts}|$ from $B \to V\gamma$," *JHEP* **04** (2006) 046, arXiv:hep-ph/0603232.

[183] D. Becirevic, V. Lubicz, F. Mescia, and C. Tarantino, "Coupling of the light vector meson to the vector and to the tensor current," *JHEP* **05** (2003) 007, arXiv:hep-lat/0301020.

[184] **BGR** Collaboration, V. M. Braun *et al.*, "Lattice calculation of vector meson couplings to the vector and tensor currents using chirally improved fermions," *Phys. Rev.* **D68** (2003) 054501, arXiv:hep-lat/0306006.

[185] **RBC and UKQCD** Collaborations, C. Allton *et al.*, "Physical results from $2+1$ flavor domain wall QCD and SU(2) chiral perturbation theory," *Phys. Rev.* **D78** (2008) 114509, arXiv:0804.0473.

[186] M. Diehl, W. Kugler, A. Schäfer, and C. Weiss, "Exclusive channels in semi-inclusive production of pions and kaons," *Phys. Rev.* **D72** (2005) 034034, arXiv:hep-ph/0506171. [Erratum: *Phys. Rev.* **D72** (2005) 059902].